Multi-Terminal Electron Transportin Single-Wall Carbon Nanotubes

Bo Gao

Département de Physique
École Normale Supérieure

Laboratoire Pierre Aigrain

THÈSE de DOCTORAT de l'UNIVERSITÉ PARIS 6

Spécialité: Physique Quantique

présentée par

Bo Gao

pour obtenir le grade de DOCTEUR de l'UNIVERSITÉ PARIS 6

Multi-Terminal Electron Transport in Single-Wall Carbon Nanotubes

---

Soutenue le 13 Juillet 2006
devant le jury composé de:

M.	**Poul Eric Lindelof**	Rapporteur
Mme.	**Inès Safi**	Rapporteur
M.	**Roland Combescot**	Président
M.	**Jean-philippe Bourgoin** ..	Examinateur
M.	**Adrian Bachtold**	CoDirecteur de thèse
M.	**Christian Glattli**	Directeur de thèse

Table of Contents

Abstract

This thesis is devoted to the experimental study of multi-terminal electronic transport properties of single-wall carbon nanotubes. This implies to find new methods to measure reliably the intrinsic resistance of the nanotube, and to probe the one-dimensional nature of the electron behavior in it.

Because the access to the intrinsic resistance of a nanotube is limited by bad contacts in the two-terminal measurement, a new four-terminal measurement technique using multi-wall carbon nanotubes as non-invasive voltage probes has been developed. In the linear regime, at room temperature, four-terminal measurements show that the single-wall nanotube is a classical resistor that obeys Ohm's law. At very low temperature, negative four-terminal resistances due to quantum interference effects are observed, as predicted by Laudauer-Büttiker formula.

At intermediate temperature, the one-dimensional nature of the electron behavior in single-wall carbon nanotube is described by Luttinger Liquid theory. However, previous electron tunneling measurements could not provide enough information to exclude other theoretical explanations, e.g. the dynamical environmental Coulomb Blockade theory. Following the proposition of theoreticians, crossed metallic single-wall nanotube structures have been fabricated. We observe a zero-bias anomaly in one tube which is suppressed by a current flowing through the other nanotube. These results are compared with a Luttinger-liquid model which takes into account electrostatic tube-tube coupling together with crossing-induced backscattering processes. Explicit solution of a simplified model is able to describe qualitatively the observed experimental data with only one adjustable parameter.

Keywords: carbon nanotube, mesoscopic physics, nanotechnology, Luttinger-liquid, Landauer-Büttiker formula

Résumé

Cette thèse a pour objet l'étude expérimentale des propriétés du transport électronique plusieurs contacts dans les nanotubes de carbone monofeuillets. Cela nécessite de trouver des méthodes nouvelles pour mesurer la résistance intrinsèque du nanotube, et aussi pour explorer la nature des comportements électroniques unidimensionnels dans le nanotube monofeuillet.

Comme la mesure électronique deux contacts ne permet pas d'explorer la résistance intrinsèque du nanotube cause de la résistance de contact, nous avons développé une nouvelle méthode de mesure quatre contacts en utilisant des nanotubes multifeuillets comme sondes de tension non-destructives. Les mesures faites sont toujours dans le régime linéaire. A température ambiante, les mesures quatre contacts montrent que le nanotube monofeuillet se comporte comme une résistance classique dont le fonctionnement obéit la loi d'Ohm. A basse température, les mesures quatre contacts montrent des résistances négatives. C'est un effet d'interférence quantique, qui avait été prédit par la formule de Laudauer-Büttiker.

A température intermédiaire, la nature des comportements électroniques unidimensionnels dans le nanotube monofeuillet est décrite par la théorie du Liquide de Luttinger. Cependant, les mesures d'effet tunnel obtenues jusqu' présent ne permettaient pas d'exclure les autres explications théoriques comme la théorie du Blocage de Coulomb dynamique. Suivant la proposition faite par des théoriciens, nous avons fabriqué des structures deux nanotubes monofeuillets croisés. Nous avons observé une anomalie tension nulle dans un des deux tubes, qui peut tre supprimée quand un courant est injecté dans l'autre. Nous avons comparé nos résultats avec les prédictions de la théorie du Liquide de Luttinger, en considérant le couplage électrostatique entre deux tubes et la rétro-diffusion d'électron provoquée par la déformation des tubes au point de croisement. La solution explicite du modèle simplifié nous permet de décrire qualitativement les résultats expérimentaux avec un seul paramètre ajustable.

Mots-clés : nanotube de carbone, physique mésoscopique, nanotechnologies, liquide de Luttinger, formule de Laudauer-Büttiker

Acknowledgement

First of all, I want to thank Dr.Inès Safi and Prof.Poul Eric Lindelof for accepting to be the referees of my thesis, as well as Prof. Roland Combescot and Prof.Jean-Philippe Bourgoin for accepting to join the jury of this thesis. Many thanks for their time devoted to the careful reading of the manuscript. I benefited a lot from their comments and suggestions on my thesis.

The work of this thesis was realized at the Physics Department of the École Normale Supérieure in Paris. I want to thank the successive directors of the department, Michel Voos and Jean-Michel Raimond, for their reception. I need also to thank particularly Claude Delalande, director of the Laboratoire Pierre Aigrain, for his welcome, as well as for excellent working conditions and a friendly atmosphere that I benefited much within the laboratory.

This thesis was supervised by Adrian Bachtold and Christian Glattli. I would first like to thank Adrian. It was him who guided me into the world of the scientific research, and shared with me unselfishly his knowledge on carbon nanotubes. I benefited a lot from his originality, his enthusiasm, and his experimental expertise. It was really a great opportunity for me to work with him. I also owe a large debt of gratitude to Christian. His insight into physics has been a constant source of inspiration and his clear explanation has greatly enhanced my understanding to the mesoscopic physics.

I need also to show my great gratitude to Bernard Plaçais, who always gives his hands to me when I was in difficult situations (visa, resident permit, etc...). Many thanks for helping me solve different experimental technical problems, for patient discussions and for the preparation of the thesis manuscript and the defense presentation. I would like also to thank Jean-Marc Berroir and Takis Kontos for their sagacious advices on many different aspects in my studies, and for their time and energy devoted to the preparation of my thesis.

I must not forget the other post-doc and students in our group. The three years I passed with you is really an amiable time to remember. I thank you all with my heart, Kyoko Nakada, Bertrand Bourlon, Julien Gabelli, Gwendal Fève, Julien Chaste, Adrien Mahé, Lorenz Herrmann, Thomas Delattre, Chéryl Feuillet-Palma...

For my work of thesis, high quality single-wall and multi-wall carbon nanotubes

have been necessary. I would like to thank Richard Smalley (Rice University), Yung-Fu Chen and Michael Fuhrer (Maryland University) for providing me single-wall carbon nanotubes. I also want to thank Csilla Miko and Laszlo Forró (EPFL) for the synthesis of multi-wall carbon nanotubes. I would also like to thank Andrei Komnik and Reinhold Egger for theoretical supports.

During my work of thesis, I benefited much from the technical supports brought by many excellent engineers in the laboratory. I would like to thank Pascal Morfin for his constant supports to my work. I benefited much from the communications with him. I would like to thank Francois-René Ladan and Michael Rosticher for maintaining the well-function of the clean-room, to thank Laurent Réa, David Darson, Anne Denis and Philippe Pace for their help in numerous aspects (pump, evaporator, etc...). I also want to thank Olivier Andrieu and Willy Daney de Marcillac for their efforts to provide me a constant supply of Liquid Helium.

I need also show my great gratitude to Anne Matignon, Isabelle Michel and Fabienne Rénia for their kind help concerning many administrative questions.

I would like to thank Sébastian Berger, Christophe Voisin, Guillaume Cassabois, Cristiano Ciuti, Nicolas Regnault and Thierry Joliceur for helpful discussions. I also want to thank Manuel Aranzana, Arnaud Labourt-Ibarre, Arnaud Verger, Thomas Grange, Ivan Favero, Zhenyu Zhao, Gumao-Bezerra Marilza for sharing with me those convivial days.

I would like to thank the French ministry of research for the fellowship(AMX) which assures me the financial support of this thesis.

I would like also thank Yijun Yao, Yun Luo, Xiaolong Li,Guodong Zhou, Huayi Chen, Ying Jiao, Zheng Gong, Xiang li, Ye Zhu, Tieyong Zeng, Feng Zhou, Cengbo Zheng for your kind help. I will always cherish the six years' life with you all in Paris.

There are still many more people in China and in France, to whom I need to show my gratitude. Though I cannot list all your names here, I must say that without your help I can not come to France to continue my study. I will never forget the hands that you gave me before.

I would like to thank my family. I owe them a lot.

Introduction

One-dimensional electron systems have been a very exciting research field since a few decades. As prescribed by quantum mechanics, the electron behavior should be described by its wave function. In case that the size of the system is comparable to the electron coherence length, quantum interference effects between electron waves should become important. In a series of work, R. Landauer and M. Büttiker have established how these interference effects affect electron transport in low-dimensional systems (a detailed description can be found in Ref.[1]).

Beyond that, as one takes into consideration the long range Coulomb interaction between electrons, which prevails in a one-dimensional system, so that the electron behavior will be completely different from that of normal metals. Theoretical investigations of this problem began about half a century ago by S. Tomonaga and J. Luttinger [2, 3]. According to their findings, the low-energy excitations in a 1-d interacting electron system are collective excitations, while the excitations in normal metal are the well known Laudau-quasi particles. The Coulomb interaction between electrons in the 1-d case will involve all electrons together, and this system is refereed to as Tomonaga-Luttinger Liquid (often simplified as Luttinger Liquid).

In order to test these theoretical predictions, an experimental model system is needed. Recent discovery of single-wall carbon nanotubes (SWNTs) provide us a nearly perfect model system to study the one-dimensional electrons. A SWNT can be regardes as a single layer of graphite, also called graphene sheet, rolled into a seamless hollow cylinder. A high quality metallic SWNT has very little disorder

along it, giving a long elastic electron mean-free path up to several microns. It is also easy to manipulate and investigate with existing experimental techniques like scanning prober microscope (SPM) and lithography.

Indeed, carbon structures similar to carbon nanotubes were observed a long time ago (see more detailed descriptions in Ref.[4, 5]). However one did not recognize the importance of these structures until the beginning of 1990s, when since they were shadowed before by the great success of the silicon technology. In 1991, S. Iijima reported his finding of multi-walled carbon nanotubes [6], which triggered a new era of research on carbon nanotubes. Two years later, SWNTs were discovered independently by Iijima's group at NEC and by Bethune's one at IBM [7, 8]. Then in 1995-1996, Smalley's group in Rice University managed to produce high quality SWNTs in large quantity using laser-vaporation of graphite [9, 10]. From then on, a lot of experimental electron transport measurements have been carried out on individual SWNTs and on bundles of SWNTs, which appear to confirm the previous theoretical predictions [11, 12, 13, 14, 15, 16]. Our knowledge of the one-dimensional electron system has therefore been greatly enriched.

The present work is in the same spirit. It uses SWNTs as a model system to understand the one-dimensional electron physics. And more specifically, it focuses on the experimental study of multi-terminal electronic transport in SWNTs. The manuscript is structured as follows:

In the first chapter, we review the general properties of single-wall carbon nanotubes. We start by a simple introduction to the atomic and electrical band structure of the graphene. We then give a general description to the atomic structure of a SWNT. The electronic band structure of a SWNT can be derived from that of the graphene sheet, using the quantization condition of electron wave vector along the perimeter of the nanotube.

In the seconde chapter, we present a simple description of sample fabrication and

characterization techniques. We show how a mesoscopic object like a SWNT can be electrically contacted and investigated.

In the third chapter, we discuss the four-terminal resistance measurements on SWNTs. Indeed, two-terminal measurements are strongly affected by bad contacts with high resistances, and a new method is needed to measure reliably the intrinsic SWNT resistance. We have developed a four-terminal measurement technique using multi-wall carbon nanotubes as non-invasive voltage probes. In the linear regime, at room temperature, four-terminal measurements show that the SWNT is a classical resistor that obeys Ohm's law. At very low temperature, negative four-terminal resistances are observed due to quantum interference effects , as predicted by Laudauer-Büttiker formula [18].

In the last chapter, we investigate the one-dimensional nature of the electron behavior in the SWNT, which is described by Luttinger Liquid theory at intermediate temperature. Previous electron tunneling measurements could not provide enough information to exclude other theoretical explanations, e.g. the dynamical environmental Coulomb Blockade theory. Following the proposition of theoreticians, crossed metallic single-wall nanotube structures have been fabricated. We observe a zero-bias anomaly in one tube which is suppressed by a current flowing through the other nanotube. These results are compared with a Luttinger-liquid model which takes into account electrostatic tube-tube coupling together with crossing-induced backscattering processes. Explicit solution of a simplified model is able to describe qualitatively the observed experimental data with only one adjustable parameter [17].

Chapter 1

Atomic and Electronic structure of Single-Wall Carbon Nanotubes

A single-wall carbon nanotube (SWNT) can be described as a monolayer of graphite, also called as a graphene layer, rolled up into a cylindrical shape. It is a one-dimensional structure with a variety of chirality, depending on the manner the graphene layer is rolled up. The electronic structure of a SWNT can therefore be derived from that of the graphene layer, which in turn can be obtain by a simple tight-binding calculation.

This chapiter is organized in the following way. In the Sec.1.1, we briefly describe the atomic structure of a graphene layer. We also present a simple tight-binding calculation for the π-electrons of carbon atoms in the graphene layer, from which the electronic structure of π-bands can be found. In the Sec. 1.2, we discuss the atomic structure of a SWNT. Several characteristic parameters will be defined. At the end of the section, the band structure of a SWNT will be obtained from that of a graphene layer.

1.1 The Two-dimensional Graphene Layer

1.1.1 Atomic Structure

The two-dimensional graphene layer is a very unique carbon material whose electronic properties have been recently investigated experimentally [19, 20]. However for the sake of describing the electronic properties of SWNTs, it is sufficient to consider here a simple model for the electronic structure of the graphene, which is described below.

In the Fig. 1.1 below we show the unit cell and the first Brillouin zone of a graphene layer. The unit cell is marked by the rhombus in the figure 1.1(a). Both $\mathbf{a}_1$ and $\mathbf{a}_2$ are unit vectors in real space.

$$\mathbf{a}_1 = (\frac{\sqrt{3}}{2}a, \frac{a}{2}),\ \mathbf{a}_2 = (\frac{\sqrt{3}}{2}a, -\frac{a}{2}) \tag{1.1.1}$$

where $a = |\mathbf{a}_1| = |\mathbf{a}_2| = 0.246nm$ is the lattice constant of the graphene layer.

Correspondingly, the hexagon in figure 1.1(b) is the first Brillouin zone of the reciprocal space. $\mathbf{b}_1$ and $\mathbf{b}_2$ are the unit vectors of the reciprocal lattice,

$$\mathbf{b}_1 = (\frac{2\pi}{\sqrt{3}a}, \frac{2\pi}{a}),\ \mathbf{b}_2 = (\frac{2\pi}{\sqrt{3}a}, -\frac{2\pi}{a}) \tag{1.1.2}$$

Three high symmetry points, Γ, K and M, can be defined as the center, the corner, and the center of the edge of the first Brillouin zone.

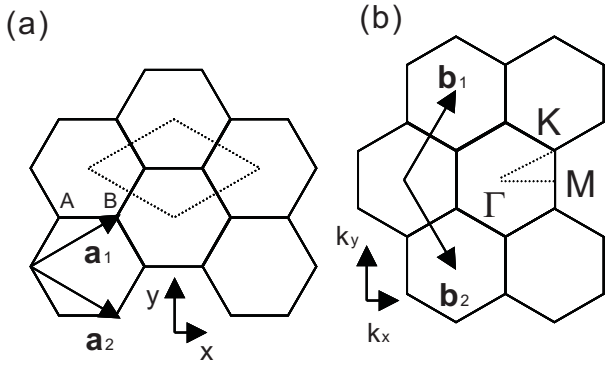

Figure 1.1: (a) The unit cell (dotted rhombus) and (b) Brillouin zone of two-dimensional graphene sheet are shown. A and B signify two inequivalent carbon atoms. $\mathbf{a}_i$ and $\mathbf{b}_i$ (i=1,2) are the unit vectors in real and reciprocal space, respectively. Γ, K and M are three high symmetry points in reciprocal lattice, Γ is the center point, K is at the corner and M is at the center of the edge.

1.1.2 Electronic Structure of π-bands

In the graphene layer, each carbon atom has three σ bands that hybridize in a sp^2 configuration, while the left $2p_x$ orbital, which is perpendicular to the graphene plane, make π covalent bands. As the π electrons are the valence electrons which dominate the electronic transport properties, we focus here only on π-bands. We use a simple tight-bind method to calculate the π-bands of the graphene layer.

Because there are two inequivalent carbon atomes A and B in the unit cell, one can construct two Bloch functions from atomic orbitals for the two inequivalent atoms.

$$\Phi_\alpha(r) = \frac{1}{\sqrt{M}} \sum_j e^{i\mathbf{k}\cdot\mathbf{R}_{j,\alpha}} \phi_\alpha(\mathbf{r} - \mathbf{R}_{j,\alpha}) \tag{1.1.3}$$

where the summation is taken over all the cells, M is the total number of cells. ϕ_α denotes the atomic wave-function of atom A or B in the jth cell, $\mathbf{R}_{j,\alpha}$ is the atom coordinate.

The eigenfunction of π-electrons in the graphene layer can therefore be written as

$$\Psi(\mathbf{r}) = C_1\Phi_A + C_2\Phi_B \tag{1.1.4}$$

where $C_{1,2}$ are two coefficients to be determined.

The eigenvalue of the energy can therefore be obtained by solving the Schrödinger equation:

$$\hat{H}|\Psi >= E|\Psi > \tag{1.1.5}$$

Taking only the contribution from the nearest neighbors, and assuming the overlap of wave-functions between carbon atoms to be zero. The above equation can be rewritten in the following form:

$$\begin{pmatrix} -E & tf(\mathbf{k}) \\ tf(\mathbf{k})^* & -E \end{pmatrix} \begin{pmatrix} C_1 \\ C_2 \end{pmatrix} = \begin{pmatrix} 0 \\ 0 \end{pmatrix} \tag{1.1.6}$$

where t is the transfer integral between the nearest neighbors that is around $-3eV$ [21], and $f(\mathbf{k})$ is defined as

$$f(\mathbf{k}) = e^{ik_x \frac{a}{\sqrt{3}}} + 2e^{-ik_x \frac{a}{2\sqrt{3}}} \cos\frac{k_y a}{2} \tag{1.1.7}$$

where $k_{x,y}$ is the electron wave vector in the x/y direction.

On resolving this equation, one finds that the dispersion relations of π-bands in a graphene layer take the following expression:

$$E_{\pm}(k_x, k_y) = \pm t\sqrt{1 + 4\cos\frac{\sqrt{3}k_x a}{2}\cos\frac{k_y a}{2} + 4\cos^2\frac{k_y a}{2}} \tag{1.1.8}$$

$E_+(\mathbf{k})$ and $E_-(\mathbf{k})$ are called bonding π and antibonding π^* energy bands. One can see that at the corner point K in the first Brillouin zone, both bands take the same energy $E = 0$, therefore there is no band gap between two bands (See Fig 1.2). As there are two inequivalent atoms in the unit cell, the antibonding band π^* will be completely filled, the Fermi level will be at E=0. We will see below that this has a strong influence on the electronic structure of a single-wall carbon nanotube.

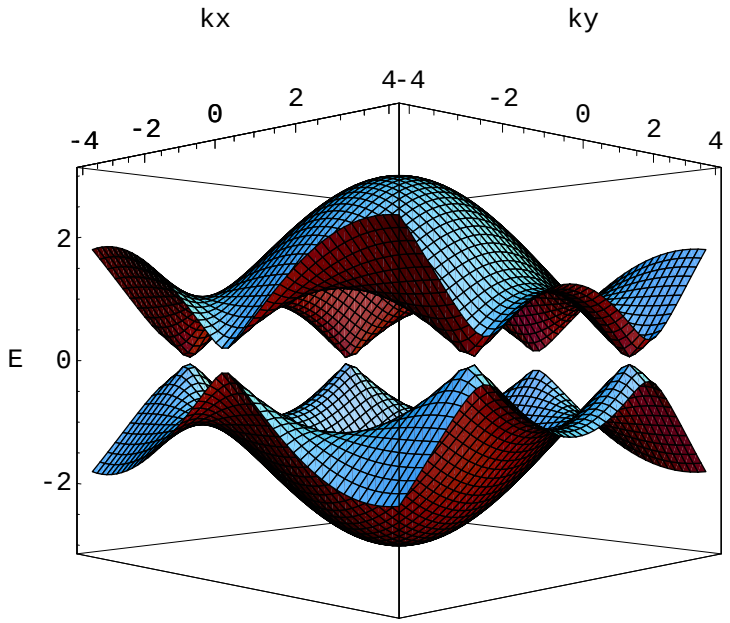

Figure 1.2: The energy dispersion relations for a two-dimensional graphene sheet are shown. The bonding and antibonding bands cross each other at K points. Therefore it is a zero gap semiconductor. The plot is in arbitrary unit.

1.2 Single-Wall Carbon Nanotube

1.2.1 Atomic Structure

A single-wall carbon nanotube can be described by rolling up a graphene sheet. The most important parameter to define the atomic structure of a SWNT is the chiral vector $\mathbf{C}_h$ (the vector in **OA** the Fig 1.3), which corresponds to the perimeter of the

nanotube. The chiral vector can be expressed by the two unit vectors $\mathbf{a}_1$ and $\mathbf{a}_2$ of the graphene lattice in the real space:

$$\mathbf{C}_h = n\mathbf{a}_1 + m\mathbf{a}_2 \equiv (n, m) \tag{1.2.1}$$

where n and m are integers, satisfying $0 \leq m \leq n$ (because of the hexagonal symmetry of the graphene lattice, we need to only consider the cases $0 \leq m \leq n$). For the case n=m, this is the so-called armchair nanotube; for m=0 it is called zigzag nanotube; all other (n,m) chiral vectors correspond to a chiral nanotube.

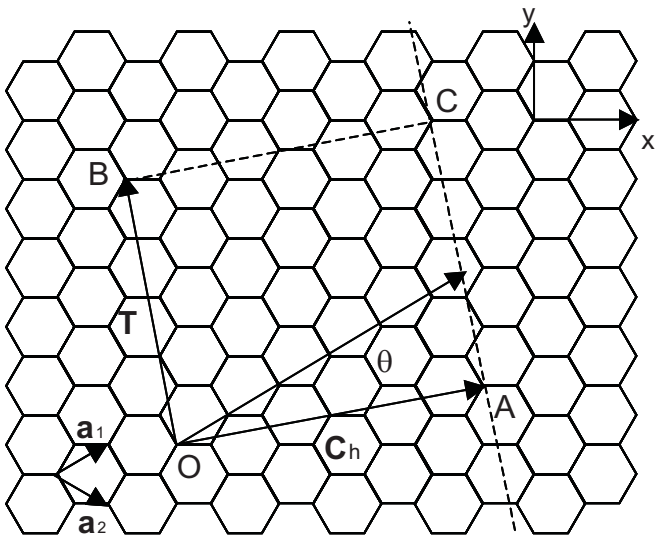

Figure 1.3: The unrolled honeycomb lattice of a nanotube. **OA** is the chiral vector $\mathbf{C}_h$, **OB** signifies the translation vector **T**, the rectangle OACB defines the unit cell of a nanotube, θ is the chiral angle, and $\mathbf{a}_i, i = (1, 2)$ is the unit vector of the graphene lattice in real space.

From the chiral vector, one can easily find that the diameter d_t of a nanotube is

$$d_t = |\mathbf{C}_h| / \pi = a\sqrt{n^2 + m^2 + nm}/\pi \tag{1.2.2}$$

where a is the lattice constant of the graphene layer defined in the previous section.

One can also define the chiral angle θ between the chiral vector $\mathbf{C}_h$ and $\mathbf{a}_1$:

$$\cos\theta = \frac{\mathbf{C}_h \cdot \mathbf{a}_1}{|\mathbf{C}_h|\,|\mathbf{a}_1|} = \frac{2n + m}{2\sqrt{n^2 + m^2 + nm}} \tag{1.2.3}$$

where θ is limited by $0 \leq |\theta| \leq 30^\circ$ because of the hexagonal symmetry of the graphene lattice.

Apart from the chiral vector $\mathbf{C}_h$, one can define the translation vector $\mathbf{T}$, which is the unit vector of the nanotube. The translation vector is parallel to the nanotube axis and is normal to the chiral vector. As seen in the Fig 1.3, it corresponds to the first lattice point B of the graphene layer through which the vector passes. One can find

$$\mathbf{T} = t_1\mathbf{a}_1 + t_2\mathbf{a}_2 \equiv (t_1, t_2) \tag{1.2.4}$$

where t_1 and t_2 are integers, and they do not have a common divisor except the unity. The precise expression for $t_{1,2}$ is

$$t_1 = \frac{2m+n}{d_R},\ t_2 = -\frac{2n+m}{d_R} \tag{1.2.5}$$

where d_R is the greatest common divisor of $(2m+n)$ and $(2n+m)$.

Since both the chiral vector and the translation vector have been defined, one can therefore find the unit cell of the one-dimensional nanotube, which is the rectangle OACB in the Fig 1.3 generated by $\mathbf{C}_h$ and $\mathbf{T}$. The number of carbon atoms in a unit cell is given by 2N, where N is

$$N = \frac{|\mathbf{C}_h \times \mathbf{T}|}{|\mathbf{a}_1 \times \mathbf{a}_2|} = \frac{2(m^2+n^2+nm)}{d_R} = \frac{2\pi^2 d_t^2}{a^2 d_R} \tag{1.2.6}$$

Above we presented briefly the atomic structure the a SWNT in real space, we can now turn to the reciprocal space. Two reciprocal lattice vectors $\mathbf{K}_1$ and $\mathbf{K}_2$ can be defined. $\mathbf{K}_1$ is in the circumferential direction and $\mathbf{K}_2$ is along the tube axis. Using the definition relations below

$$\begin{aligned} \mathbf{C}_h \cdot \mathbf{K}_1 = 2\pi,\ \mathbf{T} \cdot \mathbf{K}_1 = 0 \\ \mathbf{C}_h \cdot \mathbf{K}_2 = 0,\ \mathbf{T} \cdot \mathbf{K}_2 = 2\pi \end{aligned} \tag{1.2.7}$$

one can find that

$$\mathbf{K}_1 = \frac{1}{N}(-t_2\mathbf{b}_1 + t_1\mathbf{b}_2),\ \mathbf{K}_2 = \frac{1}{N}(m\mathbf{b}_1 - n\mathbf{b}_2) \tag{1.2.8}$$

As the nanotube is one-dimensional material, only $\mathbf{K}_2$ is a real reciprocal unit vector for a SWNT. The length of the first Brillouin zone is given by $|\mathbf{K}_2| = 2\pi/|\mathbf{T}|$.

For the vector $\mathbf{K}_1$, it is not a reciprocal unit vector of the nanotube, however it gives the discrete $\mathbf{k}$ value in the direction of $\mathbf{C}_h$, with $\mathbf{k} = k\frac{\mathbf{K}_2}{|\mathbf{K}_2|} + \mu\mathbf{K}_1, -\frac{\pi}{|\mathbf{T}|} \leq k \leq \frac{\pi}{|\mathbf{T}|}, \mu = 0, 1..., N-1$. This is due to the periodic boundary condition in the

circumferential direction of the nanotube, wavevectors in this direction become quantized. Since $N\mathbf{K}_1 = (-t_2\mathbf{b}_1 + t_1\mathbf{b}_2)$ is a reciprocal unit vector of the graphene sheet, two wave vectors which differ by $N\mathbf{K}_1$ are equivalent. Therefore, there are N different wave-vectors $\mu\mathbf{K}_1$ that give rise to N discrete k vectors, and N one-dimensional sub-bands of a nanotube appear.

1.2.2 Electronic Structure

The electronic structure of a SWNT can be deduced from that of a graphene layer. As we mentioned above, because of the periodic boundary condition in the circumferential direction of the nanotube, the electron wave-vector in this direction becomes quantized. On the other hand, the wave-vector along the direction of tube axis remains continuous provided that the length of the nanotube is infinite. Therefore the energy bands of a SWNT can be obtained from cross sections of those of a graphene layer.

One may take the example of a armchair nanotube (n,n). Using the definitions above, one may find the chiral vector $\mathbf{C}_h$ is in the direction $\mathbf{e}_x$; and the translation vector $\mathbf{T}$, which is normal to the chiral vector, is in the direction $\mathbf{e}_y$:

$$\begin{aligned} \mathbf{C}_h &= n(\mathbf{a}_1 + \mathbf{a}_2) = n\sqrt{3}a\mathbf{e}_x \\ \mathbf{T} &= \mathbf{a}_1 - \mathbf{a}_2 = a\mathbf{e}_y \end{aligned} \tag{1.2.9}$$

Because of the periodic boundary condition in this direction, the electron wave-vector k_x becomes quantized,

$$n\sqrt{3}k_{x,q} = 2\pi q, (q = 1, 2...2n) \tag{1.2.10}$$

On the other hand, the electron wave-vector k_y along the tube axis, in this case in the direction $\mathbf{e}_y$, remains continuous. On substituting Eq.1.2.10 into Eq.1.1.8, one finds the following dispersion relation:

$$E_{\pm,q}(k) = \pm t\sqrt{1 + 4\cos\frac{q\pi}{n}\cos\frac{ka}{2} + 4\cos^2\frac{ka}{2}} \tag{1.2.11}$$

where $\pm$ denotes the bonding π and antibonding π^* bands, q is the integer between 1 and 2n that denotes the sub-band index, and $-\pi \leq ka \leq \pi$ signifies the first Brillouin zone.

For an armchair SWNT (n,n), one can easily find, for both bonding and antibonding bands q=n, $E(k = \pm 2\pi/3a) = 0$, the bonding and antibonding sub-bands

cross each other. There are in total 2n antibonding sub-bands; as the number of π electrons is equal to that of the carbon atoms, which is 4n as derived from Eq 1.2.6, therefore all the antibonding sub-bands are fully occupied. The fermi level is at the crossing point. This makes the armchair SWNT a metallic nanotube. And there are four transport channels at the Fermi lever, factor 2 comes from the spin degeneration.

Fig 1.4 shows the dispersion relations calculated from the above equation for an armchair SWNT (5,5).

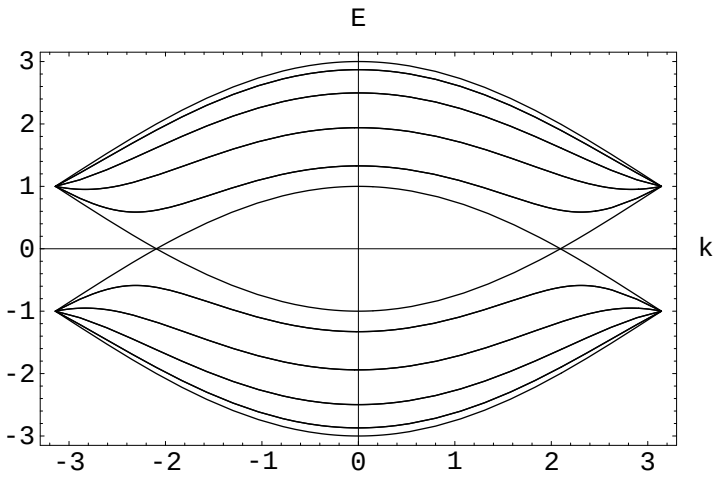

Figure 1.4: One dimensional energy dispersion relations for an armchair SWNT (5,5). Those bands with positive energy are antibonding π^* sub-bands and those with negative energy are bonding π sub-bands. The bonding and antibonding sub-bands with band label q=5 cross each other at $k = \pm 2\pi/3a$. The Fermi level is at the crossing point. The plot is in arbitrary units.

The electronic band structure of zigzag and chiral nanotubes can also be derived from that of a graphene sheet. They can be metallic or semiconducting, depending on the index of nanotube (n,m). The general condition for metallic nanotubes is that (n-m) is a multiple of 3 [22].

We at last need to mention the Peierls Instability. In general metallic 1-D materials are unstable under a Peierls distortion, however it has been found that for metallic SWNT, the energy gap due to the Peierls distortion decreases rapidly to zero when increasing the diameter of the tube [23, 24]. Therefore both metallic and semiconducting SWNTs exist.

Chapter 2

Techniques of Sample Fabrication and Characterization

We have briefed in the previous chapiter the fundamental properties of carbon nanotubes. We are specially interested in electron transport properties of single-wall carbon nanotubes (SWNT). To probe these properties, metal electrodes need to be made to carbon nanotubes so that I-V curves can be registered. In this chapiter, we will present various techniques related to sample fabrications (Sec.2.1) and sample characterizations (Sec.2.2).

2.1 Sample Fabrication

A single-wall carbon nanotube is a several-μms long cylinder, whose diameter is usually less than 2nm. Making electrical contacts to such a small object needs tens of hours work. To ensure the quality of the sample, most of the sample-fabrication work need to be carried out inside a clean room. The experimental equipments, such as beakers, flasks and tweezers, should be cleaned before the utilization and kept in a clean space. The choice on solutions used to clean equipments can be made among rectapure acetone, rectapure 2-isopropanol and deionized water, depending on the object to be cleaned. An object may be cleaned several times with different solution before the use, and the cleaning is mostly made in a ultrasonic tank (100W, 42Khz).

2.1.1 Preparation of the Silicon Wafer

To make a electrical contact to a SWNT, we need first to find an isolator to support the nanotube. We therefore use a doped silicon wafer with a 500nm thick silicon-oxide

layer on the top. We usually cut a large silicon wafer into small pieces with a typical size of 8mm×8mm. We then clean the wafer by dipping it successively in acetone, deionized water, nitride acid, deionized water again and at last 2-isopropanol. The cleaning is done in the ultrasonic tank . Each step take one minute except the first one in acetone, which takes five minuets instead. Cautions need to be taken when transferring the wafer from one solution to another. One should behaves quickly in order to not dry the wafer, if not dirties will be left on the wafer surface. The final drying process is done with a gun of azote gas (that's why it is important to verify the pressure in the bottle of azote before cleaning the wafer). The typical roughness of the wafer surface is around one 1nm.

2.1.2 Alignment Marks

Once the silicon wafer is cleaned, nanotubes can be deposited on it. However, as nanotubes will be put onto the wafer in a random way, one would need something to help to determine the position of a nanotube. Therefore alignment marks need to be evaporated onto the wafer surface before the deposition of tubes (Indeed, alignment marks can also be fabricated after the deposition of tubes. This is another technique for contacting nanotubes grown by Chemical-Vapor -deposition method. We will not go into details here). These metallic marks are fabricated using lithography technique, which will be discussed in the subsection below. The highness of an alignment mark is often tens of nms. They can be further classified into two groups: the size of large one is several hundreds μms, that of small one is about a few μs. The combination of large and small alignment marks allows us to determine the position of a nanotube with a precision down to 50nms.

2.1.3 Deposition of Nanotubes

Now we have a silicon wafer with pre-fabricated alignment marks, we can start to deposit the carbon nanotubes onto the wafer. Carbon nanotubes fabricated by laser-ablation methods look like black powder, tubes are usually intertwisted into bundles. In order to get isolated nanotubes, the traditional method involves the use of ultrasonic bath. which can help dispersing the nanotubes from bundles. A few pieces of carbon nanotubes are firstly put into a small bottle, inside which there is 3-5 cm^3

of dichloroethane solution. The bottle is then suspended in the ultrasonic tank. We usually leave the bottle in the tank for about 45 minuets. One should know that long time, high ultrasonic intensity will induce disorder inside the nanotube.

Once the ultrasonic bath is done, one needs to begin immediately the deposition of nanotubes onto the silicon wafer because tubes in the dichloroethane solution tends to intertwist with each other as time passes. The deposition is made by a technique called spin-coating. One or two drops of the nanotube solution are put on the wafer so that at least 2/3 of wafer surface is covered. The wafer is then rotated with relatively low speed (acceleration: 1000 $circle/min^2$, velocity: 1000 $circle/min$). About 5 seconds later, when the color of the wafer change (that means the solution on the surface is almost dried), we increase the velocity to 2000 $circle/min$. Keeping this velocity for 25 seconds, the deposition is completed. The above process need to be repeated several times in order to get a appropriate tube density on the wafer, which can be checked under the Atomic Force Microscope (**AFM**).

2.1.4 Locating the Carbon Nanotube

We usually locate the carbon nanotube under an Atomic Force Microscope, which can give the image of the wafer surface. The position of a nanotube is determined with respect to the four alignment marks around it (Fig 2.1). The diameter of a nanotube can also be roughly found from its highness in the **AFM** image with a precision down to 1nm. We can therefore select the best nanotube to contact, on considering tube itself (usually the tube need to be long, strait, with homogenous diameter along the total length of the tube), its nearby environment (too much dirties/tubes around may make the contacts bad or cause short-current.)

2.1.5 Making Electrical Contacts to Nanotubes

Once we decide the nanotube to be contacted, we can now put metal electrodes onto the selected area of the nanotube. This can be down using electronic lithography, which protected the undesired area from the metal evaporation.

Lithography is the traditional technique for printing on a smooth surface. The essence of electronic lithography is the same as its ancestor. Fig 2.2 illustrate the different step of an electronic lithography procedure: firstly, a layer of electro-sensitive

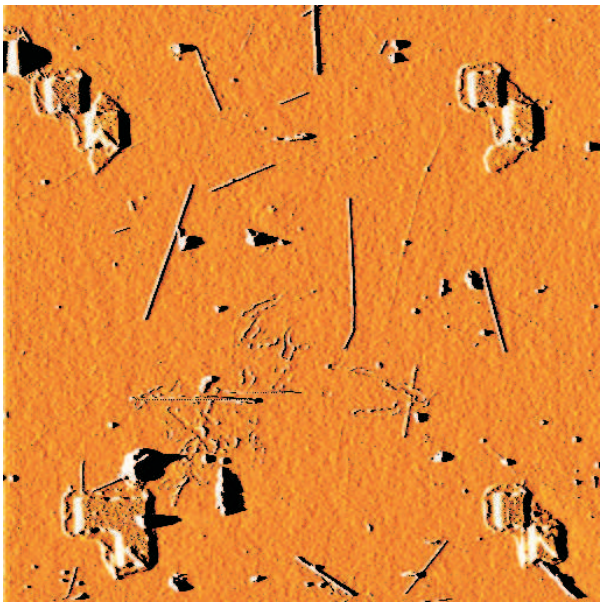

Figure 2.1: The AFM image shows catbon nanotubes on the surface of a silicon wafer. Four alignment marks lie at the corners of the image, which serve as the references to locate a nanotube.

resist (polymer) is deposited on the top surface of the silicon wafer. The wafer is then selectively exposed to high-energy electron beam (25kev) in a controlled manner. The high energy electron breaks inter-chains of the polymer molecular, therefore degrading the resist in those exposed area. The degraded resist can be lifted through the developing process, while the left resist on the surface still covers the undesired area. The metal evaporation can now be done and electrodes are attached to the nanotube. After washing off the rest resistor in hot acetone solution (Lift-Off), the sample fabrication is completed.

Deposition of the Resist

To facilitate the Lift-Off process, we deposit successively two different electro-sensitive resist, first **MAA** (Methacrylic Acid solution) then PMMA (Polymethyl Methacrylate solution), onto the silicon wafer. The deposition is also done with the spin-coating method (acceleration: 4000 $circle/min^2$, velocity: 4000 $circle/min$, time: 30 seconds). After the deposition of the **MAA**, the wafer need to be heated to 160 Celsius degrees for at least 5 minuets evaporate the solvent. The wafered need to be cooled for one minuet before the deposition of the PMMA, in order to not damage the latex airproof gasket. One can then deposit the **PMMA**, the wafer is finally reheated to

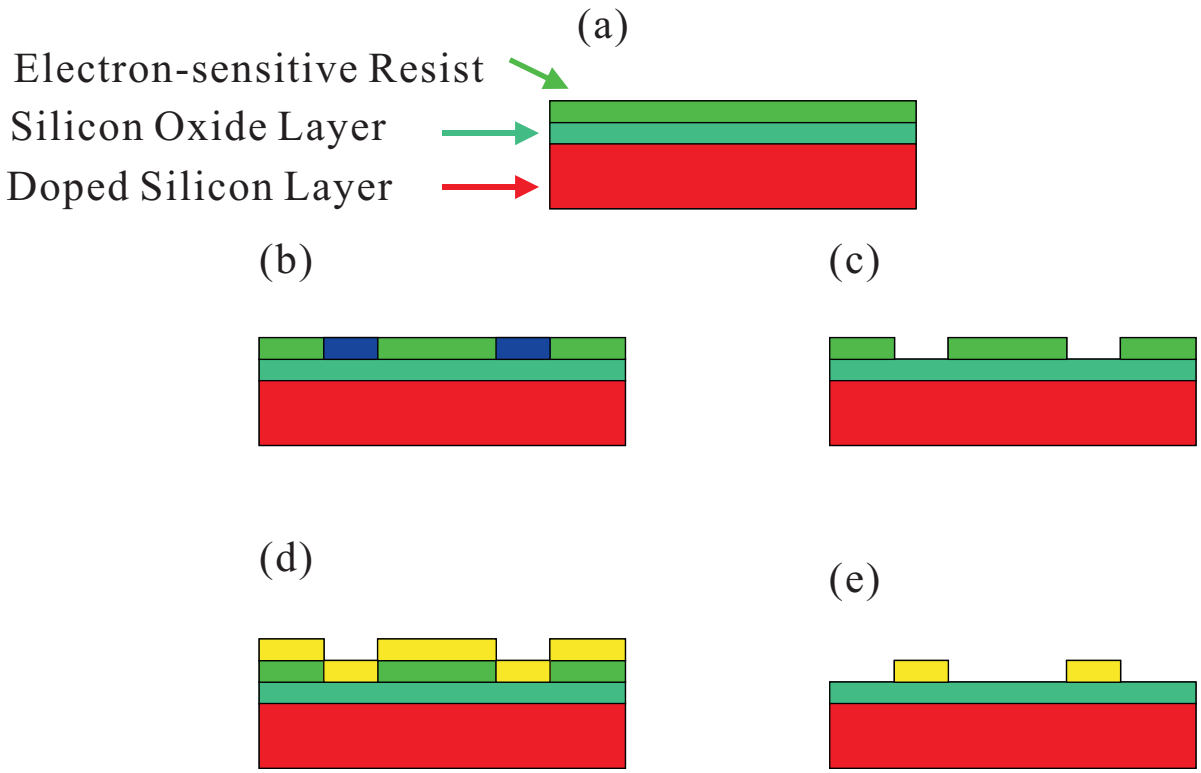

Figure 2.2: (a) The electro-sensitive resist deposited on the top surface of the silicon wafer. (b)High energy electrons attack the selected area on the resist layer, cutting the interconnections between polymer chains. (c) After the development, the degraded resist is lifted. (d) Metal evaporation covers a metallic layer on the top of the wafer. (e) Lift-off process takes away the undesired metal parts.

160 Celsius degrees for more than 15 minuets to evaporate the solvent.

Electronic Lithography

Electronic lithography is carried out inside a Scanning Electron Microscope (**SEM**, model: JEOL 2200). After the wafer is loaded into the chamber, one need first optimize different parameters of the **SEM**, in order to get it well focused on the wafer surface.

Then the alignment procedure to locate nanotubes must be down. This involves several steps:

1. To locate the position of the wafer by one pre-selected corner, it functions as the reference point for large structure. The x-y coordinates of the corner are read from rulers on the **SEM** with a precision down to 10 μms.

2. Knowing the relative positions of alignment marks with respect to the reference point, zoom the view-field into the area with the alignment marks.

3. Another alignment process is done to locate several special alignment marks serving as reference points for small structures. The position of a nanotube can therefore be determined with a precision down to 50 nms.

One can then expose the selected area of the wafer surface to electron beam. The geometry of the electrode is thus defined. Parameters like beam intensity, exposing time can be controlled by the software.

Development

We use a mixed solution of Methylisobutylcetone (**MIBK**) and 2-Isopropanol (**IPA**) to develop the exposed resist. The solution is made with one volume of **MIBK** and three volume of **IPA**. The wafer need to be washed in the solution for 70 seconds, then transferred to the solution of **IPA** for more than 30 seconds to stop the developing. The temperature of the mixed solution can dramatically change the effect of the development. To our experience, 18-20 Celsius degrees is the appropriate temperature.

Evaporation

The deposition of metal electrodes is done with the metal evaporation. The metal electrode is mostly fabricated with Cr/Au in our experiments. One layer of Cr (3-5nm

thick) is first evaporated onto the wafer for that Cr can well adhere to silicon oxide. Then the second layer of Au (40-100nm thick) can be evaporated. The evaporation is done in high-vacuum ($10^{-6}mbar$) by heating the material through Joule Effect. As large quantity of gas molecules are absorbed on the surface of Cr, a degassing process is necessary before the evaporation, which can be down by slightly heating the Cr in the vacuum.

Lift-off

After the evaporation, the wafer is completed covered by a metallic layer. To lift the undesired metal layer, one need to leave the wafer in hot acetone (54 Celsius degrees) for 10 minuets. A syringe is used to eject acetone flux onto the wafer surface to help to remove the metal layer. The wafer is then cleaned in 2-isopropanol.

2.2 Sample Characterization

After the metal electrodes have been successfully attached to a nanotube, the electrical transport measurement can be performed under a probe-station or inside a Helium 4 cryostat.

Measurement under a Probe-Station

Under the probe-station, the nanotube device is contacted by metal tips, which can be manipulated in x-, y- and z- three directions under a binocular microscope. One need to take cautions when manipulating the metal tips. As the oxidized silicon isolation layer of the sample is only 500nm thick, the metal tip must make a stable however slight contact with the electrode in order to not penetrate the isolation layer, otherwise a short-circuit with the underground doped silicon layer will totally destroy the sample. Another caution that needs to be taken by a manipulator is the hazard of electro-static charge. The electro-static potential carried by a manipulator can be up to several thousands volts. Such a high voltage can easily induce a large pulse current through the nanotube and burn it down if a direct contact between the manipulator and the sample is constructed. Therefore the manipulator need to always keep himself discharged when doing the measurements under the probe-station. Indeed, once the metal electrodes have been attached to the nanotube, one need to take the caution

against the hazard of electro-static charge when handling the sample.

Wire-bonding

We usually perform only preliminary measurements under the probe station to select some best devices for further investigations. Most of the measurements are afterward carried out inside a Helium 4 cryostat.

In order to load the sample into the cyostat, it needs to be sticked to a chip carrier using the silver lacquer. The electrical contacts between electrodes on the sample and on the chip-carrier are constructed by Au or Al thread with a 25 μm diameter. This can be down by a specific machine, which joints the metal thread with the electrode by a ultrasonic shock. This is called the wire-banding, which is one of the most delicate step in the whole experiment. One should be very patient in this step.

Measurement inside a Helium 4 Cryostat

Once the wire-banding is successfully done, one can load the sample into the cryostat, which allows us to perform the measurements in a temperature region from 1.4K to 300K, with a magnetic field up to 8 Tesla. The conductance of the sample as a function of temperature or magnetic field can therefore be registered. The measured current and voltage signals are amplified and transferred to voltage signals, which are collected by the computer through a AD-DA card. The whole data collection process is controlled by a Labview programme. Below is the figure which gives a simple description to a Helium 4 cryostat.

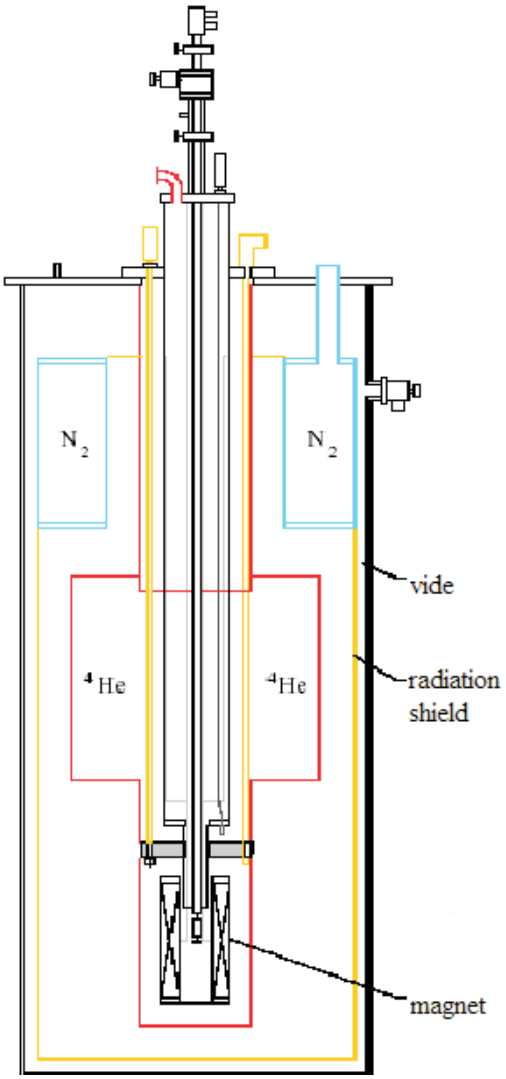

Figure 2.3: Schematic view of a Helium 4 Cryostat. The sample is to be loaded at the lower end of the rod in the middle.

Chapter 3

Non-invasive Four-terminal Measurements on Single Wall Carbon Nanotubes

Transport measurements has so far proven itself as a powerful tool to investigate the electronic properties of molecular systems [25]. Most often, individual molecular systems are electrically attached to two nano-fabricated electrodes. However, such two-terminal experiments do not allow the determination of the intrinsic resistance that results from the scattering processes involving, e.g. phonons or disorder. Indeed, the resistance is mainly dominated by poorly defined contacts that lie in series. A solution to eliminate the contribution of contacts has been found with scanning probe microscopy techniques [26, 27, 28, 29, 30], which enable the measurement of resistance variations along long systems such as nanotubes, however so far these techniques have only been applied at room temperature. The standard method to determine the intrinsic resistivity of macroscopic systems is the four-terminal measurement. However, the application of this technique to molecular systems is challenging, , since the metal electrodes used so far have been invasive. For example, nano-fabricated electrodes were shown to divide nanotubes into multiple quantum dots [31, 32].

To overcome this difficulty, we have designed a new four-terminal resistance measurements technique on single wall carbon nanotubes(SWNTs), which employs multiwalled carbon nanotubes(MWNTs) as noninvasive voltage electrodes. With this technique, we have found that SWNTs are remarkably good one-dimensional conductors with resistances as low as $1.5k\Omega$ for a 95nm long section. The resistance of

nanotube is shown to linearly increase with length at room temperature, in agreement with Ohm's law. At low temperature, however, the resistance can become negative and the amplitude then depends on the transmission coefficients at the different tube-probe interfaces. In this regime, four-terminal resistance measurements can be described by the Laudauer-Büttiker formalism [33, 34, 1], which takes into account quantum-interference effects.

This chapiter is organized as follows. In Sec. 3.1, we give a brief review of the previous efforts to measure the intrinsic resistance of SWNTs. In Sec. 3.2, we discuss the four-terminal resistance measurement in both the non-coherent and the coherent transport regime using Laudauer-Büttiker formula. In Sec. 3.3 we give a simple introduction to Coulomb Blockade (**CB**) oscillations of conductance, as we will use **CB** measurements to investigate the invasiveness of MWNTs as voltage probes. In Sec. 3.4 we give the details of our device fabrication technique, which mainly consist in moving MWNTs on the silicon oxide substrate to place them onto a SWNT. In Sec. 3.5 we give the various experimental evidences showing that MWNTs are non-invasive electrodes. The four-terminal resistance as a function of the tube length measured at room temperature, and the two-terminal coulomb blockade measurements will be presented. In Sec. 3.6 we discuss the four-terminal resistance measurements carried out at liquid Helium temperature. The interesting finding of negative four-terminal resistance strongly supports the predictions of the Laudauer-Büttiker formalism.

3.1 How to Probe the Intrinsic Resistance of a Single Wall Carbon Nanotubes ?

A disorder-free SWNT connected to ideal contacts is expected to display a conductance equal to $4e^2/h$, which is called the contact resistance R_c where the factor 4 comes from band and spin degeneracy. However, most often the contact between metal electrode and SWNT is not perfect, and there might be some disorder along the tube, the measured two-terminal resistance is a sum of quantum contact resistance R_c, tube-electrode interface resistance R_i, and the intrinsic resistance of a SWNT R_{in} due to static impurities, internal reflections due to tube bending effect and to phonon scattering, etc. Therefore the usual two-terminal measurements cannot give enough information to infer the actual intrinsic resistance of a SWNT.

A solution to eliminate the contribution of contacts has been found with scanning probe microscopy (**SPM**) techniques [26, 27, 28, 29, 30]. In these experiments, the **SPM** tips are used as movable electrodes, which enable the measurement of resistance variation along long systems such as nanotubes. However, these techniques have only been applied at room temperature.

The standard method to determine the intrinsic resistivity of a macroscopic system is the four-terminal measurement. Fig.3.1 below shows the principle of the measurement: a voltage bias is applied across the sample, maintaining a current I through the sample. Two voltage probes are attached to middle of the sample, a voltmeter is used to measure the voltage difference between both voltage probes. As there is no net current flowing through the voltage probes, the measured resistance $R = V/I$ does not depend on the contacts. Therefore the intrinsic resistance of the system can be obtained.

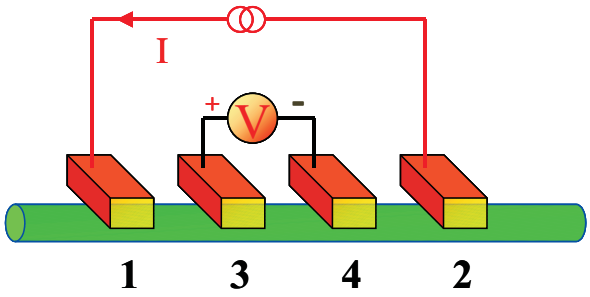

Figure 3.1: The setup of four-terminal resistance measurement: I is the current injected in 1 and extracted in 2 through the object, and V is the voltage difference between the two voltage probes 4 and 3. R=V/I gives the intrinsic resistance of the object.

However, the application of this technique to a SWNT is challenging, since the metal electrodes used so far have been invasive [31, 32]. The metal electrodes can damage the SWNT in two different ways.

Firstly, the metal electrodes may induce tunnel barriers into the SWNT. There are two different approaches to attach metal electrodes to a SWNT. The tube may be deposited on top of the prefabricated electrodes; or the electrodes may be evaporated on top of the tubes. In the former case, the mechanical bending within the tube may create successive quantum-dots inside the tube (as shown in Fig 3.2); in the latter case, though the origin is not very clear yet, electrodes also introduce barriers into

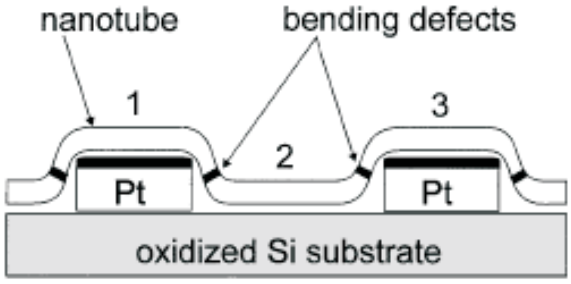

Figure 3.2: Mechanical bending within the tube create tunnel barriers near edges of electrodes inside the tube. The tube is divided into three quantum dots. One lies between two metal electrodes, and the other two lie on the top of electrodes.

the tube. The possible explanations are the damage by electron beam and the doping effect on the tube by metal electrodes.

Below is an example taken from Ref.[31]: Fig 3.3 shows a long SWNT deposited on prefabricated metal electrodes. At low temperature, two-terminal conductance measurements between non-adjacent electrodes give aperiodic Coulomb peaks, suggesting the existence of multiple quantum-dots along the measured SWNT. Further investigations suggest the location of the barriers is near the edge of the metal electrodes, where the barriers may be induced by bending of tube at the edge of the electrodes, as seen in Fig 3.2.

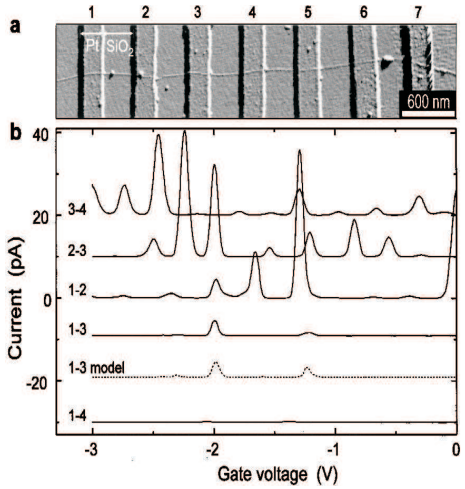

Figure 3.3: (a) AFM image showing a nanotube over prefabricated Pd electrodes. (b) Two-terminal measurements of the current versus gate voltage between various pairs of electrodes i-j at 4K. Curves are vertically offset for clarity.

Even if the electrodes cause no damage, the metal electrodes can be invasive in a more fundamental way. As seen in the Fig 3.4 below, an electron traveling in the SWNT can enter the voltage probe. As the voltage probe itself is electrically floating, no net current flows in or out of it, so another electron must come out. However, this electron can take either directions, this generates an additional resistance.

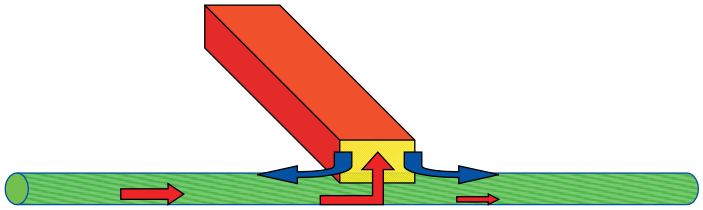

Figure 3.4: Additional back-scattering created by a voltage probe placed above a SWNT. Arrows show the incoming and outgoing electrons.

To investigate in detail this additional backscattering, we can start with the scattering matrix (S-matrix) related to the voltage probe. A S-matrix relates the outgoing wave amplitudes to the incoming wave amplitudes at different leads. Like the configuration in the Fig 3.5 below, the S-matrix which describes locally the voltage probe can be written as

$$\begin{pmatrix} b_1 \\ b_2 \\ b_3 \end{pmatrix} = \begin{pmatrix} a & \sqrt{\epsilon} & b \\ \sqrt{\epsilon} & c & \sqrt{\epsilon} \\ b & \sqrt{\epsilon} & a \end{pmatrix} \begin{pmatrix} a_1 \\ a_2 \\ a_3 \end{pmatrix} \tag{3.1.1}$$

Where b_i and a_i are outgoing and incoming wave fuction amplitudes of the electrode i, respectively, and $c = \sqrt{1-2\epsilon}$, $a = (1-c)/2$, $b = -(1+c)/2$, ϵ is the coupling parameter between the tube and the voltage probe [35]. Here we suppose there is no other static scattering center along the tube, and all metal electrodes make transparent contacts. The analysis below is made in the non-coherent transport regime.

The transmission probability T_{nm} between from m to n is obtained by the magnitude of the corresponding element of the S-matrix:

$$T_{nm} = |S_{nm}|^2 \tag{3.1.2}$$

The transmission probability matrix can be written as

$$\begin{pmatrix} a^2 & \epsilon & b^2 \\ \epsilon & c^2 & \epsilon \\ b^2 & \epsilon & a^2 \end{pmatrix} \tag{3.1.3}$$

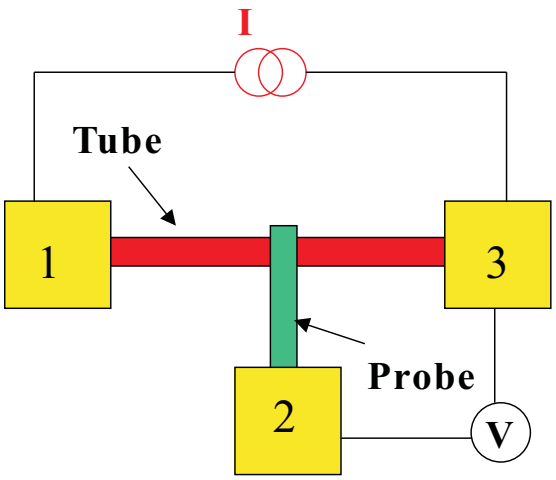

Figure 3.5: A three terminal device with which we calculate the additional resistance introduced by the probe.

Therefore the total transmission probability between tube and voltage probe $T_{tube-probe}$ is 2ϵ.

Using Büttiker formula, $I_m = 4\frac{e^2}{h}\sum_n [T_{nm}V_m - T_{mn}V_n]$, where V_m and I_m are the potential and the current of electrode m, respectively. We therefore have the following expression

$$\begin{pmatrix} I_1 \\ I_2 \\ I_3 \end{pmatrix} = \frac{4e^2}{h} \begin{pmatrix} T_{12}+T_{13} & -T_{12} & -T_{13} \\ -T_{21} & T_{21}+T_{23} & -T_{23} \\ -T_{31} & -T_{32} & T_{31}+T_{32} \end{pmatrix} \begin{pmatrix} V_1 \\ V_2 \\ V_3 \end{pmatrix} \tag{3.1.4}$$

On taking V_3 as zero, and using the Kirchoff's law ($I_1 + I_2 + I_3 = 0$), we can find the the following I-V relations:

$$\begin{pmatrix} I_1 \\ I_2 \end{pmatrix} = \frac{4e^2}{h} \begin{pmatrix} b^2+\epsilon & -\epsilon \\ -\epsilon & 2\epsilon \end{pmatrix} \begin{pmatrix} V_1 \\ V_2 \end{pmatrix} \tag{3.1.5}$$

from which we can find that the two-terminal resistance R_{2pt} between lead 1 and 3 is

$$R_{2pt} = \left[\frac{V_1}{I_1}\right]_{I_2=0} = \frac{1}{b^2+\epsilon/2}\frac{h}{4e^2} \tag{3.1.6}$$

therefore if the transmission probability between tube and voltage probe is around 0.4, we get an additional resistance $\approx 0.1\frac{h}{4e^2}$. In order to get rid of this additional resistance, the transmission probability $T_{tube-probe}$ between tube and voltage probe needs to be weak.

Experimentally, one can estimate the $T_{tube-probe}$ by measuring the resistance between the tube and voltage probe. We have

$$\begin{aligned} R_{tube-probe} &= \left[\frac{V_2}{I_2}\right]_{I_1=0} \\ &= \frac{1}{\epsilon}\frac{b^2+\epsilon}{2b^2+\epsilon}\frac{h}{4e^2} \\ &\approx \frac{1}{2\epsilon}\frac{h}{4e^2} = \frac{1}{T_{tube-probe}}\frac{h}{4e^2} \end{aligned} \tag{3.1.7}$$

in the weak coupling limit.

Above we have analyzed the invasiveness of voltage probes. In order to find the intrinsic resistance of a SWNT with four-terminal measurement technique, one need to attach some non-invasive voltage probes to a SWNT. We propose to use MWNTs as voltage probes, since the electrical transmission between two crossed nanotubes is low [36, 17]. These MWNTs can be attached to the SWNT by **AFM** manipulations. We will see in the Sec. 3.4 the details concerning how to place a MWNT onto a SWNT with the help of the **AFM** tips.

3.2 Laudauer-Büttiker Formalism

3.2.1 General Description of a Four-Terminal Device by the Laudauer-Büttiker Formalism

In this section we will give a brief introduction to the Laudauer-Büttiker formalism, which is the theory mostly employed in the description of multi-terminal electron transport in mesoscopic systems. Both non-coherent and coherent electron transport in a four-terminal system will be discussed.

The basic equation that describes the I-V relations in a multi-terminal structure is:

$$I_m = \sum_n [G_{nm}V_m - G_{mn}V_n] \tag{3.2.1}$$

where V_m and I_m are the potential and the current of electrode m, respectively; and G_{nm} is the conductance coefficient from the electrode m to the electrode n. We can express G_{nm} with the transmission coefficient T_{nm}:

$$G_{nm} = 4\frac{e^2}{h}T_{nm} \tag{3.2.2}$$

where the factor 4 comes from the fact that there are 2 spin-degenerated transport channels at the Fermi level of a SWNT.

Therefore the I-V relations in a four-terminal device as described in the Fig 3.6 can be written as

$$\begin{pmatrix} I_1 \\ I_2 \\ I_3 \end{pmatrix} = \frac{4e^2}{h} \begin{pmatrix} T_{12}+T_{13}+T_{14} & -T_{12} & -T_{13} \\ -T_{21} & T_{21}+T_{23}+T_{24} & -T_{23} \\ -T_{31} & -T_{32} & T_{31}+T_{32}+T_{34} \end{pmatrix} \begin{pmatrix} V_1 \\ V_2 \\ V_3 \end{pmatrix} \tag{3.2.3}$$

We have taken the voltage V_4 to be zero, and $I_1 + I_4 = 0$.

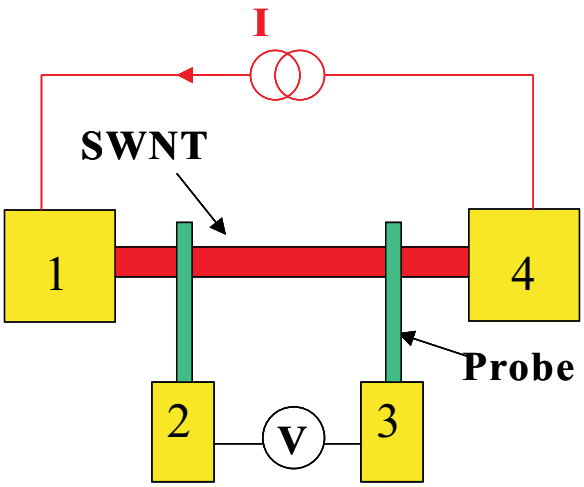

Figure 3.6: A four-terminal measurement setup on a SWNT. The current I flowing from terminal 1 to 4. A voltage drop V is measured between the floating terminal 2 and 3.

We now take the reciprocal of the transmission matrix, then we have

$$\begin{pmatrix} V_1 \\ V_2 \\ V_3 \end{pmatrix} = \mathbf{R} \begin{pmatrix} I_1 \\ I_2 \\ I_3 \end{pmatrix} \tag{3.2.4}$$

where the resistance matrix [**R**] is given by

$$\mathbf{R} = \frac{h}{4e^2} \begin{bmatrix} T_{12}+T_{13}+T_{14} & -T_{12} & -T_{13} \\ -T_{21} & T_{21}+T_{23}+T_{24} & -T_{23} \\ -T_{31} & -T_{32} & T_{31}+T_{32}+T_{34} \end{bmatrix}^{-1} \tag{3.2.5}$$

The four-terminal resistance R_{4p} measured in the configuration shown in Fig 3.6 is given by

$$R_{4p} = \frac{V}{I} = \left[\frac{V_2 - V_3}{I}\right]_{I_2 - I_3 = 0} = R_{21} - R_{31} \tag{3.2.6}$$

Therefore our goal is to calculate the transmission matrix $[T_{nm}]$.

3.2.2 Non-coherent Electron Transport Regime

We first treat the electron motion classically, therefore we do not worry about any interference effect. We will take a simple model shown in the Fig 3.7. This is a SWNT contacted by four electrodes, among which electrodes 1 and 4 are current probes, electrodes 2 and 3 are voltage probes. Supposing there are three static scatters along

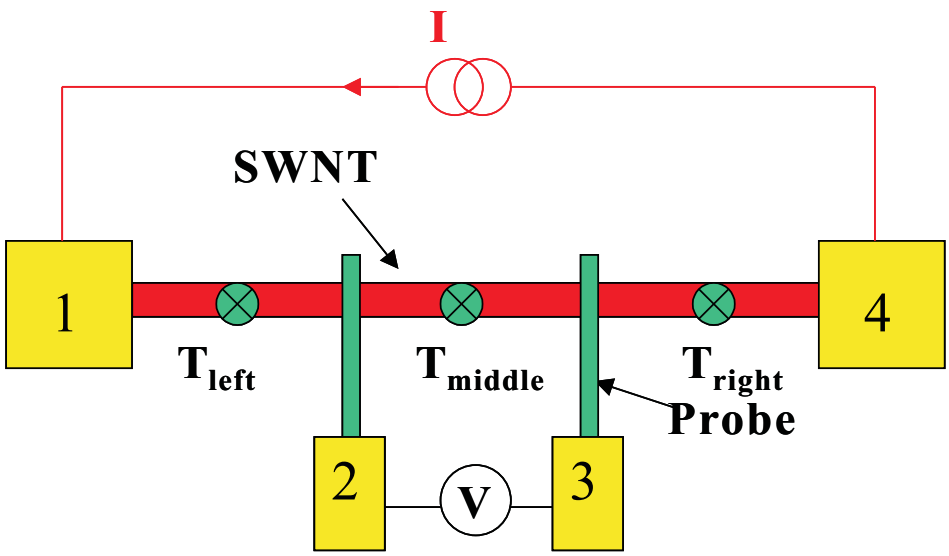

Figure 3.7: A four-terminal measurement setup on a SWNT, along which lie three static scatterers. One to the left of electrode 2 is called T_{left}, where T_{left} also signifies its transmission probability. T_{right} and T_{middle} are defined in the same way.

the tube, each can be characterized by a (2×2) scattering matrix

$$\begin{pmatrix} i\sqrt{1-T_i} & \sqrt{T_i} \\ \sqrt{T_i} & i\sqrt{1-T_i} \end{pmatrix} \tag{3.2.7}$$

where T_i is the transmission probability of the static scattering center i.

The effect of voltage probes, as we have seen in the first section, can be described by a (3×3) scattering matrix

$$\begin{pmatrix} a & \sqrt{\epsilon} & b \\ \sqrt{\epsilon} & c & \sqrt{\epsilon} \\ b & \sqrt{\epsilon} & a \end{pmatrix} \tag{3.2.8}$$

where $c = \sqrt{1-2\epsilon}$, $a = (1-c)/2$, $b = -(1+c)/2$, ϵ is the coupling parameter between the tube and the voltage probe.

These scattering matrix relate the outgoing electron wave amplitudes to the incoming electron wave amplitudes. What we need to do now is to combine all these

scattering matrix together to find the total transmission matrix. Because we are in non-coherent transport regime, we may neglect the phase factor of the electron wave. Instead of combining successive scattering matrix, we can combine directly the probability matrix to get the total transmission matrix. The probability matrix is obtained by taking the squared magnitude of the corresponding element of the scattering matrix, therefore we have the following probability matrix related to the static scattering center

$$\begin{pmatrix} 1-T_i & T_i \\ T_i & 1-T_i \end{pmatrix} \tag{3.2.9}$$

and to the voltage probe

$$\begin{pmatrix} a^2 & \epsilon & b^2 \\ \epsilon & c^2 & \epsilon \\ b^2 & \epsilon & a^2 \end{pmatrix} \tag{3.2.10}$$

The method to combine different probability matrix into a composite matrix is described in [1]. We give in the appendix the Mathematica programme for details of the calculation. We present here the main results of the calculation.

1. The calculated four-terminal resistance R_{4p} does not depend on the transmission probabilities T_{left} and T_{right} as shown in the Fig 3.8 below. The similar dependence on T_{left} can also be obtained.

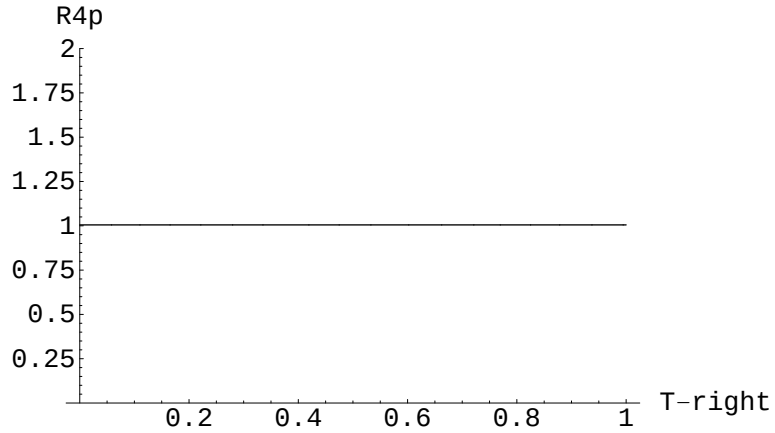

Figure 3.8: Four-terminal resistance R_{4p} as a function of the transmission T_{right}, with T_{left}=0.1, $T_{middle} = 0.5$, $\epsilon_{1,2} = 0.01$, the R_{4p} is in unit of $\frac{h}{4e^2}$.

2. The calculated four-terminal resistance R_{4p} does depend on the coupling $\epsilon_{1,2}$ between voltage probes and the SWNT, as seen in Fig 3.9. The four-terminal resistance increases with the coupling strength ϵ, as we have seen in the first section,

this is due to the additional backscattering caused by the voltage probes. For weak coupling between the voltage probe and the SWNT, R_{4p} tends to $\frac{h}{4e^2}\frac{1-T_{middle}}{T_{middle}}$, which is the intrinsic resistance of the SWNT as we will see below.

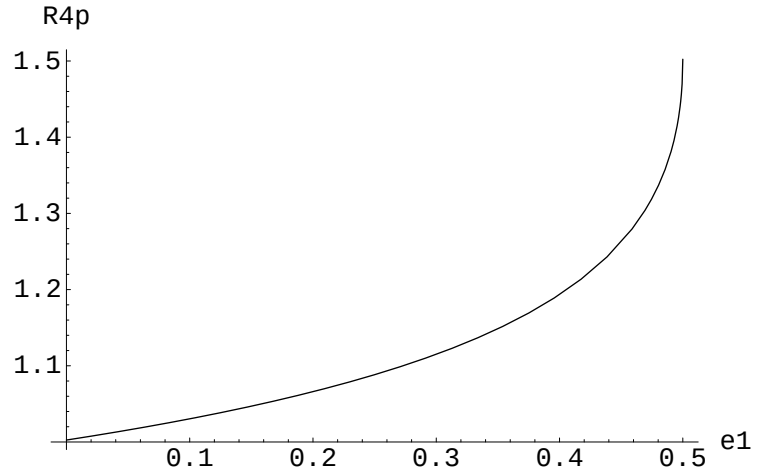

Figure 3.9: Four-terminal resistance R_{4p} as a function of the the coupling strength ϵ_1, with $T_{left} = T_{right} = 0.1$, T_{middle}=0.5, $\epsilon_2 = 0.01$, the R_{4p} is in unit of $\frac{h}{4e^2}$.

3. In case that the coupling between the voltage probes and the SWNT is weak, the four-terminal resistance R_{4p} is only a function of T_2. This means that R_{4p} describes only the intrinsic resistance between the two voltage probes. Indeed, the above curve

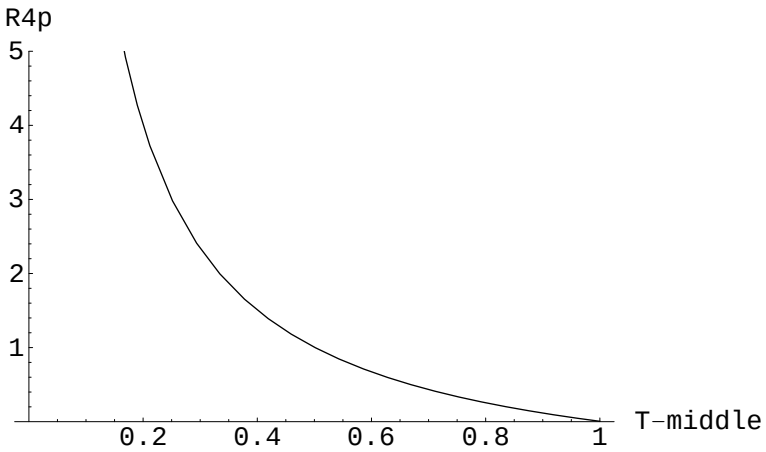

Figure 3.10: Four-terminal resistance R_{4p} as a function of the transmission T_{middle}, with T_{left}=0.1, $T_{right} = 0.1$, $\epsilon_{1,2} = 0.01$, the R_{4p} is in unit of $\frac{h}{4e^2}$.

takes a form of $(1 - T_{middle})/T_{middle}$, as seen in Fig 3.10. We can understand this result using the description in [1].

Supposing there are several static scattering center lying in series along the SWNT between the two voltage probes. The measured four-terminal resistance should be the sum of the resistance related to each scatterer. We start by a simple case: two scatterers with transmission probability T_1 and T_2 are located inside the SWNT. To obtain the total transmission probability T_{12} we need to take into account all the multiple reflections of electron between both scatterers. As we neglect the interference, the total transmission probability is:

$$\begin{aligned} T_{12} &= T_1T_2 + T_1T_2R_1R_2 + T_1T_2R_1^2R_2^2 + ... \\ &= \frac{T_1T_2}{1 - R_1R_2} \end{aligned} \tag{3.2.11}$$

with $R_{1,2} = 1 - T_{1,2}$ is the reflection probability of both scatterers.

We can rewrite the above result in the following form:

$$\frac{1 - T_{12}}{T_{12}} = \frac{1 - T_1}{T_1} + \frac{1 - T_2}{T_2} \tag{3.2.12}$$

The fact that the quantity $(1 - T_i)/T_i$ has an additive property suggests that the resistance of an individual scatterers is proportional to it. Therefore, if there are N scatterers lying along the SWNT, each has a transmission probability T, the total resistance of these scatterers should proportional to $(1 - T(N))/T(N)$, where $T(N)$ is the total transmission probability satisfying

$$\frac{1 - T(N)}{T(N)} = N\frac{1 - T}{T} \tag{3.2.13}$$

This explains the above calculated four-terminal resistance R_{4p} taking a form of $\frac{1-T}{T}$.

We can further relate the four-terminal resistance to the elastic mean-free path of electron in a SWNT. Rewrite $T(N)$ in the following expression:

$$T(N) = \frac{T}{N(1 - T) + T} \tag{3.2.14}$$

Provided the separation between two voltage probes is L, and ρ is the mean linear density of the scatterers, we can define the elastic mean-free path of electron in SWNT $l_e \equiv \frac{T}{\rho(1-T)}$, the total transmission $T(N)$ can be written as

$$T(L) = \frac{l_e}{L + l_e} \tag{3.2.15}$$

We can find

$$R_{4pt} = \frac{h}{4e^2}\frac{1 - T}{T} = \frac{h}{4e^2}\frac{L}{l_e} \tag{3.2.16}$$

The four-terminal resistance in non-coherent transport regime can therefore provide direct information about the elastic mean-free path of electron in a SWNT.

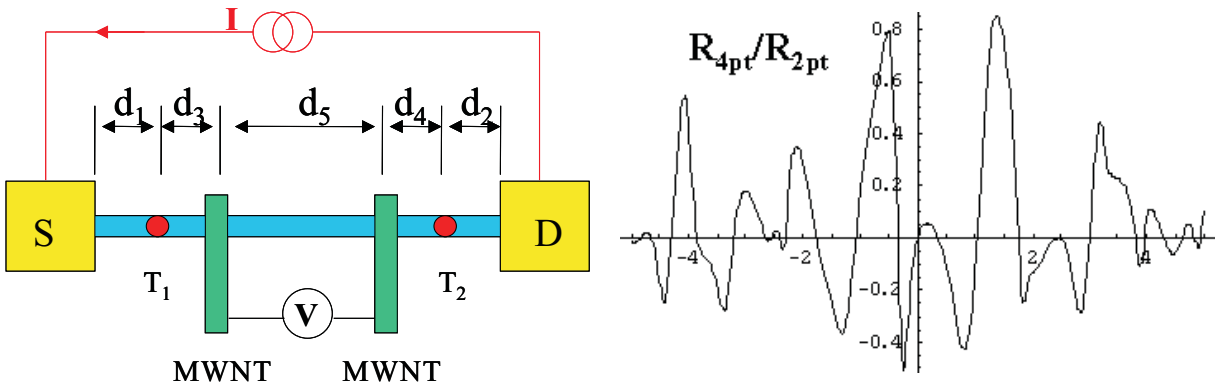

Figure 3.11: (a) The four-terminal resistance measurement on a SWNT inside which there is two static scattering center. (b) The calculated resistance ratio R_{4pt}/R_{2pt} as a function of the wave vector k of the electron wave inside the SWNT.

3.2.3 Coherent transport regime

Above we discussed the four-terminal measurement in the non-coherent transport regime. This is valid for high temperature measurements where the electron-phonon interaction strongly decreases the phase coherence length of electrons. When decreasing the temperature, the phase coherence length increases. At low temperature, the phase coherence length of electron may become close to even longer than the sample size [37, 38]. In this case, one cannot neglect the interference effects of electron waves. Therefore, to calculate the total transmission matrix, one needs to combine the successive scattering matrix coherently.

We will take a very simple model to get some intuition. We suppose that there are two static scatterers lying in the SWNT, as seen in Fig 3.11. The electron wave will also be scattered by both voltage probes. The related scattering matrix are the same as in Eq.3.2.7 and Eq.3.2.8. We also suppose that the electron propagate freely between scatterers. Therefore it will acquire a phase factor e^{ikl} after traveling a distance l. The method to combine the scattering matrix coherently is also given in Ref [1]. We give in the appendix the complete Mathematica programme for the detailed calculation. The numerical simulations below show clearly the modulations of R_{4pt}/R_{2pt} as a function of wave vector k. We find the very interesting phenomenon that the four-terminal resistance can be negative. This can be understood in the following way.

We go back to Büttiker formula,

$$I_p = 4\frac{e}{h}\sum_q [T_{qp}\mu_p - T_{pq}\mu_q] \tag{3.2.17}$$

where μ_q is electro-chemical potential of the electrode q. From this formula, one can easily find the resistance ratio R_{4pt}/R_{2pt} given by

$$\begin{aligned}\frac{R_{4pt}}{R_{2pt}} &= \frac{\mu_3 - \mu_4}{\mu_1 - \mu_2} \\ &= \frac{T_{13}T_{24} - T_{23}T_{14}}{(T_{13} + T_{23} + T_{43})(T_{14} + T_{24} + T_{34}) - T_{43}T_{34}}\end{aligned} \tag{3.2.18}$$

As we are in coherent transport regime, the incident and reflected electron waves interfere with each other. Therefore, when varying the electron wave vector k, we get different interference pattern, which enable the sign reversal of the numerator in Eq.3.2.18.

3.3 Introduction to Coulomb Blockade Oscillations of Conductance

As we will use Coulomb Blockade (**CB**) measurements to determine the invasiveness of MWNTs as voltage probes, we give a simple introduction to **CB** in this section to get some intuition.

Coulomb Blockade oscillations of the conductance are the manifestation of single electron tunneling through a quantum dot. The conductance oscillates as the voltage V_g of a nearby gate electrode is varied. We now seek to understand the origin of this conductance oscillation phenomena.

The Fig 3.12 below is simple model of of a quantum dot contacted to the external electron reservoir through tunnel junctions. The linear response conductance of a quantum dot is defined as $G \equiv I/V$, in the limit $V \to 0$. At low temperature, the electron tunneling is usually blocked. This is due to the large charging energy of the quantum dot. The capacitance C of a quantum dot is small, therefore putting an additional electron into a quantum dot will cost a significant of energy (in the order of e^2/C), the energy. However, in certain situation, adding an electron into the dot costs no energy, the **CB** is therefore lifted.

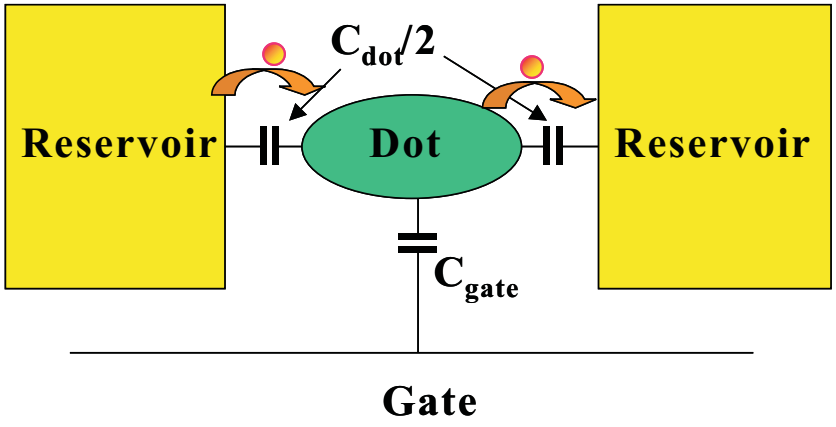

Figure 3.12: A schematic view of a quantum dot contacted to the external electron reservoir through tunnel junctions. The capacitance C of the dot is defined as $C = C_{gate} + C_{dot}$. Because the size of the dot is very small, the charging energy of the dot $E_c = e^2/C$ is rather large, the electron can be only added one by one into the dot.

At equilibrium, the probability $P(N)$ to find N electron in the quantum dot is given by the following expression [39]:

$$P(N) = constance \times exp(-\frac{1}{k_B T}[F(N) - NE_F]) \tag{3.3.1}$$

where N is the number of electrons in the dot, F(N) is the free energy of the dot, and E_F is the Fermi energy of the electron reservoir measured of the bottom of the conduction band. At zero temperature, P(N) is non-zero only for a single value, which is the integer that minimize the thermodynamic potential $\Omega(N) \equiv [F(N) - NE_F]$. In order to get a non-zero linear response conductance, P(N) and P(N+1) must be both non-zero, so that a very small voltage can induce a current through the dot. In order that both P(N) and P(N+1) are non-zero, that means both N and N+1 minimize the thermodynamic potential Ω, the necessary condition is $\Omega(N+1) = \Omega(N)$, which gives

$$F(N+1) - F(N) = E_F \tag{3.3.2}$$

At zero temperature, the free energy of the dot can be written as

$$F(N) \equiv U(N) + \sum_{p=1}^{N} E_p \tag{3.3.3}$$

where U(N) is the charging energy, and E_p is the single electron energy level in the dot. Substituting Eq.3.3.3 into Eq.3.3.2, one can find the new condition for the

conductance peak

$$E_N + U(N) - U(N-1) = E_F \tag{3.3.4}$$

The charging energy U(N) can be calculated from the orthodox model [40], it takes the form

$$\begin{aligned} U(N) &= \frac{(Ne)^2}{2C} - Ne\phi_{ext} \\ &= \frac{(Ne - Q_{ext})^2}{2C} + constant \end{aligned} \tag{3.3.5}$$

where ϕ_{ext} is the potential difference between the dot and the reservoir induced by the external charge, $C = C_{gate} + C_{dot}$ is the capacitance of the dot, and $Q_{ext} \equiv C\phi_{ext}$ is the so-called "externally induced charge" on the dot, which can be varied continuously.

Using the explicit expression of U(N), the condition for conductance peak is

$$E_N + (N - 1/2)\frac{e^2}{C} = E_F + e\phi_{ext} \tag{3.3.6}$$

when sweeping ϕ_{ext}, the number of electrons in the dot will be changed one by one.

From the above equation one can determine the periodicity of the conductance oscillation. As the spin degeneracy of the levels in the dot is lifted by the charging energy, the oscillation will have a doublet structure in case that the level separation ΔE is on the same order to the charging energy $E_c = e^2/C$. If $E_c >> \Delta E$, the charging energy will regulate the spacing, and a periodic oscillation can be expected.

To determine the oscillation period as the function of the gate voltage, one can use the following relation:

$$\Delta\phi_{ext} = \alpha\Delta\phi_{gate} \tag{3.3.7}$$

where ϕ_{gate} is the gate voltage and α is the coupling coefficient, which can be roughly estimated as $\alpha = C_{gate}/C = C_{gate}/(C_{gate} + C_{dot})$. Therefore the spacing of the gate voltage between successive conductance peak will be $\frac{E_c}{\alpha e}$ and $\frac{E_c + \Delta E}{\alpha e}$, depending on the number of electrons in the dot. This so-called even-odd effect has been observed in the transport measurement in the nanotube quantum dot [41].

Indeed for a metallic SWNT, Coulomb Blockade effect can be rather complicated. When taking into account the spin of electron and the fact that there are two crossing bands at the Fermi level, the conductance oscillations should be described by a model with five parameters: the charging energy E_c, the quantum energy-level separation ΔE, the band mismatch δ, the exchange energy J, and the excess Coulomb Energy

dU. The exchange energy favors spin alignment and the excess Coulomb energy is the extra charging energy associated with placing two electrons in the same energy level. Detailed description of this model and the experimental description can be found in Ref. [42, 43].

3.4 How to Move Carbon Nanotubes with AFM Tips ?

Above we discussed the theoretical aspect of the four-terminal resistance measurements using the Landauer-Büttiker formalism. We now turn to the experimental aspect of the measurement. In this section we give a detailed description of the fabrication technique of our samples. In general, the samples are fabricated with standard nano-fabrication techniques. In our experiments, two types of SWNTS are used. One is the $\approx 1nm$ diameter SWNT grown by laser-ablation [10], the other is the SWNT grown by chemical-vapor deposition [44]. In the former case, nanotubes are dispersed from a suspension in dichloroethane onto a silicon oxide wafer; while in the latter case, $\approx 1nm$ diameter SWNTs are grown directly on the silicon oxide substrate.

After that the SWNTs have been placed onto the wafer, MWNTs are dispersed onto the same wafer from a suspension in dichloroethane. Cautions need to be taken while controlling the density of MWNTs. If not, short-circuits may make the analysis more complicated. We then select the proper SWNTs with atomic force microscopy(**AFM**). Sometimes we are lucky enough to find one or more MWNTs already falling upon a SWNT; more often we need to move the nearby MWNTs and put them above the selected SWNTs using **AFM** manipulation. We explain below in details how to do it.

AFM has different working modes. In order to avoid the nanotubes being damaged by mechanical contacts with **AFM** tip, we normally choose non-contact working mode. This is one among several vibrating cantilever techniques in which an **AFM** cantilever vibrates near the surface of a sample. The spacing between the tip and the sample is on the order of tens to hundreds of angstroms.

To move a MWNT with the tip, mechanical contact between tip and tube is necessary (**AFM** contact mode operation). We first need to decrease the scanning area to less than $0.1\mu m \times 0.1\mu m$, then move the tip to the position right above a

MWNT. We next turn down the feedback control on the scanner. In order to make less damage to the sample, we decrease the vibrating force applied on the cantilever, for e.g. to 10% of its original value. Then, by monitoring the signal $A-B$ that indicate the amplitude of the vibration of the tip, we can manually decrease the separation between tip and substrate. As the tip touches the surface of the substrate, this signal decreases to zero. We can then move the tip, which pushes the MWNTs towards the selected SWNT. The figure below gives a simple illustration to the manipulation of a MWNT using the **AFM** tip.

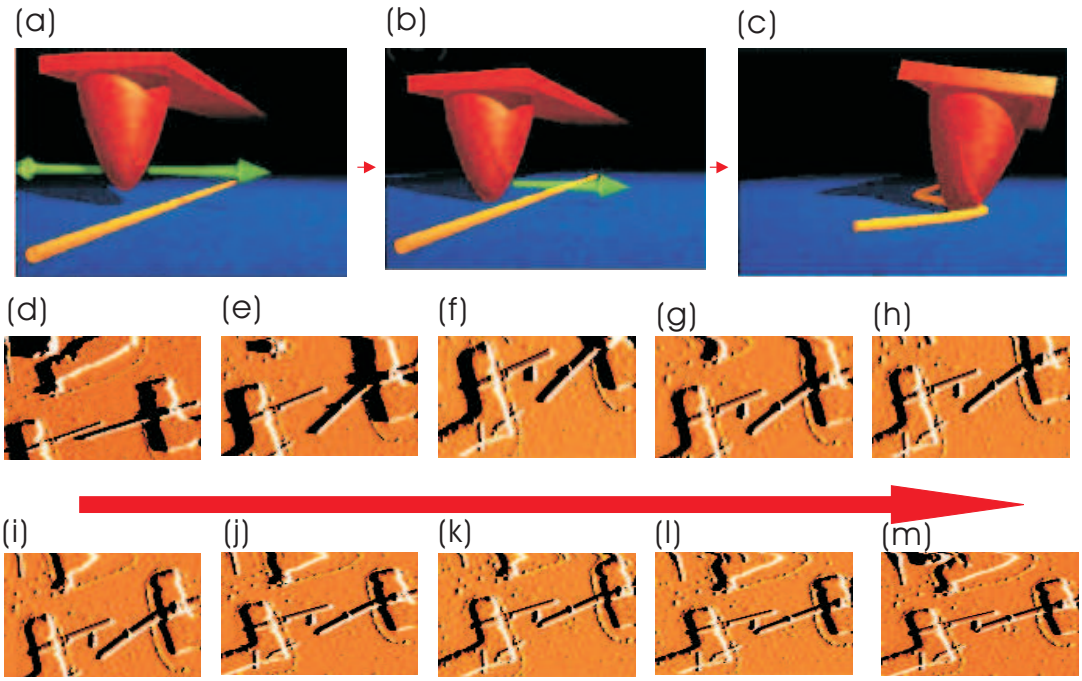

Figure 3.13: (a) Move the **AFM** tip to an appropriate place over the MWNT. (b) Decline the tip until it touches the substrate surface. (c) Move the MWNT with the **AFM** tip. The three images are taken from the website of IBM T. J. Watson research center. Images from (d) to (m) show how we change the separation between two MWNTs with a tip of AFM, even the MWNTs have been contacted by metal electrodes.

The above manipulations need to be repeated tens of times before a MWNT is placed to a good position nearby the selected SWNT. The main difficulty lies in the fact that the surface of the substrate is often slightly tilted with respect to the horizontal tip motion. Therefore the tip may lose the contact with the MWNT (we may find the signal $A - B$ increases), or plunge too much into the substrate causing grave damage to itself and to the substrate. In such case, we need to go back to

non-contact mode, retake the image of the area, and repeat the above manipulations. Sometimes we may manually change the tip-substrate separation to compensate the orientation of the surface when moving a MWNT, however it may often accelerate the damaging process of the tip.

Once a MWNT is placed close enough to a SWNT, one have to put it across the selected SWNT. This may be the most difficult part of the sample fabrication. The key point is to avoid the mechanical contact between the tip and the SWNT, for that it will easily create a kink in the SWNT thus damaging it. We have found two solutions.

The first one needs a long SWNT. We place the MWNT near the end of the SWNT, make them crossed, then push the MWNT step by step towards the other end of the SWNT. Though we may damage the end part of the SWNT, it will not be a problem so far as it is not involved in the future resistance measurement.

The other solution demands a large diameter MWNT, typically larger than $10nm$. Such a MWNT is rigid enough to behavior like a stick. We may place a MWNT close to a SWNT, pushing its far end to make a rotation, and the MWNT will cross the SWNT.

We need precise here that this technique is time-consuming. It normally take several hours to put two MWNTs onto a SWNT. And sometimes the MWNT may be picked up by the AFM tip. Therefore one needs to restart the work. Also the AFM tip itself may be damaged because of the frequent contacts with the substrate. One may need to change the point and it also take time to optimize again all the working conditions.

Despite of all these difficulties, with the technique presented above, we can put two or more MWNTs above a SWNT. Using standard nano-fabrication techniques, metal electrodes can be attached to the nanotubes allowing us to carry out four-terminal resistance measurements on a SWNT.

3.5 How to Decide the Invasiveness of MWNTs as voltage Probes ?

In the previous section, we have presented the technique to displace a MWNT with an AFM tip. With this technique, we can fabricate devices which allow us to realize

	R_{4pt} (kΩ)	L (nm)	l_e (nm)	$L_{Au\text{-}Au}$ (μm)		
Device 1	1.5	95	408	2.7	SGS*	CVD
Device 2	37.0	100	17	5.6	SC**	LA
Device 3	2.7	150	358	1.0	metal	CVD
Device 4	6.3	140	143	0.6	metal	LA
Device 5	12.7	590	300	1.4	metal	LA

Table 3.1: Device characteristics at 300 K. L is the separation between the MWNTs and L_{Au-Au} between the Au electrodes. * Small-gap semiconductor with the current reduction occurring at V_g >2 V. ** Large-gap semiconductor with the threshold voltage at $\sim$ 40 V. LA = laser ablation. CVD = chemical vapor deposition.

a four-terminal resistance measurement on a SWNT using MWNT as voltage probe. Fig 3.14 describes a typical device.

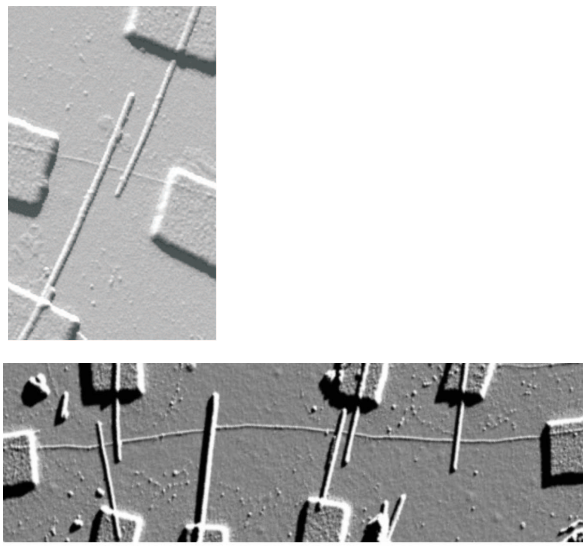

Figure 3.14: (a) Atomic force microscopy image of a SWNT contacted by 2 MWNTs and 2 Au electrodes. (b)Atomic force microscopy image of a SWNT contacted by 6 MWNTs and 2 Au electrodes.

In this section, we present our experimental measurements in order to determine that the MWNTs are non-invasive voltage probes to the SWNT. The table 4.1 below describes the device characteristics at 300K.

3.5.1 Measurements done at Room Temperature

As we have seen in the previous sections, the voltage probes may perturb significantly the electron transport in the SWNT. Therefore we need to determine how much

invasive are the MWNT probes. All the measurements at room temperature have been carried out in the linear regime, which means the applied voltage between both ends of the SWNT is always much less than the $k_BT \approx 25meV$.

We first measure the junction resistances between SWNTs and MWNTs. We find these resistances are of the order of several hundreds $k\Omega$, therefore the transmission probabilities between SWNTs and MWNTs are less than 10^{-2}. As explained in the first section, such weak coupling between tube and probe will not cause strong additional back-scattering.

We next need to determine whether MWNT probes create strong barriers along SWNTs and therefore divide SWNTs into multiple quantum dots. As reported in previous measurements, nano-fabricated metal electrodes do separate SWNTs into multiple dots. Are MWNT probes better in this respect?

To answer the question, we first investigate the four-terminal resistance of a function of the tube length at room temperature. In order to find this length dependence, two types of measurements are performed (See Fig 3.15).

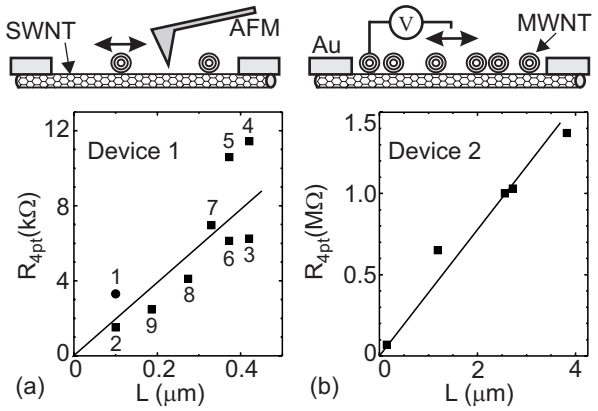

Figure 3.15: Length dependence of R_{4pt} at room temperature and $V_g = 0$. (a) SWNT contacted by 2 MWNTs. One MWNT is displaced back and forth with an AFM tip. Points are numbered to describe the measurement sequence. Point 1 has been acquired one week before in the cryostat. Most points have been recorded while decreasing L, so that the R enhancement with L is not due to a structural degradation during the manipulation. (b) SWNT contacted by 6 MWNTs.

The first one is carried out under **AFM**. The tip of **AFM** is used to change the separation **L** between two MWNTs. One MWNT is moved back and forth with the tip. We find the R_{4pt} increases linearly with the separation between MWNTs. Note that most of the data are recorded when decreasing L, therefore one can nearly

exclude the possibility that the increase of R_{4pt} is due to sequential manipulations of MWNT that may create some disorder along the studied SWNT. In addition, R_{4pt} tends to zero as the length is reduced to zero. This suggests also that MWNTs are mainly noninvasive. If not, a significant resistance contribution from the MWNTs would give a finite R_{4pt} at zero length, which is in opposition to the measurements. However, the measurements in Fig 3.15(a) show rather large scatterers. This may come from the **AFM** manipulation that stretches the tube, deposits or removes some molecules absorbed on the SWNT, or modifies the pressure applied by the MWNT on the SWNT. Thus, we cannot exclude completely a small resistance perturbation from the MWNTs and/or the AFM manipulation.

The other way to find the length dependence of R_{4pt} is realized upon a very long SWNT. Six MWNTs are placed on this SWNT, enabling the four-terminal resistance measurement of multiple portions. We find also the resistance increases linearly with tube length, and tends to zero as the length is decreased to zero. Here the measured resistance is large. To date, the origin of the large resistance is not clear. A possible explanation is related to the sample fabrication processes, which involves the separation of isolated tubes from bundles with the help of ultrasonic that can induce disorder inside the tube.

With the measurements presented above, we conclude that SWNTs are classical resistor at room temperature, which obey Ohm's law. And more importantly, for both types of measurements done, R_{4pt} tends to zero as the length is reduced to zero, which suggests no (or very weak) additional resistance from the voltage probes.

3.5.2 Coulomb Blockade Measurements at cryogenic Temperature

We further use Coulomb Blockade (**CB**) measurements to investigate the invasiveness of MWNT probes. Two types of two-terminal conductance measurement were performed. We first measured the conductance between two current probes, as seen in Fig 3.16(a); we then measured the conductance between two voltage probes, as seen in Fig 3.16(b).

We see in Fig 3.17 that conductance peaks are found at the same V_g for conductance measurements between different pairs of electrodes. Some devices even show a series of **CB** peaks that appear regularly when sweeping the gate voltage V_g of the

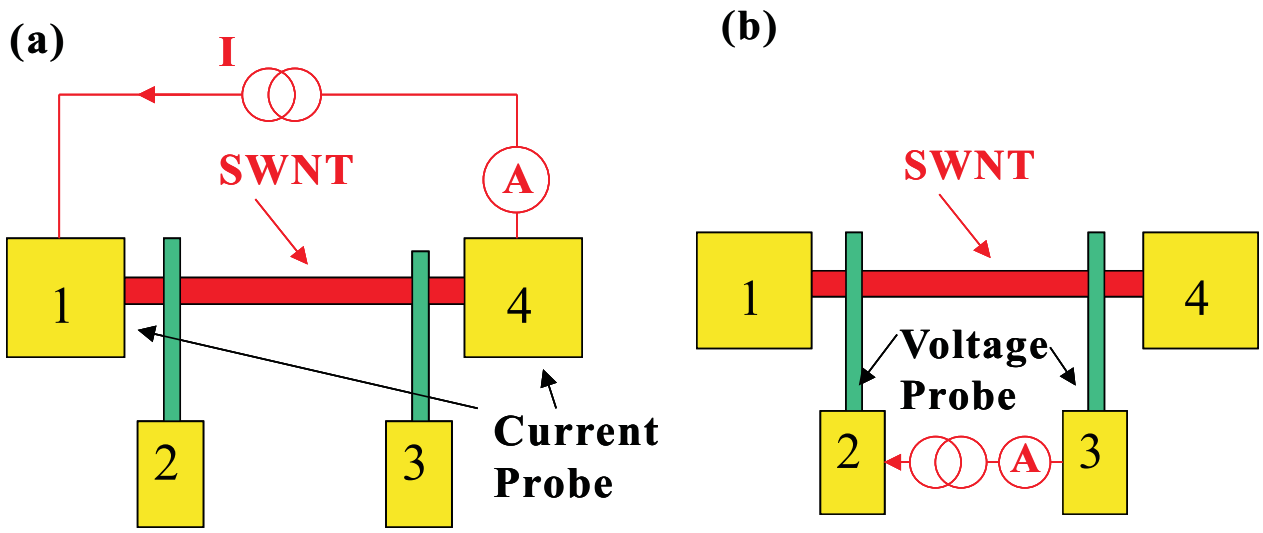

Figure 3.16: Two-terminal conductance measurement as a function of V_g (not shown in the figure). (a) Au-Au: conductance between two gold current probes. (b) MWNT-MWNT: conductance between two MWNTs as voltage probes.

back gate. This indicate that gold current electrodes and MWNT voltage electrodes probe the same quantum dot. Coulomb diamonds measurements give that the charging energy $E_c \approx 5meV$. It has been shown that $E_c \approx 5meV/L[\mu m]$ for similarly prepared samples [11, 32]. The dot length is thus $\approx 1\mu m$, which is consistent with the actual 600 nm length separation between gold current electrodes. These measurements suggest that MWNTs are sufficiently noninvasive not to divide the SWNT into multiple quantum dots. In addition, the fact that a single dot extends over the total length of SWNT suggests also what we have an isolated SWNT, not a bundle of tubes nor small diameter MWNTs.

There are also some devices showing irregular Coulomb Blockade peaks. This probably results from the disorder along the SWNT. Interestingly, the Coulomb Blockade peaks in these devices appear in pairs (see Fig 3.18(a)). This is better seen in the Fig 3.18(b). The separation between Coulomb Blockade peaks goes up and down as the gate voltage is swept. The peak separation reflect the energy needed to add an additional electron into the dot. This even-odd alternation suggests two-electron shell filling [41]. As we have seen in the Sec.Three, because of Pauli's principle, the spin of the ground state alternates by 1/2 as consecutive electrons are added. For an electron number N in the dot that is odd, the N+1 electron enters the same orbital

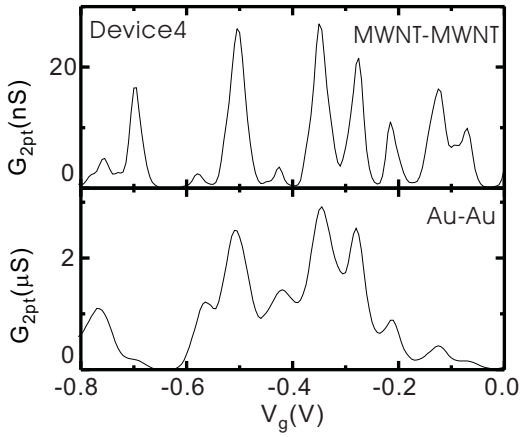

Figure 3.17: Two-terminal conductance as a function of V_g at 1.4 K. CB peaks measured between different electrodes are found at the same V_g. In addition, **CB** peaks appear regularly when sweeping the gate voltage V_g. Similar behaviors were observed in the Device 3.

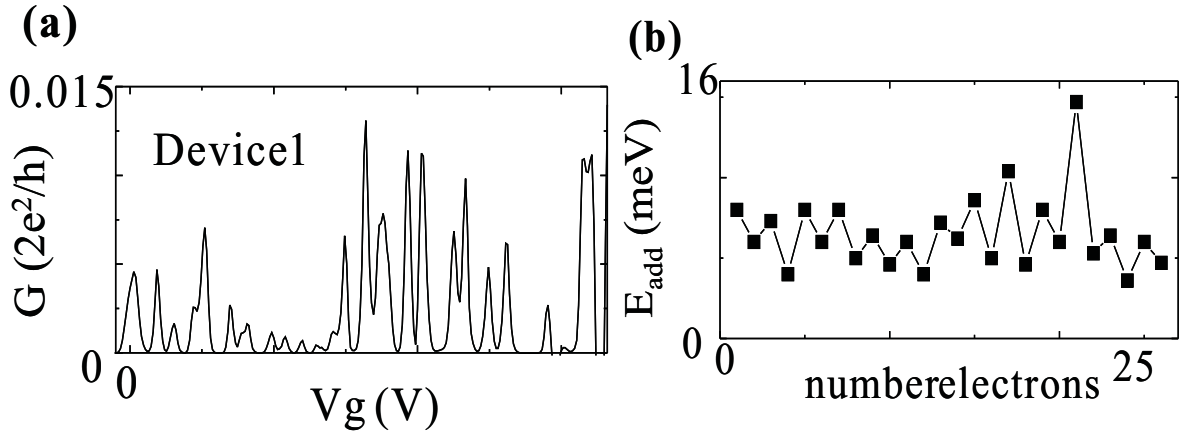

Figure 3.18: (a) Two-terminal conductance measured between the two Au current probes as a function of the gate voltage at 1.5 K in device 1. The conductance oscillations show a doublet structure. (b) The addition energy for adding one electron into the dot as the function of number of electrons in the dot. Measurements show clearly an even-odd effect corresponding to a two-electron shell filling.

as the N electron, The resulting separation of **CB** peaks is E_c/α with α is the coupling efficiency. For even N, the N+1 electron enters the next orbital. The resulting separation is then $(E_c + \Delta E)/\alpha$. Using $\alpha = 1/6$ measured from Coulomb diamonds, we obtain an averaged $\Delta E = 0.5meV$. The level spacing is related to the length L_{dot} of the dot through

$$\Delta E = \frac{hv_F}{2L_{dot}} \tag{3.5.1}$$

where $v_F \approx 8 \times 10^5 m/s$ is the Fermi velocity of the SWNT. We get $L_{dot} \approx 2.9\mu m$, which is very close to the $2.7\mu m$ separation between the gold current electrodes. This is in any case much longer than the 95nm separation between the MWNTs.

In general, these **CB** measurements suggest that MWNTs are sufficiently non-invasive to not divide the SWNT in multiple quantum dots. This is in agreement with measurements of the length dependence of the four-terminal resistance at room temperature.

3.6 Coherent Electron Transport at cryogenic Temperature

In the previous section we have presented the measurements carried out at room temperature, and we found that the SWNT behaves like a classical resistor at this temperature. In this last section, we explore the four-terminal electron transport properties of SWNT at low temperature. Our measurements are still done in linear regime with a bias voltage smaller than $k_B T/e$.

Upon decreasing the temperature, R_{4pt} does not change for T $\gtrsim 60K$, as seen in Fig 3.19, suggesting that the intrinsic resistance is related to some static disorder and not to phonons. At lower temperature, R_{4pt} starts to depend on the gate voltage V_g.

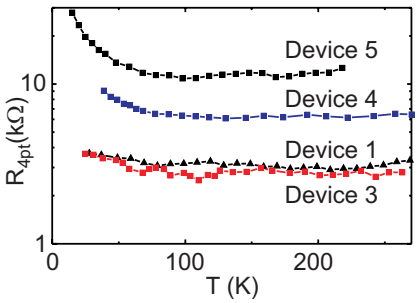

Figure 3.19: Temperature dependence of R_{4pt} measured at $V_g = 0$.

Very interestingly, when temperature $T \lesssim 10K$, R_{4pt} can even become significantly negative. The inset of Fig 3.20(a) shows that R_{4pt} is $-29M\Omega$ near zero V_g. Fig 3.20 shows that the absolute value of modulations of R_{4pt}/R_{2pt} can be as high as 0.6.

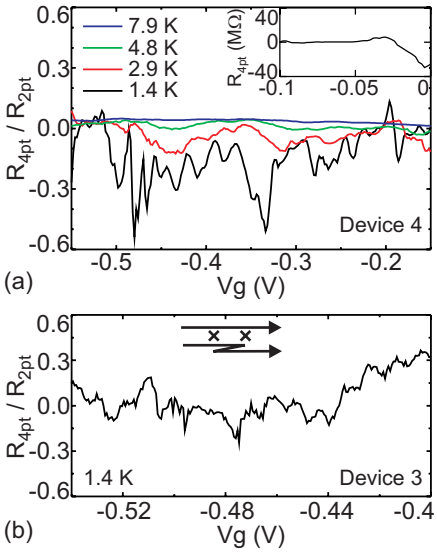

Figure 3.20: Negative four-terminal resistance at low temperature. (a,b) R_{4pt}/R_{2pt} as a function of V_g. Similar results are also obtained for Device 1. R_{2pt} measured between Au electrodes is checked to be lower than R_{2pt} between MWNT electrodes. The inset of (a) shows $R_{4pt}(V_g)$ at 1.4 K. R_{4pt} is close to 0 for V_g between -0.1 and -0.6 V (not shown here). The inset of (b) shows two scattering centers that generate interference.

We now seek for the possible origin of these negative R_{4pt}. It might come from some narrow diameter MWNTs or SWNT bundles [45, 46] as we can not ensure that we have an contacted an isolated SWNT using only **AFM** imaging. It might also come from the unexpected short-cut between electrodes by some very long tubes lying far away. In both case, the complicated current pathway will give rise to the observed negative R_{4pt}. However, such a classical effect should persist at higher T, which is not the case since R_{4pt} is always positive at $T \geq 10K$. Moreover, complicated current pathways give a finite non-local resistance at high temperature [46] (Fig 3.21 shows the setup for non-local resistance measurements). We do not observe this for these samples.

Finally, we attribute these negative R_{4pt} to quantum-interference effect [47, 48]. We have shown in the Sec.3.2 the numerical simulation based on Laudauer-Büttiker formula. Here we give a simple physical description to help understanding the nature

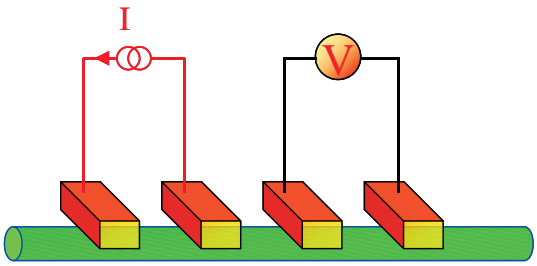

Figure 3.21: The set-up for non-local resistance measurements. If there is no complicated current pathways as in the case of an isolated SWNT, the voltage meter would read zero; while in the case of an MWNT or a bundle of tubes, inter-shell or inter-tube coupling will introduce a non-zero voltage difference between the two voltage probes.

of this negative resistance.

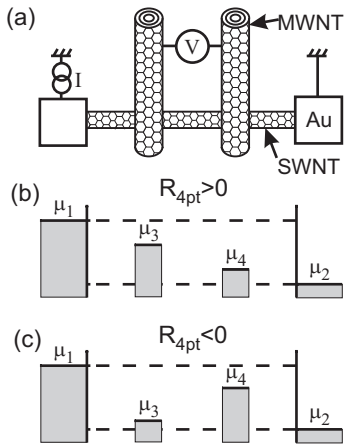

Figure 3.22: (a) Schematic of the four-terminal resistance measurement. (b) positive four-terminal resistance (c) negative four-terminal resistance.

As shown in Fig 3.22, once there is a positive electro-chemical potential difference between electrode 1 and 2, in normal case, the electro-chemical potential μ_3 will be larger than μ_4. However, at low temperature, the length of electron pathway in SWNT may become shorter than the electron phase-relaxation length, the electron transport is said to be coherent. One can no longer treat electrons in SWNT as classical particles. A quantum description is thus necessary. In some cases, due to the destructive interference arising from the backscattering at the tube ends or scattering on impurities, electrode 3 has smaller probability to see electrons from left electrode 1, its electro-chemical potential μ_3 will be closer to that of right electrode 2. We can therefore find $\mu_3 \leq \mu_4$ that gives rise to a negative R_{4pt}. Indeed, the potential

of electrode 3, μ_3, can take any value between μ_1 and μ_2. The same holds also for μ_4. Using $R_{2pt} = (\mu_1 - \mu_2)/I$ and $R_{4pt} = (\mu_3 - \mu_4)/I$, we can find that R_{4pt} can take any value between[34]

$$-R_{2pt} \leq R_{4pt} \leq R_{2pt} \tag{3.6.1}$$

This remarkable prediction of $R_{4pt} < 0$ is difficult to observe experimentally. Some works on ballistic one-dimensional conductors fabricated in semiconductors showed that R_{4pt} can become slightly negative [49, 50]. However, we believe that our data show for the first time significant negative R_{4pt} that approaches R_{2pt}.

As temperature increases, the phase coherence may be lost, and thermal phase averaging becomes also stronger. The electron transport is no longer coherent, therefore R_{4pt} becomes always positive when $T \geq 10K$.

Note that the SWNT can eventually enter the regime of strong localization (SL) [1]. This is expected for SWNTs when the phase-coherence length is longer than a few times l_e. This may be the case since l_e of Device 4 is 143 nm and that negative R_{4pt} suggests coherence at least over $L = 140$ nm. However, similar R_{4pt} measurements are obtained for devices that are less in the SL regime (Fig. 3.20(b), l_e =358 nm). Moreover, the two-terminal conductance modulation of Devices 3-5 is quite regular when V_g is swept (Fig. 3.17), in opposition to SL predictions [51]. Overall, those devices are not enough in the SL regime to give significant deviations from the diffusion regime. An explanation is that the tube length is too short.

So far, we have not taken into account the electron-electron interaction beyond the standard Coulomb Blockade approximation. These interactions are responsible for the the Luttinger liquid phase at intermediate temeperature[17]. Four-terminal resistance of a Luttinger Liquid has not been calculated yet. However, interference due to impurities in a Luttinger Liquid should also lead to negative R_{4pt}. In order to observe the manifestation of the Luttinger Liquid behavior, new experimental setup is needed. We will discuss it in more details in the next chapiter.

We at last give a conclusion for the last two sections. Our experiments show that the transition of R_{4pt} between the Ohm's law at 300 K and its deviation at low temperature due to quantum-interference effects. The deviation can become so dramatic that R_{4pt} is negative. Hence it is likely that inclusion of these quantum-mechanical interference effects will ultimately be required in the design of practical

multi-terminal intramolecular devices.

Chapter 4

Luttinger Liquid in Carbon Nanotubes

Landau's Fermi liquid theory has acquired great success in describing the conduction electrons in normal metals [52]. In these conventional metallic systems, the Coulomb interaction between electrons is strongly screened. One can use perturbation methods to treat interactions between electrons. There is a one-to-one mapping between the low energy excitations of noninteracting and interacting electrons systems. In the one dimensional case, the situation is very different. There is a strong coupling between electrons, even for arbitrarily weak interactions. The low energy excitations in one-dimensional electron systems are usually described by the Tomonaga-Luttinger Liquid theory (often refereed to as simply Luttinger-Liquid theory), which was firstly proposed by Tomonaga [2], then reformulated by Luttinger [3]. A brief introduction to properties of Luttinger-Liquid (LL) can be found in [53, 54, 55]. Interacting quantum wires like single-wall carbon nanotubes (SWNT) are considered as an ideal system to investigate the LL theory. Theoretical studies based on LL theory have shown the electron transport properties of a SWNT are qualitatively different from those predicted by a Fermi liquid [56, 57, 58]. Recent progress in the growth of high quality single-wall carbon nanotubes has reached the stage where it becomes possible to study one-dimensional interacting electron systems experimentally [10]. In this chapiter, I will present our experiments on crossed single-wall nanotubes, which strongly supports the Luttinger Liquid theory.

This chapter is organized as follows. In Sec. 4.1, I give a brief introduction to Fermi and Luttinger Liquids. In Sec. 4.2, I review the technique of bosonization to

describe one dimensional interacting electron systems. In Sec. 4.3, I discuss transport through a single barrier within a Luttinger Liquid for spinless electrons. It shows that the electron transport is completed prohibited at low temperature, for an arbitrarily weak barrier. In Sec. 4.4, I review the previous experiments on tunneling transport measurements in metallic single-wall carbon nanotubes. In particular I discuss the two different interpretations based on the Luttinger Liquid theory and on the environmental dynamical Coulomb Blockade theory, respectively. In Sec. 4.5, I present our transport measurements through crossed metallic single-wall carbon nanotubes. After excluding different explanations like heating effect, an interpretation based on the Luttinger Liquid model is presented. In conclusion, I present this experiment on carbon nanotubes as a new signature of the Luttinger Liquid state.

4.1 Fermi and Luttinger Liquids

4.1.1 Fermi Liquid

Landau Fermi Liquid is a well established theory describing the conduction electrons in conventional metallic systems. It is mainly based on the concept of "adiabatic continuity", stating that quantum numbers associated with eigenstates are more robust against perturbations than eigenstates themselves. Landau applied this idea to interacting electron systems, starting from the noninteracting Fermi gas, turning on the Coulomb interaction between electrons slowly, then observing how the eigenstates of the system evolve. He assumed that the electron wave vector $\mathbf{k}$ remains a good quantum number in the presence of interactions. As a consequence, one obtains a one-to-one correspondence between the eigenstates of the noninteracting and the interacting system (adiabatic continuity). The new eigenstate is called a *Landau quasi-particle* (See Fig 4.1). The quasi-particle wavefunction and its energy may differ from those of a free electron. However the eigenstate of the quasi-particle can still be labeled by its wave vector $\mathbf{k}$. The quasi-particle can be viewed as an electron added at position $\mathbf{k}$ in $\mathbf{k}$-space with $|\mathbf{k}| > k_f$ (or a hole added at position $\mathbf{k}$ in $\mathbf{k}$-space with $|\mathbf{k}| < k_f$), surrounded by a cloud of electron-hole pairs. Of course, these quasi-particles are not real particles. The added electron or hole can gradually lose energy by exciting electron-hole pairs from the Fermi sea. Therefore the lifetime of a quasi-particle is finite. One can find indeed that, for a quasi-particle of energy $\varepsilon_{\boldsymbol{k}}$,

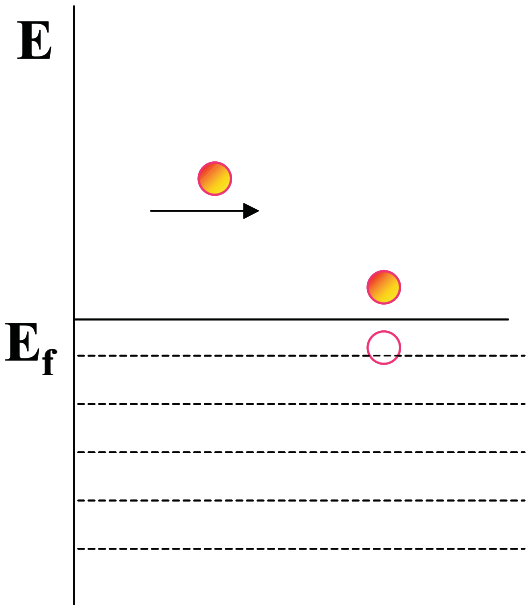

Figure 4.1: Landau quasi-particles in Fermi liquid. An added electron will excite electron-hole pairs from the Fermi sea below. This electron and the surrounding cloud made by electron-hole pair together makes a quasi-particle.

the lifetime τ of a quasi-particle is given by [55]:

$$\tau^{-1} \propto m^{*3} \frac{(\pi k_B T)^2 + \varepsilon_{\boldsymbol{k}}^2}{1 + e^{-\varepsilon_{\boldsymbol{k}}/k_B T}}, \tag{4.1.1}$$

Where m^* is the effective mass of the quasi-particle. In the low-temperature, low-energy limit, the lifetime of a quasi-particle tends to infinity. The quasi-particle becomes a nearly well-defined eigenstate of the interacting electron system. This is the regime where one can apply the Landau Fermi Liquid theory.

Since the electron wave vector $\mathbf{k}$ remains a good quantum number for interacting electron systems, the configurational entropy of the system is unchanged. This implies that the quasi-particle distribution function is unchanged with respect to that of the free electron case. The quasi-particles obey also the Fermi-Dirac statistics. The momentum distribution function $n_{\boldsymbol{k}}$ is given by

$$n_{\boldsymbol{k}} = \frac{1}{e^{\varepsilon_{\boldsymbol{k}}/k_B T} + 1} \tag{4.1.2}$$

It is important to note that $\varepsilon_{\boldsymbol{k}}$ is the full energy of the quasi-particle, which depends itself on the distribution function via the particle-particle interaction. The above equation needs to be solved self-consistently. It is well known that, for the non-interacting Fermi gas, at zero temperature, the momentum distribution function is

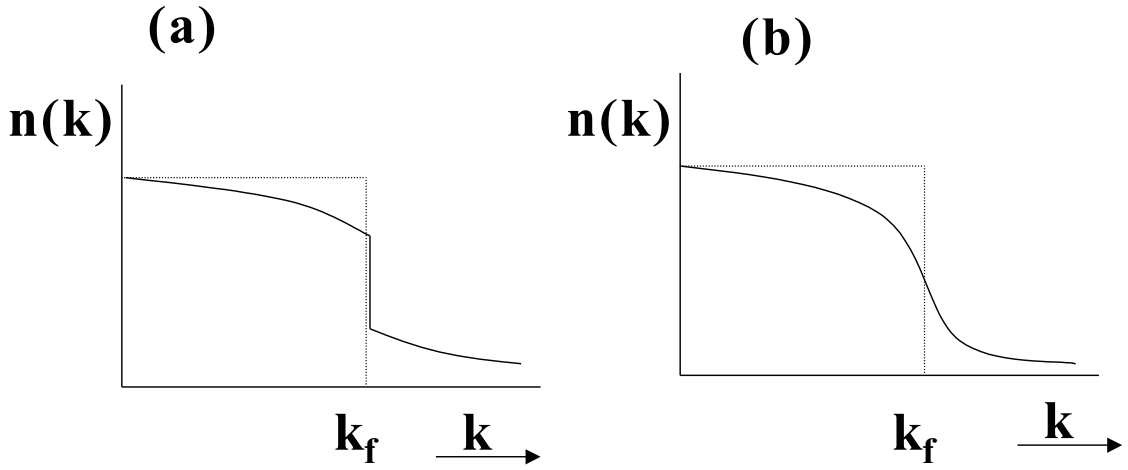

Figure 4.2: One particule momentum distribution function. (a) the finite discontinuity at the Fermi momentum k_F for a system of interacting fermions in more than one dimension. (b) the absence of discontinuity in an interacting system in one dimension.

discontinuous at the Fermi surface with a discontinuity equal to 1. For a Fermi liquid, this discontinuity persists (See Fig 4.2a), although reduced to a quasi-particle renormalization factor $z_{\boldsymbol{k}}$ [52] with

$$0 < z_{\boldsymbol{k}} < 1 \tag{4.1.3}$$

Finally in a Fermi liquid, various correlation functions decay at large distances as power laws. The exponents, which depend on the dimensionality, are independent of the interaction strength.

4.1.2 Luttinger Liquid

The Fermi Liquid theory beautifully describes the interacting electron systems in 2-D or 3-D. However when one goes into the 1-D case, the Coulomb interaction is less screened, and the perturbation methods used above become unreliable. The normal Fermi Liquid picture fails and a so-called Luttinger Liquid picture is employed.

The Luttinger Liquid has the following general properties. Firstly, it has no quasi-particle excitations; all the low energy excitations can be thought as an ensemble of particle-hole pairs (see Fig 4.3). In addition, all these excitations take the form of

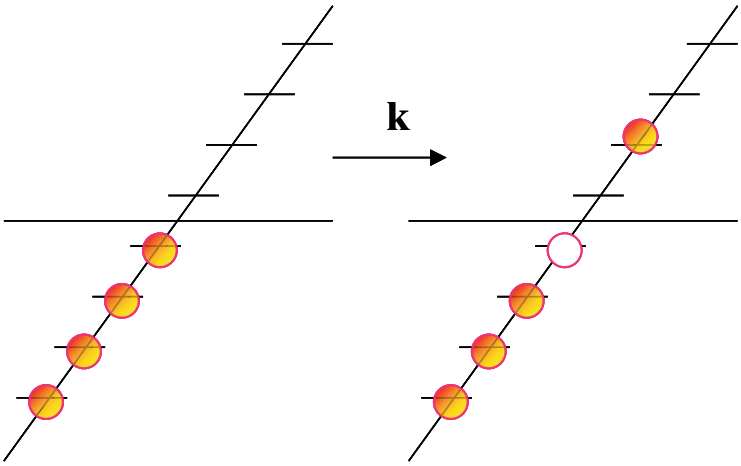

Figure 4.3: Particle-hole excitations from the ground state (Left) to an excited state (Right) in a Luttinger Liquid.

long wave length sound waves with a linear dispersion relation $\epsilon_q = v_F q$, where v_F is the Fermi velocity, and q is a momentum much smaller than Fermi momentum k_F.

Secondly there is no discontinuity in the momentum distribution function at the Fermi level. Instead it takes the following form [53]: (See Fig 4.2b).

$$n(k) = n(k_F) + Constant \times sign(k - k_F)\,|k - k_F|^{\beta} \tag{4.1.4}$$

Here β is a positive number depending on the interaction strength. For a non interacting system, $\beta = 0$, and one recovers the full discontinuity in the momentum distribution function at the Fermi level. At last, various correlation functions decay at long distance as power laws, with exponents depending now on the interaction strength. For example, the density-density correlation function decays algebraically at large distance as

$$\langle n(x)n(0)\rangle \approx \frac{\sin 2k_F x}{x^g} \tag{4.1.5}$$

where g is a Luttinger Liquid parameter, which describes the interaction strength [59]. For non-interacting systems ($g = 1$), one recovers the Fridel oscillations of a Fermi Liquid. For very strong Coulomb interactions, $g \to 0$, and a true long range order can be found. One may rely on the Wigner crystal picture to gain some insight on the nature of a Luttinger Liquid. In fact there cannot be a true long range order in these one-dimensional interacting systems, due to quantum fluctuations. Indeed long wave length phonon modes mentioned above will destroy the long range crystal order. It is therefore appropriate to describe the system as a Wigner Crystal plus

fluctuations. This description remains valid even for weak interactions as discussed below.

4.2 Introduction to the Bosonization Method

In this section I will present briefly the bosonization method to describe the low energy excitations in Luttinger Liquid. The complete exposition of this method can be found in the literature [53, 55, 61]. Here the spin of electron is ignored for simplicity.

Electron is of course a fermion. The low energy excitations of electrons can be described by a fermionic field. However, as we stated in the first section, in one-dimensional case, all low-energy excitations can be considered as electron-hole pairs. One can therefore use bosonic fields to describe them. This technique is called bosonization. We introduce here some important results, details of the calculation are presented in the appendix.

In order to understand the method, one can start with fermions on a circle of Length L with periodic boundary condition. One may introduce the second quantized Fermi field of right- and left-moving components as the following:

$$\begin{aligned} \psi_\nu(x) &= \frac{1}{\sqrt{L}} \sum_{k=-\infty}^{\infty} c_{\nu,k}\, e^{i\nu kx} \\ k &= \frac{2\pi}{L} n_k \end{aligned} \tag{4.2.1}$$

with ν=$\pm$1, referring to right and left-moving components,denoted as $\boldsymbol{R}$ and $\boldsymbol{L}$ respectivly, where $n_k = 0, \pm 1, \pm 2....$ Fermion operators $c_{\nu,k}$ respect anticommutation relations.

The normal ordered fermion number operator $\hat{N}_\nu$ can be defined in the following way:

$$\begin{aligned} \hat{N}_\nu &= \sum_{k=-\infty}^{\infty} : c^\dagger_{\nu,k} c_{\nu,k} : \\ &= \sum_{k>0} c^\dagger_{\nu,k} c_{\nu,k} - \sum_{k\leq 0} c_{\nu,k} c^\dagger_{\nu,k} \end{aligned} \tag{4.2.2}$$

The next step is to define bosonic operators:

$$\begin{aligned} b^{\dagger}_{\nu,q} &= \frac{1}{\sqrt{n_q}} \sum_{k=-\infty}^{\infty} c^{\dagger}_{\nu,k+q} c_{\nu,k} \\ b_{\nu,q} &= \frac{1}{\sqrt{n_q}} \sum_{k=-\infty}^{\infty} c^{\dagger}_{\nu,k-q} c_{\nu,k} \\ q &= \frac{2\pi}{L} n_q, n_q = 1, 2, 3... \end{aligned} \tag{4.2.3}$$

These bosonic operators describe an ensemble of electron-hole pairs.

With these operators one can now define the chiral creation and annihilation operators:

$$\begin{aligned} \chi_{\nu}(x) &= \frac{i\nu}{2\sqrt{\pi}} \sum_{q>0} \frac{1}{\sqrt{n_q}} b_{\nu,q} e^{i\nu qx - \alpha q/2} \\ \chi^{\dagger}_{\nu}(x) &= -\frac{i\nu}{2\sqrt{\pi}} \sum_{q>0} \frac{1}{\sqrt{n_q}} b^{\dagger}_{\nu,q} e^{-i\nu qx - \alpha q/2} \end{aligned} \tag{4.2.4}$$

One can then define the right- and left-moving bosonic fields $\phi_{\nu}(x)$ as:

$$\phi_{\nu}(x) = \chi_{\nu}(x) + \chi^{\dagger}_{\nu}(x) - \frac{\sqrt{\pi}x}{L} \hat{N}_{\nu} \tag{4.2.5}$$

where $\nu = \pm 1$ corresponds to right- and left-moving fields.

Finally two phonon-like displacement fields which are dual to each other can be found:

$$\begin{aligned} \phi(x) &= \phi_R(x) + \phi_L(x) \\ \theta(x) &= -\phi_R(x) + \phi_L(x) \end{aligned} \tag{4.2.6}$$

As we will see below, these phonon-like fields will be used to describe the low-energy excitations in the Luttinger Liquid after adding the interaction. One may imagine that these fields describe the displacement of a particle from its original lattice position, the system is just like a Wigner Crystal plus fluctuations.

Once the phonon-like displacement fields have been defined, one can then define the chiral fermion density operators:

$$\begin{aligned} \rho_{\nu}(x) &=: \psi^{\dagger}_{\nu}(x) \psi_{\nu}(x) : \\ &= \frac{1}{L} \sum_{q>0} \sqrt{n_q} (b_{\nu,q} e^{iqx} + b^{\dagger}_{\nu,q} e^{-iqx}) \\ &+ \frac{1}{L} \sum_{k} : c^{\dagger}_{\nu,k} c_{v,k} := -\frac{1}{\sqrt{\pi}} \frac{\partial \phi_{\nu}}{\partial x} \end{aligned} \tag{4.2.7}$$

Therefore the total density and current operator are given by:

$$\begin{aligned}\rho(x) &= \rho_R(x) + \rho_L(x) = -\frac{1}{\sqrt{\pi}}\partial_x\phi \\ j(x) &= v_F(\rho_R(x) - \rho_L(x)) = \frac{v_F}{\sqrt{\pi}}\partial_x\theta\end{aligned} \tag{4.2.8}$$

One needs to precise that the density operator $\rho(x)$ here measures only the fluctuation in the electron density. We have removed in the definition of $\rho(x)$ the mean electron density N_0/L.

If one introduces now a linear dispersion relation $\epsilon_{\nu,k} = v_F k$, the Hamiltonian of non-interacting system can be written in bosonic language as:

$$\begin{aligned}H_0 &= v_F \sum_{q>0} q(b^\dagger_{R,q} b_{R,q} + b^\dagger_{L,q} b_{L,q}) + \frac{\pi v_F}{L}(\hat{N}_R^2 + \hat{N}_L^2) \\ &= \frac{v_F}{2}\int_0^L dx[(\partial_x\phi)^2 + (\partial_x\theta)^2]\end{aligned} \tag{4.2.9}$$

Since the Hamiltonian of the non-interacting system has been found, one can now add in the following interaction term :

$$V = \frac{1}{2}\int_0^L dx[2g_2\rho_R(x)\rho_L(x) + g_4(\rho_R(x)^2 + \rho_L^2(x))] \tag{4.2.10}$$

where the g_2 term corresponds to a two-particle interaction involving different chiralities; and the g_4 term corresponds to an interaction between two particles with the same chirality.

Once interaction terms have been taken into consideration, one can now write the total Hamiltonian $H = H_0 + V$. As we will see, it takes a very simple form in the bosonic language:

$$\begin{aligned}H =& \sum_{q>0} q[v_F(b^\dagger_{R,q} b_{R,q} + b^\dagger_{L,q} b_{L,q}) + \frac{g_2}{2\pi}(b^\dagger_{R,q} b^\dagger_{L,q} + b_{R,q} b_{L,q}) \\ &+ \frac{g_4}{2\pi}(b^\dagger R, q b_{R,q} + b^\dagger_{L,q} b_{L,q})] + \frac{\pi v_F}{L}(\hat{N}_R^2 + \hat{N}_L^2) \\ &+ \frac{g_2}{L}\hat{N}_R\hat{N}_L + \frac{g_4}{2L}(\hat{N}_R^2 + \hat{N}_L^2)\end{aligned} \tag{4.2.11}$$

One can easily find that the effect of g_4 term is to renormalize the Fermi velocity to $v_F + \frac{g_4}{2\pi}$. And the g_2 term can be diagonalized by a Bogoliubov transformation. One can define the following two parameters:

$$\begin{aligned}v =& [(v_F + \frac{g_4}{2\pi} - \frac{g_2}{2\pi})(v_F + \frac{g_4}{2\pi} + \frac{g_2}{2\pi})]^{1/2} \\ g =& [(v_F + \frac{g_4}{2\pi} - \frac{g_2}{2\pi})/(v_F + \frac{g_4}{2\pi} + \frac{g_2}{2\pi})]^{1/2}\end{aligned} \tag{4.2.12}$$

In the conventional case, one can take $g_2 = g_4 > 0$ (repulsive interaction), v is therefore the plasmon velocity which is larger than Fermi velocity because the repulsive interaction reduces the compressibility of the electron gas. And g is the parameter that we mentioned above, which describes the interaction strength between electrons, $g < 1$ for repulsive interaction.

The total Hamiltonian can now be rewritten in the quadratic expression:

$$\begin{aligned} H &= \frac{v}{2}\int_0^L dx[g(\partial_x\theta)^2 + \frac{1}{g}(\partial_x\phi)^2] \\ &= \frac{v}{2}\int_0^L dx[(\partial_x\tilde{\theta})^2 + (\partial_x\tilde{\phi})^2] \end{aligned} \tag{4.2.13}$$

The old and new bosonic fields are related as:

$$\phi = \sqrt{g}\tilde{\phi}\ ,\ \theta = \frac{1}{\sqrt{g}}\tilde{\theta} \tag{4.2.14}$$

Above we studied a model system with the bosonization method. In the calculus, we supposed an infinite number of right- and left-moving modes with the momentum going from $-\infty$ to ∞; and a linear dissipation relation for all the modes. These assumptions are generally not true for one dimensional interacting systems. However, as we are only interested in low-energy excitations in these systems, we will focus on those modes lying close to the Fermi points $\pm k_F$. Around these points, one can approximate the dispersion relation by a linear one, and Fermi velocity can be defined as $v_F = (d\epsilon_k/dk)_{k=k_F}$. We restrict our attention to the right-moving modes with momenta lying between $k_F - \Lambda$ and $k_F + \Lambda$, and the left-moving modes with momenta lying between $-k_F - \Lambda$ and $-k_F + \Lambda$, where Λ is much less than k_F. Then the second quantized Fermi field can be written as:

$$\psi(x,t) = \psi_R(x,t)e^{ik_Fx} + \psi_L(x,t)e^{-ik_Fx} \tag{4.2.15}$$

One can take an example to see the influence of this change. Let's calculate the density operator ρ that is defined as the form below:

$$\rho =: \psi^\dagger\psi :=: \psi_R^\dagger\psi_R + \psi_L^\dagger\psi_L + e^{-i2k_Fx}\psi_R^\dagger\psi_L + e^{i2k_Fx}\psi_L^\dagger\psi_R : \tag{4.2.16}$$

By transforming fermionic fields to bosonic fields, we have

$$\begin{aligned} \psi_R(x,t) &= \frac{1}{\sqrt{2\pi\alpha}}\eta_R e^{-i2\sqrt{\pi}\phi_R} \\ \psi_L(x,t) &= \frac{1}{\sqrt{2\pi\alpha}}\eta_L e^{i2\sqrt{\pi}\phi_L} \end{aligned} \tag{4.2.17}$$

where the unitary Klein operator $\eta_\nu(\eta_\nu^\dagger)$ are defined to be the operator that raise (lower) the momentum label k of all the occupied states for right- or left-moving particles. Therefore the density operator ρ takes the form:

$$\begin{aligned}\rho &= -\frac{1}{\sqrt{\pi}}\partial_x\phi + \frac{1}{2\pi\alpha}[\eta_R^\dagger\eta_L e^{i(2\sqrt{\pi}\phi-2k_Fx)} + \eta_L^\dagger\eta_R e^{-i(2\sqrt{\pi}\phi-2k_Fx)}] \\ &= -\sqrt{\frac{g}{\pi}}\partial_x\tilde{\phi} + \frac{1}{2\pi\alpha}[ie^{i(2\sqrt{\pi g}\tilde{\phi}-2k_Fx)} - ie^{-i(2\sqrt{\pi g}\tilde{\phi}-2k_Fx)}] \\ &= -\sqrt{\frac{g}{\pi}}\partial_x\tilde{\phi} - \frac{1}{\pi\alpha}\sin(\sqrt{4\pi g}\tilde{\phi} - 2k_Fx)\end{aligned} \tag{4.2.18}$$

Where $\alpha = 1/k_F$ is the short distance cut-off (lattice spacing). One can see the second term containing $2k_Fx$ oscillates quickly on the scale k_F^{-1}, it comes from the mixing right and left movers; and the first slow term is due to the sum of right- and left-moving densities.

4.3 Transport Through a Barrier in a Luttinger Liquid

We have presented in the previous section a simple introduction to Bosonization method used to describe the Luttinger-Liquid. In this section we will focus on some general properties of the electron transport through a barrier in a Luttinger Liquid [59, 60].

4.3.1 Weak Barrier Limit

We first consider the electron transport through a weak barrier. In this limit the barrier can be treated as a small perturbation on an ideal Luttinger Liquid. For reason of simplicity, one can choose $V(x) = \lambda\delta(x)$ to describe the barrier, with $\lambda \ll \epsilon_F/k_F$ as a small perturbation. Therefore the action of the perturbation takes the form

$$S_{int} = \int dx \int d\tau V(x)\psi^\dagger(x)\psi(x) \tag{4.3.1}$$

As seen in the previous section

$$\psi^\dagger(x)\psi(x) = -\frac{1}{\sqrt{\pi}}\partial_x\phi(x) - \frac{1}{\pi\alpha}\sin(2\sqrt{\pi}\phi(x) - 2k_Fx) \tag{4.3.2}$$

The first term, which is related to electron scattering between modes of same chirality, will not affect the conductance. Therefore the full action of the system is

$$\begin{aligned} S &= S_0 + S_{int} \\ &= \frac{1}{2g}\int d\tau \int dx[\frac{1}{v}(\partial_\tau \phi)^2 + v(\partial_x \phi)^2] - \frac{\lambda}{\pi\alpha}\int d\tau \sin\left(2\sqrt{\pi}\phi(0)\right) \end{aligned} \tag{4.3.3}$$

where S_0 is the action of the pure LL system without the barrier.

As the perturbation term is fixed at $x = 0$, one can first integrate out the variable away from the origin and write down the action purely in terms of $\phi(x = 0, \tau)$. One then takes a Fourier transformation, using $\phi(\omega) = \int d\tau \phi(x = 0, \tau) e^{i\omega\tau}$, the new action takes the following form

$$S = \frac{1}{g}\int \frac{d\omega}{2\pi} |\omega| \, \phi^2(\omega) - \frac{\lambda}{\pi\alpha}\int \frac{d\omega}{2\pi} \sin 2\sqrt{\pi}\phi(\omega) \tag{4.3.4}$$

One can now turn to the standard renormalization group (**RG**) method to treat the problem.

The basic idea of the **RG** method is the following [53, 55, 61]:

I. one starts form a cutoff-dependent action $S(\Omega)$, integrates all the frequency modes lying between $|\Omega|$ and $|\Omega|/s$, where $s = e^{dl}$ is a factor larger than unity. This gives rises to a new action $S'(\Omega' = \Omega/s)$.

II. One then rescales the time coordinates $\omega \to s\omega$, so that the new action looks exactly like the old one. This new action is effective at a larger scale $\propto e^{dl}$. Since one has integrated our high frequency modes, the coupling strength will change.

III. One chooses the value of s which is infinitesimally close to unity: $s = 1 + \epsilon$, and repeats the processes to integrate out high frequency modes. This will give rise to the flow equation of the coupling strength.

One can then find the flow equation

$$\frac{d\lambda}{dl} = (1 - g)\lambda \tag{4.3.5}$$

The flow equation is now easy to analyze. For repulsive interaction, $g < 1$, λ is relevant as the scaling parameter e^l increases. This means that, when one goes into lower and lower energy/temperature, the effective strength of the barrier increases. One will then go from the weak barrier limit into the strong barrier limit. At low temperature or low bias, the electron transport will be completely prohibited, irrespective of the

barrier strength. Further calculation shows that the electrical conductance G satisfies :

$$(G - g\frac{e^2}{h}) \propto (T, V)^{2g-2} \tag{4.3.6}$$

where g is the parameter for the interaction strength, T is the temperature and V is the applied voltage [62]. One need to take caution here: a conductance that is equal to ge^2/h can be extracted from the equation above in case that no barrier lies in the LL; however, this conductance is not the usually measured two-terminal conductance. Indeed, one does not take into consideration the effect of electrode, which makes the conductance independent of the interaction strength [63].

4.3.2 Strong Barrier Limit

Above we have briefly discussed the electron transport through a weak barrier in a Luttinger Liquide, now we will turn to the strong barrier limit. This barrier separates the system into two semi-infinite Luttinger Liquid wires connected by a very weak hopping matrix element t at $x = 0$. One can define $\psi_1(\psi_2)$ is the electron operator in the left (right) semi-infinite Luttinger Liquid, the tunneling Hamiltonian can be written as

$$H_{hop} = -t[\psi_1^\dagger(x = 0)\psi_2(x = 0) + h.c] \tag{4.3.7}$$

One can also investigate the problem with renormalization group method. One may find the above hopping matrix element t is indeed *irrelevant*.

The Euclidean time action of the two semi-infinite Luttinger Liquid is

$$S_0 = \frac{1}{2}\int d\tau \int dx[\frac{1}{gv}(\partial_\tau\phi_i)^2 + \frac{v}{g}(\partial_x\phi_i)^2] \tag{4.3.8}$$

where ϕ_i corresponds to left/right semi-infinite Luttinger Liquid. And the action correspond to electron hopping between two semi-infinite Luttinger Liquid can be written as

$$\begin{aligned} S_{hop} = &- t\int d\tau[\eta_{L,1}^\dagger\eta_{R,2}e^{-i2\sqrt{\pi}(\phi_{L,1}+\phi_{R,2})} + \eta_{L,2}^\dagger\eta_{R,1}e^{-i2\sqrt{\pi}(\phi_{L,2}+\phi_{R,1})} \\ &+ \eta_{R,1}^\dagger\eta_{L,2}e^{i2\sqrt{\pi}(\phi_{L,2}+\phi_{R,1})} + \eta_{R,2}^\dagger\eta_{L,1}e^{i2\sqrt{\pi}(\phi_{L,1}+\phi_{R,2})}] \end{aligned} \tag{4.3.9}$$

As there is a barrier at $x = 0$, that implies the local electron density at $x = 0$ for left- and right- semi-infinite Luttinger Liquid is zero. One have

$$2\sqrt{\pi}\phi_1 = 2\sqrt{\pi}\phi_2 = \pi/2 \tag{4.3.10}$$

Using the definitions made in the Sec. 4.2

$$\begin{aligned}\phi(0) &= \phi_R(0) + \phi_L(0) \\ \theta(0) &= -\phi_R(0) + \phi_L(0)\end{aligned} \tag{4.3.11}$$

one can get the simplified expression of the hopping action

$$S_{hop} = 4t \int d\tau \cos\left[\sqrt{\pi}(\theta_1 - \theta_2)\right] \tag{4.3.12}$$

Using the standard renormalization group method, one finds the following flow equation for hopping matrix element t

$$\frac{dt}{dl} = (1 - 1/g)t \tag{4.3.13}$$

For repulsive interaction, $g < 1$, therefore the hopping matrix element t is irrelevant. It means that, as the scaling length ae^l increases, one goes into low energy/long wavelength limit, and t flows to zero. The transport is forbidden. The explicit expression of the electrical conductance can be found in Ref.[62].

$$G(V,T) \propto t^2 \left|V,T\right|^{(2/g)-2} \tag{4.3.14}$$

From the above equation, one can find that for repulsive interaction ($g < 1$), at low temperature/bias limit, the electron transport will be completed prohibited. This is the so-called **zero bias anomaly** (**ZBA**).

In general, the electron conduction in a Luttinger Liquid with a single barrier is prohibited at low temperature/bias. Indeed, we may interpret the insulating behavior of a Luttinger liquid with a single barrier in the following way. The Luttinger liquid has a tendency towards Charge Density Wave order (**CDW**), in particular for $g \leq 0.2$ in carbon nanotubes [57]. These **CDW** correlations are long range enough for a single barrier to pin the incident the low-energy charge density wave.

4.4 Tunneling into a Luttinger Liquid

As stated in the previous sections, theoretical work has shown that one-dimensional interacting electron systems have very specific properties. It is very interesting to probe experimentally these intriguing properties to verify the theoretical predictions. The disorder-free metallic single-wall carbon nanotubes (SWNTs) have an elastic

mean free path which can be as large as a few micrometers at low temperature. Furthermore metallic SWNTs have only two transport modes at the Fermi level, which greatly simplifies the analysis. Therefore the metallic SWNT is often regarded as a model system for the one-dimensional physics [26, 64, 16].

Pioneering work has been done by Bockrath et al [15], who succeeded in electrically connecting single-wall carbon nanotubes. Using standard lithography techniques, they attached gold electrodes at both ends of SWNT ropes. Preliminary measurements have shown relatively bad contacts between the gold electrodes and carbon nanotubes, forming tunnel junctions. Further investigations have shown that both the conductance and the differential conductance scale as power laws to zero when decreasing the temperature or the bias.

4.4.1 Interpretation Using Luttinger Liquid Theory

The above experimental findings were first explained in the frame of the Luttinger Liquid theory as follows. For simplicity, the case of a single barrier at the inferface between the metal electrode and the nanotube was considered in the zero temperature limit. From the standard tunneling theory, the following expression for the current through the junction was obtained:

$$I = \frac{1}{eR_T}\int_0^{eV} dE\rho_t(E) \tag{4.4.1}$$

where R_T is the tunnel resistance, ρ_t is the tunneling density of states of the carbon nanotube [65].

As a result the differential conductance dI/dV is found to be proportional to $\rho_t(E)$:

$$dI/dV \propto \rho_t(E), \tag{4.4.2}$$

and one recovers the classical result that the conductance is proportional to the density of states.

The energy dependence $\rho_t(E)$ can be calculated from the Fourrier transform of the electron Green's function $\langle\psi(x,t)\psi^\dagger(x,0)\rangle$ [66]:

$$\rho(E) = \frac{1}{\pi}Re\int_0^\infty dte^{iEt}\langle\psi(x,t)\psi^\dagger(x,0)\rangle \tag{4.4.3}$$

Detailed calculation shows that $\rho_t(E)$ vanishes as a power law in the energy of the tunneling electron:

$$\rho_t(E) \propto E^{\alpha_L} \tag{4.4.4}$$

The exponent α_L depends on the electron-electron interaction strength, and also on the geometry of the tunnel junction. For tunneling into the end of a long nanotube or into the middle of a tube, one expects to find [67]:

$$\begin{aligned} \alpha_{end} &= (g^{-1} - 1)/4 \\ \alpha_{bulk} &= (g + g^{-1} - 2)/8 \end{aligned} \tag{4.4.5}$$

The observed power-law behavior can be understood in the following manner. In the presence of Coulomb interactions ($g \leq 1$), the tunneling density of states vanishes as $E \rightarrow 0$ because the quasi-particle is not a proper excitation of the Luttinger Liquid. To create an additional electron in the Luttinger liquid, the wavefunctions of all electrons participating in the collective excitations need to be changed, this gives rise to the so-called orthogonality catastrophe. This process is very difficult and the tunneling is suppressed.

4.4.2 Interpretation Using Dynamic Coulomb Blockade Theory

This explanation has been the current interpretation for the non-linearities observed in the Bockrath experiment. However, this experiment can still be explained in an alternative way. Indeed, further theoretical studies have shown that another model, the so-called environmental dynamical Coulomb blockade theory [68, 69], can also explain the observed power-law behavior.

This theory regards both the gold electrode and the carbon nanotube as conventional Fermi Liquid materials. In addition, the theory takes into account the fluctuations in the electric circuit (the Johnson-Nyquist noise). Due to the exchange of energy between the electron and the environmental modes, the delta-function in the usual expression of the tunneling current must be replaced by a function $P(E)$, which gives the probability that a tunneling electron creates an excitation with an energy E in the electromagnetic environment [68]. The strict energy conservation prescribed by the delta function is therefore lifted. The new expression of the tunneling current

can be written as

$$I = \frac{1}{eR_T}\int_{-\infty}^{+\infty} dE \int_{-\infty}^{+\infty} dE' \{f(E)[1-f(E')]P(E+eV-E') \\ -[1-f(E)]f(E')P(E'-E-eV)\} \tag{4.4.6}$$

where $f(E)$ is the Fermi-Dirac function, and R_T is the junction resistance . One can determine the function $P(E)$ from the Fourier transform of the phase correlator:

$$P(E) = \frac{1}{2\pi\hbar}\int_{-\infty}^{\infty} dt e^{iEt/\hbar}\langle e^{i\hat{\phi}(t)}e^{-i\hat{\phi}(0)}\rangle \tag{4.4.7}$$

Supposing the temperature is zero, the above equation can be simplified as:

$$I = \frac{1}{eR_T}\int_{-\infty}^{+\infty} dE E P(eV-E) \tag{4.4.8}$$

At zero temperature the function $P(E)$ determines the second derivative of the I-V curve:

$$\frac{d^2I}{dV^2} = \frac{e}{R_T}P(eV) \tag{4.4.9}$$

To determine the explicit expression of the function $P(E)$, one can use the phase-correlation theory [68, 70]. The essence of the theory is to treat the junction and its environment as a single quantum system. Indeed the phase difference across the junction is related to the voltage V across the junction by a Josephson-like relation:

$$\hbar\frac{d\phi}{dt} = eV \tag{4.4.10}$$

One can write the phase correlator $\langle e^{i\hat{\phi}(t)}e^{i\hat{\phi}(0)}\rangle$ in the form:

$$\langle e^{i\hat{\phi}(t)}e^{i\hat{\phi}(0)}\rangle = e^{J(t)} \\ J(t) \approx \langle[\hat{\phi}(t)-\hat{\phi}(0)]\hat{\phi}(0)\rangle = 2\int_0^{\infty}\frac{d\omega}{\omega}\frac{ReZ(\omega)}{R_K}(e^{-i\omega t}-1) \tag{4.4.11}$$

This relation is a direct consequence of the fluctuation-dissipation theorem, here $R_K = \frac{\hbar}{e^2} = 26k\Omega$ and $Z(\omega)$ is the impedance of the environment.

In the case of low environmental impedance ($ReZ(\omega)/R_K \to 0$), one can show that the function $P(E)$ reduces to the delta-function $\delta(E)$. One recovers the normal tunneling $I-V$ relation. The Coulomb blockade is suppressed because the weak environmental impedance will not delay the dissipation of the tunneling electron. In the opposite high-impedance limit ($ReZ(\omega)/R_K \to \infty$), $P(E)$ becomes $\delta(E-E_c)$. $E_c = e^2/2C_T$ is the charging energy of the junction, where C_T is the capacity of

the junction . This is the manifestation of dynamical Coulomb blockade. For finite $ReZ(\omega)/R_K$, when E is much smaller than charging energy, $P(E)$ is a power-law function:

$$P(E) \propto \frac{\tau}{\hbar}\left[\frac{E\tau}{\hbar}\right]^{(\alpha_E-1)} \tag{4.4.12}$$

where

$$\alpha_E = \frac{2ReZ(0)}{R_K} \tag{4.4.13}$$

and $\tau = Re(Z(0))C_T$ is the relaxation time in the electric circuit.

Because the function $P(E)$ determines the second derivative of the I-V curve, the exponent of the differential conductance dI/dV will be α_E. Therefore the environmental dynamical Coulomb Blockade theory gives an alternative explanation for the observed power-law behaviors.

We have seen that both the Luttinger Liquid theory and the dynamic Coulomb Blockade theory can give an interpretation to the observed power-law behavior. In the Luttinger Liquid description, the power-law behavior of differential conductance originates from the energy dependence of **DOS** $\rho(E)$, which is defined as a Fourier transformation of the averaged operator product $\langle\hat{\psi}(x,t)\hat{\psi}^{\dagger}(x,0)\rangle$. In the environmental dynamical Coulomb Blockade description, the power-law behavior comes from the energy dependence of the probability function $P(E)$, which is a Fourier transformation of the correlator $\langle e^{i\hat{\phi}(t)}e^{-i\hat{\phi}(0)}\rangle$. Since both operators $e^{-i\hat{\phi}(t)}$ and $\hat{\psi}(x.t)$ are electron creation operators, similar energy dependence for $\rho(E)$ and $P(E)$ should be expected. In addition, recent theoretical investigation also shows the coupling to the Ohmic environment can induce effective repulsive interactions between electrons [71]. The difference between two models is very subtle.

There were efforts to distinguish both models by comparing the absolute value of the exponents. However, theoretical investigations show that in the case of a multichannel one dimensional conductor, the difference between exponent α_L and α_E is equal to $1/N$, where N is number of transport channels [65]. For a metallic single-wall carbon nanotube, there are four conduction channels (2 from spin and 2 from bands crossing the Fermi level), the difference between α_L and α_E is only 0.25. Unfortunately, the experimental precision in Ref. [15] was not high enough to find which model is the correct one. Further experimental investigations need to be done to provide more evidence for the Luttinger Liquid description of electron states in

metallic single wall carbon nanotubes.

4.5 Electron Transport in Crossed Metallic Single Wall Carbon Nanotubes

In Section 3.4, we have reviewed the tunneling measurement on the ropes of single-wall carbon nanotubes. Some similar tunneling and resonant tunneling measurements have also been made on SWNTs. [15, 73, 74, 75] A pronounced suppression in the tunneling density of states, also called zero-bias anomaly (**ZBA**), has been observed in these measurements. It is again considered as a direct evidence for Luttinger Liquid behavior in carbon nanotubes. However, as we have shown before, two-point transport measurements cannot give enough evidence for Luttinger Liquid behavior in carbon nanotubes. Although the measured power-law **ZBA** can be consistently explained by the Luttinger Liquid theory, it is difficult to rule out alternative explanations based on environmental dynamical Coulomb Blockade theory. Furthermore, a very similar **ZBA** has been experimentally observed in multi- wall carbon nanotubes [76, 77, 78] eventhough such systems are known to be disordered multichannel wires [79, 80]. It is therefore important to find new experimental evidence beyond the **ZBA** for tunneling into single wall carbon nanotubes [15, 73, 74]. Following the proposal made by theorists [81, 82], we have fabricated crossed metallic single-wall carbon nanotube junctions. The electron transport measurements on such structures give some new Luttinger Liquid signatures in metallic single-wall carbon nanotubes.

Although crossed nanotube junctions have been investigated before by other groups [36, 83, 84], the richness of configurations allowed in this crossed nanotube experiments was not fully exploited; instead measurements focused on the mere junction resistance. In our experiments, we focus on the device made by two crossed metallic SWNTs. The conductance is measured in a broad temperature range (20-100K), and the device is fully characterized using all possible two-point and four-point measurements so as to extract the relevant contact and junction transmissions.

We find a decrease of the single-tube conductance as the temperature or the bias is reduced, in a way very similar to **ZBA** reported in the above mentioned tunneling measurements. A very interesting new feature is that the **ZBA** can be suppressed as we increase the current in the second tube. We will show below the relationship

between these findings and the Luttinger Liquid picture of metallic SWNTs. We can give here a simple physical picture to get some intuition. In general, the local electrostatic interaction at the crossing point creates a barrier in each tube. In a picture where the Luttinger Liquid can be viewed as a charge density wave, the latter is pinned by the barrier, explaining the power-law vanishing current. When the current is fed through the second tube, electrons in the first tube will get additional energy to overcome the barrier, thus enhancing the conductance of the first tube. We will give explicit calculation based on Luttinger Liquid theory at the end of this section, which reproduces well the experimental results.

4.5.1 Sample fabrication

The devices were fabricated with the standard nano-fabrication technics. The laser-ablation grown SWNTs are dispersed from a suspension in dichloroethane onto an oxidized Silicon wafer. Atomic-force microscope (**AFM**) is then used to locate crossed SWNTs with an apparent diameter of $\approx 1nm$. It is difficult to distinguish with **AFM** individual SWNT from small-diameter bundle of SWNTs or MWNTs, and we select the thinnest tubes in the **AFM** images, which are assumed to be individual SWNTs. Next, C_r/A_u electrodes are attached to the selected tubes using electron-beam lithography together with thermal evaporation techniques. An example of device is shown in Fig 4.4. The separation L between the crossing point and the electrodes is $\approx 300nm$. This value is taken as it is smaller than the elastic mean free path ($L_e \approx 1\mu m$ in pure SWNTs), and larger than the thermal length $L_T = \hbar v_F/KT$ at our lowest temperature. For shorter L, undesired finite-size effects may come into play, which would involve the three dimensional physics of the leads. For much longer L, the probabilities is enhanced to find more disorder centers along the SWNTs that complicate the analysis.

The yield of the sample fabrication has been very low. Out of the 60 fabricated samples, we have not managed to obtain the ideal device with two metallic nanotubes and four highly transparent contacts to prevent spurious Coulomb Blockade effects. Instead, we have found four almost perfect samples, with only one highly resistive contact. Measurements have been carried out on these four devices, and give similar results. Below we describe a representative set of measurements performed on one of these devices.

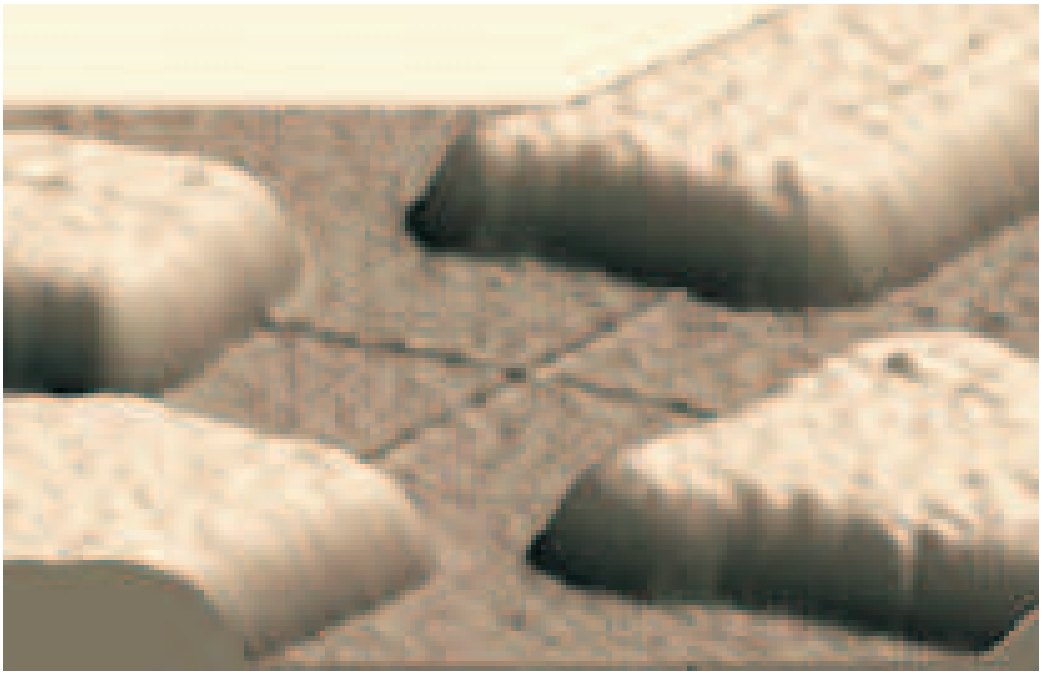

Figure 4.4: AFM image of a device made of two crossed SWNTs. The electrode height is 45 nm.

4.5.2 Preliminary Sample Characterization

At high temperature (T=220K), where Luttinger Liquid effects are negligible, the linear resistances of the two SWNTs (henceforth called A and B) are measured with $R_A = 19k\Omega$ and $R_B = 524k\Omega$, corresponding to contact transmission of 0.6 and 0.01 respectively. The four-point resistance of the tube-tube junction at the crossing point is $R_x = 277k\Omega$ (transmission 0.02). As mentioned above, one of the four contact (B1) is bad, it is identified by comparing different two-point resistances. Note that the two-point measurements are achieved with the other electrodes left floating. When the temperature is decreased, the large contact resistance induces Coulomb blockade (**CB**) oscillations in tube B as a function of the back gate voltage V_g. In the following measurements, V_g is fixed at a broad **CB** peak so as to maximize the current in the tube B.

The device is further characterized by measuring the Luttinger Liquid interaction parameter g from the tunneling density of states [72, 67], using the tube-tube tunnel junction polarized as shown in Fig 4.5. While measuring the current I through the tube-tube junction and the voltage drop V across the crossing point, the differential

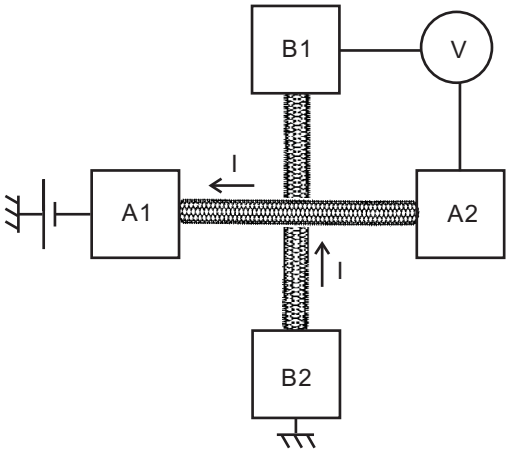

Figure 4.5: Schematic view of the tunneling measurements across the tube-tube junction. Current I is applied between electrode A1 and B2, voltage drop on the junction is measured between electrode A2 and B1.

tunneling conductance $G_X(V_X, T) = dI_X/dV_X$ (X signifies the crossed junction) can be measured. The geometry corresponds to electron tunneling from the middle of one tube to the middle of the other tube (bulk-bulk tunneling, see Eq 4.4.5). The double-logarithmic plots of $G_X(V_X, T)$ in the fig 4.6 are described by a power-law scaling with the slope $\alpha_{bulk-bulk} \approx 1.1$. Using $\alpha_{bulk-bulk} = (g^{-1} + g - 2)/4$ [72, 67], we find $g = 0.16$. This value is somewhat lower than the currently reported ones $g \approx 0.2$ for tunneling into a SWNT from a metal electrode[15, 73, 74]. This reflects a slightly stronger Coulomb interaction which is probably due to the different geometry of our devices; in particular, concerning the electrode location responsible for screening effects.

4.5.3 Zero-Bias Anomaly and its Suppression

We next measure the conductance of tube A while tube B is left floating. The Fig 4.7 shows the differential conductance dI_A/dV_A measured on tube A as a function of V_A for different temperatures T. We observe a clear **ZBA**, which becomes larger as T is decreased. Such a phenomenon has been observed many times in SWNTs [15, 73, 74]. It implies the presence of a barrier along the tube A or at the interface with electrodes. However we can not go further to determine the nature of the barrier at the moment.

We next impose a current I_B flowing through tube B. It is very interesting that the **ZBA** in tube A is progressively suppressed when I_B is increased (Similar behaviors

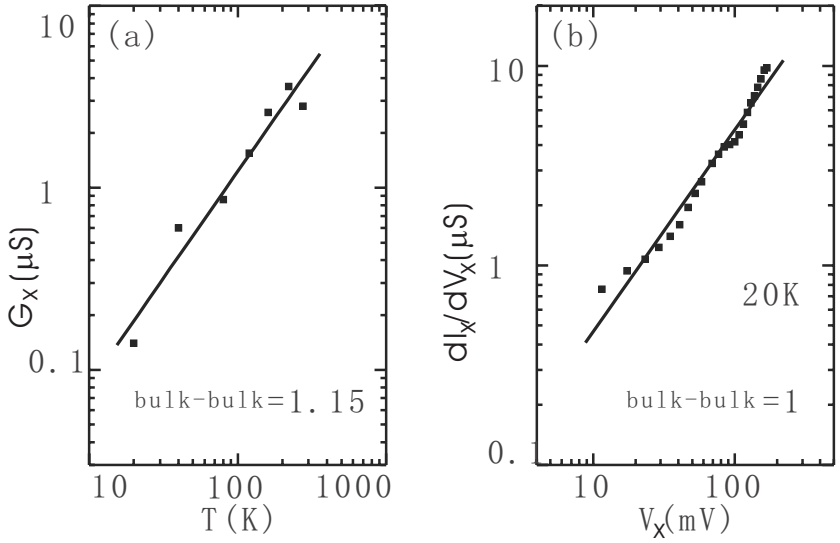

Figure 4.6: Tunnelling measurement on the tube-tube junction in a four-probe configuration. (a) Linear conductance $G_X(V_X = 0, T)$ (b) Differential conductance $dI_X/dV_X(V_X, T = 20K)$.

were also observed in other devices, see Fig 4.10). We note that the **ZBA** suppression depends only on the intensity of I_B and not on its sign. For these measurements, the sample is biased symmetrically about the junction so that no current flows from tube A into tube B through the crossing point. To achieve this, several three-points measurements are carried out in advance (see Fig 4.8), with the following procedure.

Firstly, a three-point measurement is carried out on tube A to determine the potential V_A^X at the crossing point. By adjusting the voltages applied on both electrodes A1 and A2, which are respectively $-aV_A$ and $(1-a)V_A$, we can find the parameter a as a function of V_A, which suppresses the potential at the junction so that no current flows through the junction into the tube B. Parameter a is nearly 0.5 as both contacts are almost transparent. The procedure is reproduced for tube B with parameter b. This time b is far away from 0.5, reflecting the large contact resistance at the B1 electrode. Finally, I_A is measured as a function of V_A for different V_B (and I_B) where voltages $V_{B1} = -bV_B + aV_A$ and $V_{B2} = (1-b)V_B + aV_A$ applied on electrodes B1 and B2 are continually adjusted so that V_A^X is always equal to V_B^X, which is aV_A. Since most of V_B drops at the bad contact B1, we give instead of V_B the current I_B in the

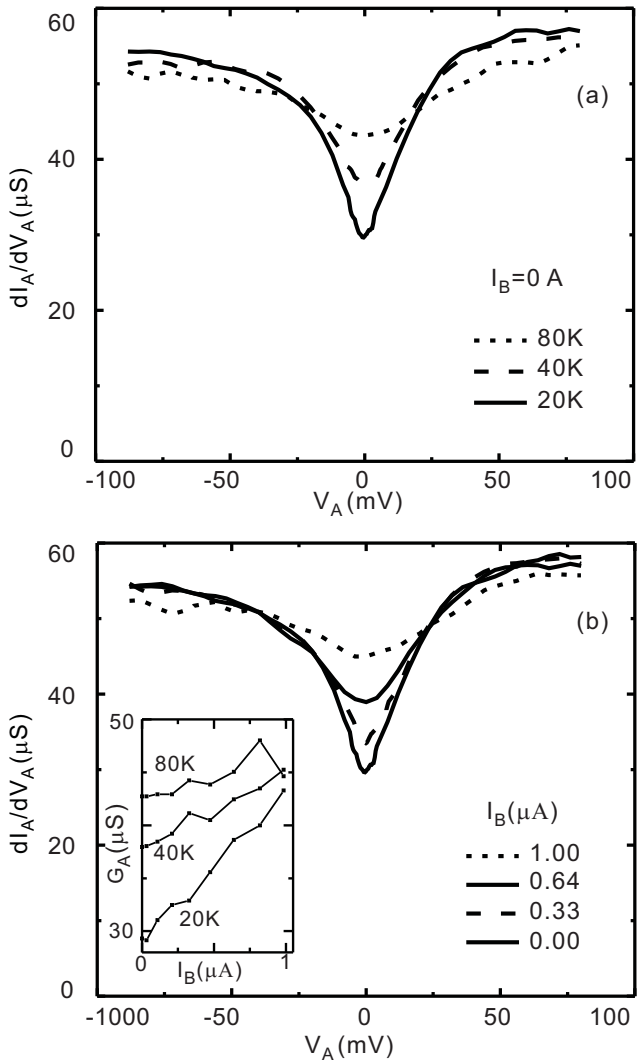

Figure 4.7: Differential conductance $dI_A/dV_A(V_A)$ measured on SWNT A (a) for different T and (b) for different I_B through SWNT B. Inset in (b) shows G_A for V_A=0 as a function of I_B. The maximum I_B corresponds to V_B=0. 8V. The points are separated by ΔV_B =0. 1V.

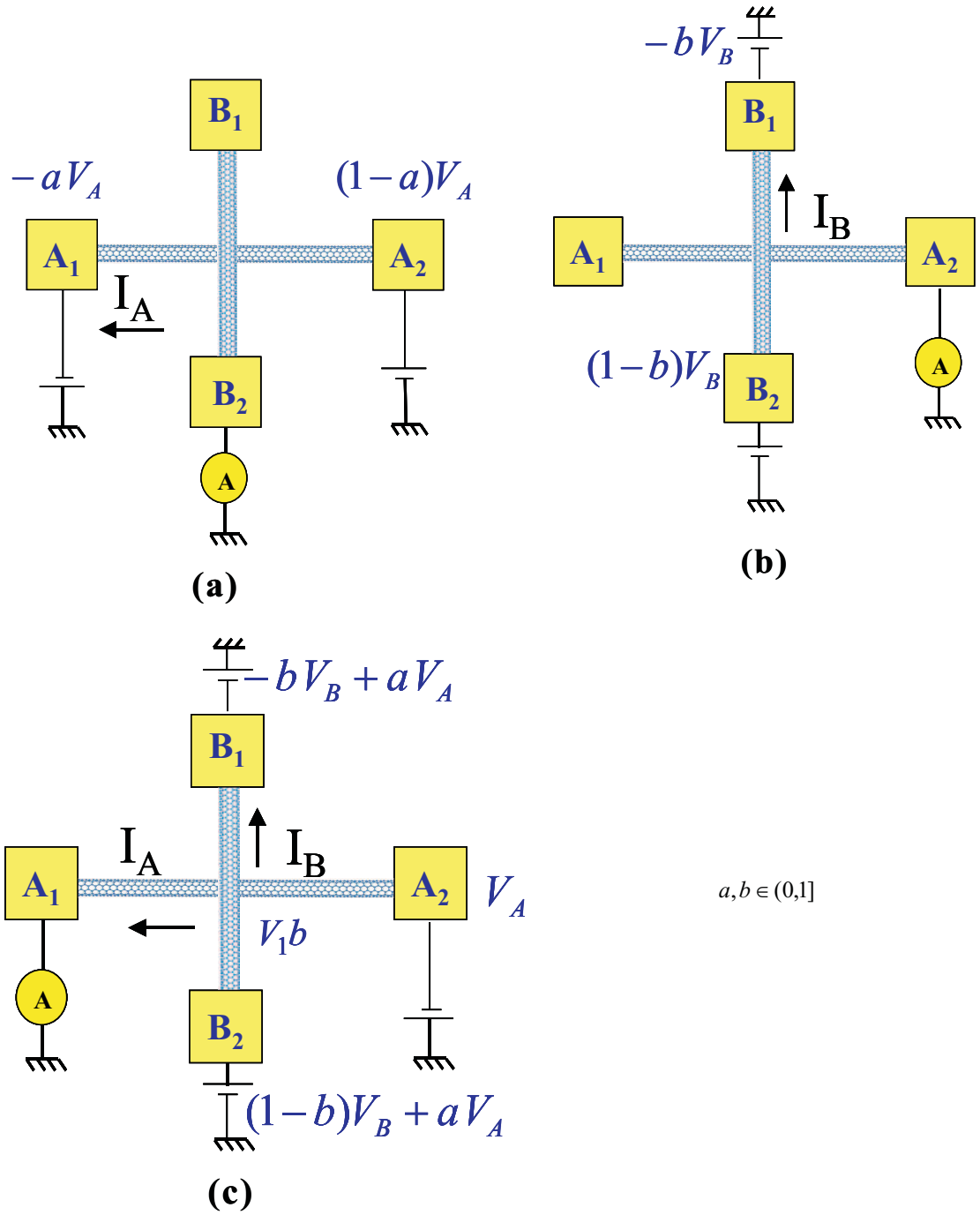

Figure 4.8: Three-terminal measurements to determine the voltage drop on the four electrodes. (a) a, as a function of the bias V_A, is the parameter with which the electrical potential at the crossing point in tube A is set to zero. (b) b, as a function of the bias V_B, is the parameter with which the electrical potential at the crossing point in tube B is set to zero. (c) The bias applied on B1 and B2 varies with V_A in this specific manner, therefore we can maintain a constant current I_B in tube B, while keeping that the potential at the crossing point in each tube is always equal to each other.

Fig 4.9 legend, which is measured while tube A is left floating.

4.5.4 Interpretation of Experimental Results

We review now some possible explanations for the I_B dependence of the **ZBA** in tube A. Let us first consider the effect of joule heating. Note that heating effect are generally disregarded in tunneling experiments into carbon nanotubes [15, 73, 74, 76, 77, 78]. However, the poor B1 contact releases significant heat when we increase the current in tube B. Part of the heat flows through tube A, which may then change the temperature sensitive conductance G_A. Unfortunately, the temperature rise ΔT is difficult to estimate, because little is known about the thermal conductances of individual SWNTs and tube-tube junctions. Out limited knowledge about the thermal conductance of SWNTs is that it increases with temperature when T is less than $100K$ [85, 86, 83]. Nevertheless, a qualitative statement can be made. The inset in Fig 4.7 describes the differential conductance G_A as a function of current I_B, measured at three different temperatures. Since we observe $G_A(20K, 0.6\mu A) \approx G_A(40K, 0A)$ and $G_A(40K, 0.6\mu A) \approx G_A(80K, 0A)$, this would mean that the same heat input (360nW) would give rise to different temperature increases, $20 \rightarrow 40K$ and $40 \rightarrow 80K$ respectively. This would imply that the thermal conductance decreases with T, which is at odd with our knowledge. Indeed, the temperature increase ΔT of tube A should be anti-proportional to the thermal conductance, for that the heat will dissipate faster into the environment. Hence our conclusion is that thermal effects alone cannot explain our observations. Another explanation might be related to the direct capacitive coupling between tubes, tube B playing the role of a local gate for tube A. The conductance can vary with back gate voltage V_g as seen in interference experiments [64, 16]. We indeed find that G_A fluctuates with V_g. One could argue that tube B acts as a local gate. However, the conductance fluctuation with V_g, which are lower than $2.1\mu S$, cannot account for the large modulation of $G_A(I_B)$. We conclude that another explanation is needed to account for our results.

We now compare the data to LL predictions for two crossed SWNTs with identical Luttinger Liquid parameter g [81, 82]. We will model our device by two Luttinger Liquid wires coupled in a pointlike manner. We suppose that both tubes are perpendicular, and that metallic electrodes onto the tubes are symmetric with respect to the crossing point. Such a structure will cause three different coupling mechanisms:

First, there will be a local density-density electrostatic interaction at the crossing point. Secondly, as both tubes are stacked on top of each other, a crossing-induced backscattering (**CIB**) process needs to be taken into consideration. The importance of **CIB** processe due to the tube deformation has been stressed in several previous experimental [84, 88] and theoretical studies [89, 90]. Another possible process is the single-particle hopping from one tube to the other one. However, as our experiments are carried out at zero tube-tube current, this single-electron tunneling can be neglected.

Let us first discuss the electrostatic interaction. The electrostatic interaction is taken as a local coupling acting only at the crossing point, which takes the form $H_{AB} = \lambda_0 \rho_A(0)\rho_B(0)$, where $\rho_\alpha(x)$ is the density operator corresponding to the charge density wave excitations in tube $\alpha = A, B$, λ_0 is the local density-density coupling strength. We firstly omit the mean density k_F/π which is supposedly neutralized by positive background charges. Then, as we have found the electron interaction strength g in our devices is around 0.16, this signifies very strong electron correlations. Therefore the dominant excitation is a high-order charge density wave whose wave length is equal to $\pi/4q_F$ [57], and $\rho_\alpha(x) \propto \cos\sqrt{16\pi g}\phi(x)$. (the wave vector q_F is related to band filling. An average excess density $\delta\rho$ compared to the unbiased half-filling case gives rise to a non-zero $q_F = \pi\delta\rho/4$. One can easily adjust the band filling by varying the back gate V_g.)

Now we turn to the back scattering induced by the geometrical deformations. The hamiltonian of **CIB** part can be described by $H_{CIB} = \lambda_1\rho_A(0) + \lambda_2\rho_B(0)$. With the standard renormalization group method [61], we can find the lowest-order flow equations

$$\begin{aligned} \frac{d\lambda_0}{dl} &= (1-8g)\lambda_0 + 2\lambda_1\lambda_2 \\ \frac{d\lambda_{1,2}}{dl} &= (1-4g)\lambda_{1,2} \end{aligned} \tag{4.5.1}$$

The initial coupling constants $\lambda_{0,1,2}(0)$ could be accessed from microscopic considerations but we only need here that they are nonzero. Integration the above equations yields

$$\begin{aligned} \lambda_{1,2}(l) &= \lambda_{1,2}(0)e^{(1-4g)l} \\ \lambda_0(l) &= [\lambda_0(0) - 2\lambda_1(0)\lambda_2(0)]e^{(1-8g)l} + 2\lambda_1(0)\lambda_2(0)e^{(2-8g)l} \end{aligned} \tag{4.5.2}$$

It is apparent that at low energy (large l), as the interaction parameter g in our device is about 0.16, the **RG** flow is completed dominated by $\lambda_0(l)$ due to second term in its expression. That is to say the density-density coupling is generated from the crossing induced backscattering coupling. It has an effective scaling dimension $K_{eff} = 4g - 1/2$. We need to note that for this argument, it is crucial that $g < 1/5$ (for having charge density wave as the dominating low energy excitations) and $\lambda_{1,2}(0) \neq 0$. The **CIB** processes drive the local electrostatic density-density coupling $\lambda_{0,eff}(l)$ to be the dominant interaction in this crossed geometry, whose fix point is now not $\lambda_0(0)$ but $2\lambda_1(0)\lambda_2(0)$. The strong coupling $\lambda_{0,eff}$ then generate a **ZBA** which disappears when current flows in the second tube. We will show below the exact solution of this problem.

As the $\lambda_{1,2}(l)$ terms have a scaling dimension less important than $\lambda_0(l)$ terms, we keep only the density-density coupling in the total Hamiltonian, and we arrive at the single-channel model in Ref. [81, 82]. In this model, we consider two spinless Luttinger liquids. Assuming that the tubes do not contain impurities, Hamiltonian of the uncoupled system is as we found in Section 4.2.

$$H_0 = \frac{1}{2}\int dx \sum_{m=1,2} [(\partial_x \tilde{\theta}_m)^2 + (\partial_x \tilde{\phi}_m)^2] \tag{4.5.3}$$

where we have put $\hbar = 1$ and the sound velocity $v \equiv v_F/g = 1$. The Hamiltonian H_{AB} corresponding to electrostatic interactions takes the form

$$H_{AB} = \lambda_{0,eff}\rho_A(0)\rho_B(0) \tag{4.5.4}$$

We can take the following variable transformation

$$\begin{aligned} \phi_\pm(x) &= [\tilde{\phi}_1(x) \pm \tilde{\phi}_2(x)]/\sqrt{2} \\ \theta_\pm(x) &= [\tilde{\theta}_1(x) \pm \tilde{\theta}_2(x)]/\sqrt{2} \end{aligned} \tag{4.5.5}$$

The total Hamiltonian $H_0 + H_{AB}$ decouples into the sum of $H_+ + H_-$ with

$$H_\pm = \frac{1}{2}\int dx[(\partial_x\phi_\pm)^2 + (\partial_x\theta_\pm)^2] \pm \lambda_{0,eff}\cos[\sqrt{8\pi K_{eff}}\phi_\pm(0)] \tag{4.5.6}$$

We get two completely decoupled system, each of which is formally equivalent to the problem of an elastic scatterer embedded into a spinless Luttinger Liquid [60]. Supposing I_+ and I_- are the effective current in each system, the current in each tube is then given by $I_m = (I_+ \pm I_-)/\sqrt{2}$.

Therefore the full nonlinear correlated transport problem of crossed Luttinger Liquids decouples into two effective single-impurity problems characterized by an effective interaction parameter $K_{eff} = 4g - 1/2$. This single impurity problem has been studied before in detail. For $K_{eff} = 1/4$, this can be made explicit by a simple analytical solution of the resulting transport problem [82]. This corresponds to $g = 0.1875$, which is close to our experimental value $g \approx 0.16$. While the exact solution can be obtained by any K_{eff} as well, away from $K_{eff} = 1/4$ [91], the solution is less transparent and shows only slight differences. For $K_{eff} = 1/4$, the current through tube A and B is

$$I_m = \frac{4e^2}{h}[V_\alpha - (U_+ \pm U_-)/\sqrt{2}] \tag{4.5.7}$$

with $U_\pm$ obeying the self-consistency relations

$$eU_\pm = 2kT_B Im\Psi\left[\frac{1}{2} + \frac{kT_B + i(eV_\pm - eU_\pm)}{2\pi kT}\right] \tag{4.5.8}$$

with the digamma function Ψ, $V_\pm = (V_A \pm V_B)/\sqrt{2}$, and an effective coupling strength $T_B \propto \lambda_0^{1/(1-2K_{eff})}$. The solutions employs radiative boundary conditions [91], which in turn assume ideal tube-electrode contacts. This assumption is, however, only restrictive here since $L_T \ll L$ (see above). For our devices, where three contacts are nearly ideal and only one has low transparency, the solutions receive only small corrections, (see Sec.4 in Ref[82]).

Fig 4.9 shows modified $dI_A/dV_A(V_A)$ curve of Fig 4.7. Indeed, Fig 4.7 shows that the high-bias differential conductance saturates at $(17.9k\Omega)^{-1}$ instead of $4e^2/h$, which is the high-bias conductance predicted by the above equations. We therefore argue that a resistance $R_c = 11.4k\Omega$ lies in series with the I_B dependant contribution of the intertube coupling in order to obtain this dI_A/dV_A saturation. R_c, presumably located at the tube-electrode interfaces, is taken constant. This approximation is quite good since the **ZBA** tends to disappear for large I_B, leaving only a weak $1/R_c$ conductance modulation. Moreover, the conductance is known to change only slightly with T or V in experiments on individual SWNTs that are well contacted with contact resistances of the order $10k\Omega$ [64, 16]. Fig 4.9 (c) and (d) show the predicted $dI_A/dV_A(V_A)$ curves calculated from Eq 4.5.7 and 4.5.8. The effective coupling T_B is set at $T_B = 11.6K$ to get agreement with the experimental value for G_A at $20K$; $I_B = 0$ and $V_A = 0$. After fixing T_B, no parameter is turned to calculate the condutance variation with

V_A, T and I_B. Despite the above-mentioned approximations, the agreement of theory and experiment is quite good. We note in passing that Eq 4.5.7 and 4.5.8 predict the emergence of minima in $dI_A/dV_A(V_A)$ for $I_B \geq 1\mu A$, which have not been observed though. One probable cause could be the inelastic scattering on optical phonons taking place at such large currents, which are not included in Eq 4.5.7 and 4.5.8.

In conclusion, we have observed on a crossed metallic SWNT junction a **ZBA** in one tube which is suppressed by a current flowing through the other. These measurements are in rather good agreement with an analysis based on Luttinger Liquid theory, which predicts a barrier along each tube generated by the electrostatic tube-tube interaction and controlled by current in other tube. The crossed tube junction thus provides an interesting system offering external control of the barrier transmission in a Luttinger Liquid that will be useful, e. g. , in noise measurements.

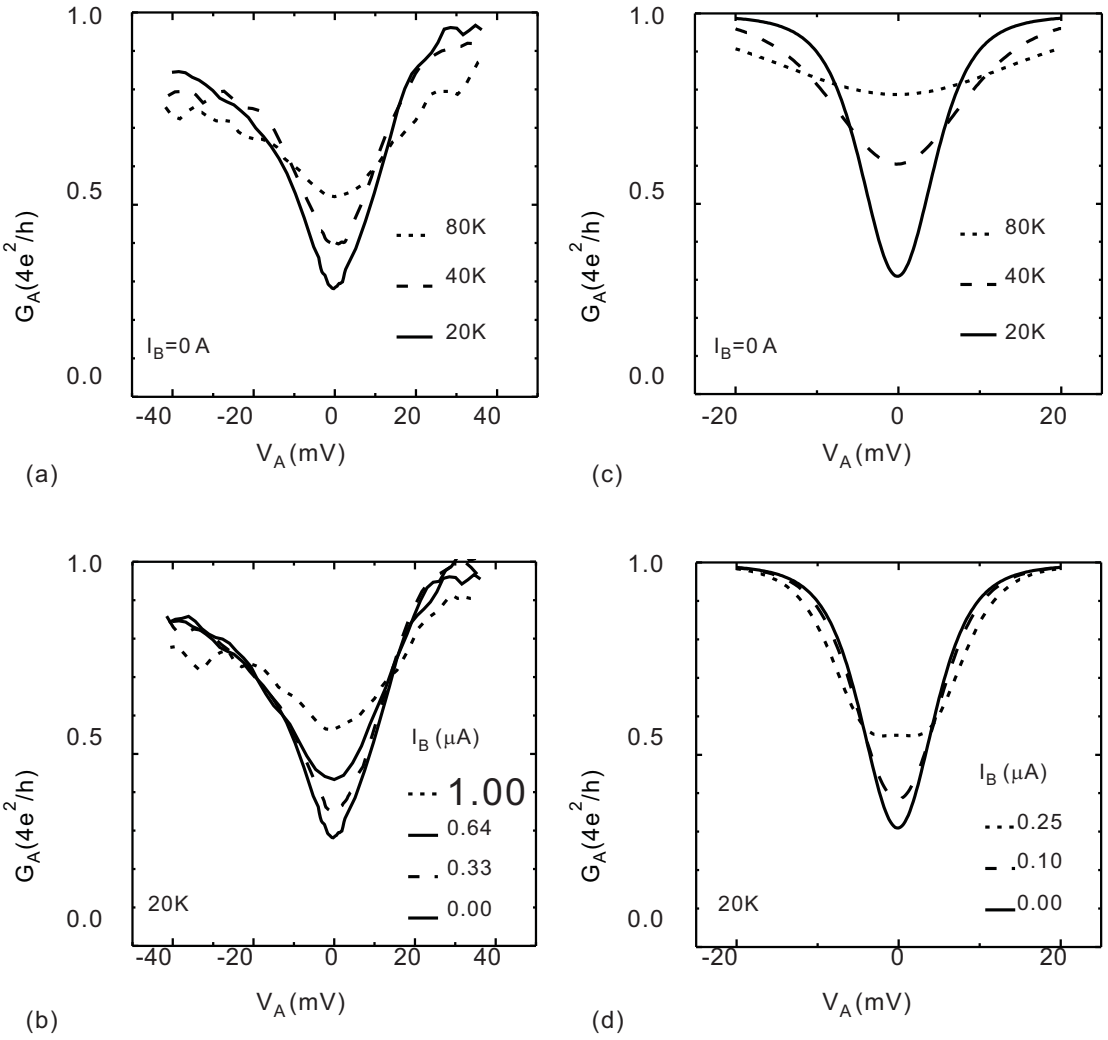

Figure 4.9: Differential conductance $dI_A/dV_A(V_A)$ of device 1 symmetrized and modified from Fig 4.7 for different T (a) and for different I_B (b). Theoretical predictions for two interacting SWNTs are shown in (c) and (d). The curves in (d) are obtained for constant biases V_B. The corresponding currents I_B, which are calculated with Eq 4.5.7 and 4.5.8 for $V_A = 0$, are given in the legend.

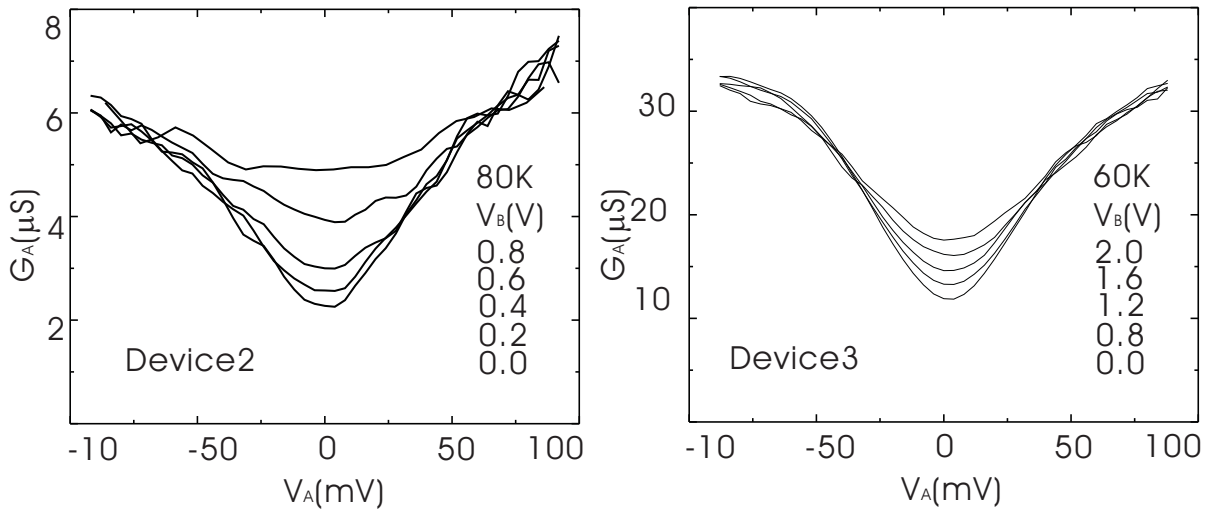

Figure 4.10: Similar curves(differential conductance of tube A versus voltage applied on tube B) obtained from other two devices.

Conclusion

As a conclusion, we have realized different multi-terminal electron transport measurements on a single-wall carbon nanotubes, which allow us to investigate the rich physics inside a carbon nanotube at different temperature scales.

Firstly, in order to investigate the intrinsic resistance of a single-wall carbon nanotubes, we developed a new type of four-terminal measurement method using multi-wall carbon nanotubes as voltage probes. Compared to two-terminal measurement, four-terminal measurements are not limited by the bad contacts between metal electrode and nanotube. Therefore in can in principle give the information about the intrinsic electrical properties of a carbon nanotube. Previous efforts to apply directly this method to a carbon nanotube was failed because metal electrodes can be invasive to a carbon nanotube. The reason has been clarified in previous chapiters. We have shown MWNTs are much less invasive to carbon nanotubes than metal electrodes. We thus realized a first true four-terminal measurement on a SWNT, which allows us to understand the intrinsic electrical properties of a SWNT at both high and low temperature. We found that SWNTs behave like classical resistors at room temperature by respecting the Ohm's Law. At liquid helium temperature, when varying the back-gate voltage, four-terminal measurements can read both positive and negative resistances. We attribute these negative resistances to quantum interference effect between different electron paths inside the SWNT. The experimental results can be understood within the frame of Laudauer-Büttiker formalism. Our findings support the validity of L-B formalism in a molecular system. In addition, with this new four-terminal measurement technique, we can investigate the effect of disorder along a carbon nanotube. We have experimentally studied the localization effect inside a SWNT. Though limited by time, this work was not included in this thesis, a detailed description can be found in Ref. [93].

Single-wall carbon nanotube is considered as an ideal model system to study one-dimensional interacting electron system, so-called Luttinger liquid state. Previous reports measuring tunneling current from metal elctrodes to a SWNT have shown a power-law behavior which is considered as a characteristic of LL. However there are still disputes around these measurements as a dynamical coulomb blockade model cannot be excluded. We have realized a different type of measurements on two crossed metallic SWNTs. We found that the conductance dip of one SWNT can be suppressed by increasing the current through the other tube. After precise analysis of the experimental results, we conclude that we have found new evidence of LL behavior inside SWNYS beyond the usual tunneling measurements.

Appendix

Appendix A

Bosonization Method

We present here a relatively complete description to the Bosonization method. One can start with fermions on a circle of Length L with periodic boundary condition. One may introduce the second quantized Fermi field of right- and left-moving components as the following:

$$\begin{aligned} \psi_\nu(x) &= \frac{1}{\sqrt{L}} \sum_{k=-\infty}^{\infty} c_{\nu,k}\, e^{i\nu kx} \\ k &= \frac{2\pi}{L} n_k \end{aligned} \tag{A.0.1}$$

with ν=$\boldsymbol{R}$ and $\boldsymbol{L}$ referring to right and left-moving components respectivly, where $n_k = 0, \pm 1, \pm 2....$ Fermion operator $c_{\nu,k}$ respects the following anticommutation relations.

$$\begin{aligned} \{c_{\nu,k}, c_{\nu',k'}\} &= 0 \\ \{c_{\nu,k}, c^\dagger_{\nu',k'}\} &= \delta_{\nu\nu'}\, \delta_{kk'} \end{aligned} \tag{A.0.2}$$

One can then define the Fermi sea of the system to be the state $|0\rangle$, which satisfies:

$$\begin{aligned} c_{\nu,k} \mid 0 > &= 0 \quad for\ k > 0 \\ c^\dagger_{\nu,k} \mid 0 > &= 0 \quad for\ k \leq 0 \end{aligned} \tag{A.0.3}$$

The normal ordered fermion number operator $\hat{N}_\nu$ can be defined in the following way:

$$\begin{aligned} \hat{N}_\nu &= \sum_{k=-\infty}^{\infty} : c^\dagger_{\nu,k} c_{\nu,k} : \\ &= \sum_{k>0} c^\dagger_{\nu,k} c_{\nu,k} - \sum_{k\leq 0} c_{\nu,k} c^\dagger_{\nu,k} \end{aligned} \tag{A.0.4}$$

One can easily find that$\hat{N}_\nu|0\rangle = 0$.

The next step is to define bosonic operators:

$$\begin{aligned} b^\dagger_{\nu,q} &= \frac{1}{\sqrt{n_q}} \sum_{k=-\infty}^{\infty} c^\dagger_{\nu,k+q} c_{\nu,k} \\ b_{\nu,q} &= \frac{1}{\sqrt{n_q}} \sum_{k=-\infty}^{\infty} c^\dagger_{\nu,k-q} c_{\nu,k} \\ q &= \frac{2\pi}{L} n_q, n_q = 1, 2, 3... \end{aligned} \tag{A.0.5}$$

One can easily check the following commutation relations:

$$\begin{aligned} [b_{\nu,q}, b_{\nu',q'}] &= 0 \\ [b_{\nu,q}, b^\dagger_{\nu',q'}] &= \delta_{\nu\nu'}\delta_{qq'} \\ [\hat{N}_\nu, b_{\nu',q}] &= [\hat{N}_\nu, b^\dagger_{\nu',q}] = 0 \end{aligned} \tag{A.0.6}$$

With these operators one can now define the chiral creation and annihilation operators:

$$\begin{aligned} \chi_\nu(x) &= \frac{i\nu}{2\sqrt{\pi}} \sum_{q>0} \frac{1}{\sqrt{n_q}} b_{\nu,q} e^{i\nu qx - \alpha q/2} \\ \chi^\dagger_\nu(x) &= -\frac{i\nu}{2\sqrt{\pi}} \sum_{q>0} \frac{1}{\sqrt{n_q}} b^\dagger_{\nu,q} e^{-i\nu qx - \alpha q/2} \end{aligned} \tag{A.0.7}$$

which, in the limit $L \to \infty$, satisfy the following commutation relations:

$$\begin{aligned} [\chi_\nu(x), \chi_\nu(x')] &= 0 \\ [\chi_\nu(x), \chi^\dagger_{\nu'}(x')] &= -\frac{1}{4\pi}\delta_{\nu\nu'} \ln[\frac{2\pi}{L}(\alpha - i\nu(x - x'))] \end{aligned} \tag{A.0.8}$$

One can then define the right- and left-moving bosonic fields $\phi_\nu(x)$ as:

$$\phi_\nu(x) = \chi_\nu(x) + \chi^\dagger_\nu(x) - \frac{\sqrt{\pi}x}{L}\hat{N}_\nu \tag{A.0.9}$$

which satisfies:

$$[\phi_\nu(x), \phi_{\nu'}(x)] = -\frac{i\nu}{4}\delta_{\nu\nu'} sign(x - x') \tag{A.0.10}$$

Finally one can define two phonon-like displacement fields dual to each other:

$$\begin{aligned} \phi(x) &= \phi_R(x) + \phi_L(x) \\ \theta(x) &= -\phi_R(x) + \phi_L(x) \end{aligned} \tag{A.0.11}$$

which satisfy:

$$\begin{aligned} [\phi(x), \phi(x')] &= [\theta(x), \theta(x')] = 0 \\ [\phi(x), \theta(x')] &= \frac{i}{2} sign(x - x') \end{aligned} \tag{A.0.12}$$

As we will see below, these phonon-like fields are to be used to describe the low-energy excitations in the Luttinger Liquid after adding the interaction. One may consider these fields as describing the displacement of a particle from its original lattice position, the system is just like a Wigner Crystal plus fluctuations.

Once the phonon-like displacement fields are defined, one can then define the chiral fermion density operators:

$$\begin{aligned}\rho_\nu(x) &=: \psi_\nu^\dagger(x)\psi_\nu(x) : \\ &= \frac{1}{L}\sum_{q>0}\sqrt{n_q}(b_{\nu,q}e^{iqx} + b_{\nu,q}^\dagger e^{-iqx}) \\ &+ \frac{1}{L}\sum_k : c_{\nu,k}^\dagger c_{v,k} := -\frac{1}{\sqrt{\pi}}\frac{\partial\psi_\nu}{\partial x}\end{aligned} \tag{A.0.13}$$

Therefore the total density and current operator are given by:

$$\begin{aligned}\rho x = \rho_R(x) + \rho_L(x) = -\frac{1}{\sqrt{\pi}}\partial_x\psi \\ j(x) = v_F(\rho_R(x) - \rho_L(x)) = \frac{v_F}{\sqrt{\pi}}\partial_x\theta\end{aligned} \tag{A.0.14}$$

One need to precise that the density operator $\rho(x)$ here measures only the fluctuation in the electron density. We have removed in the definition of $\rho(x)$ the mean electron density N_0/L.

If we introduce a linear dispersion relation $\epsilon_{\nu,k} = v_F k$, the Hamiltonian of non-interacting system can be written in fermionic and bosonic language respectively:

$$\begin{aligned}H_0 &= v_F\sum_{k=-\infty}^{\infty} : c_{R,k}^\dagger c_{R,k} + c_{L,k}^\dagger c_{L,k} : + \frac{\pi v_F}{L}(\hat{N}_R^2 + \hat{N}_L^2) \\ &= v_F\sum_{q>0} q(b_{R,q}^\dagger b_{R,q} + b_{L,q}^\dagger b_{L,q}) + \frac{\pi v_F}{L}(\hat{N}_R^2 + \hat{N}_L^2) \\ &= v_F\int_0^L dx[(\partial_x\phi_R)^2 + (\partial_x\phi_L)^2] \\ &= \frac{v_F}{2}\int_0^L dx[(\partial_x\phi)^2 + (\partial_x\theta)^2]\end{aligned} \tag{A.0.15}$$

Since the Hamiltonian of the non-interacting system has been found, one can now begin to add in the interaction of the following form:

$$V = \frac{1}{2}\int_0^L dx[2g_2\rho_R(x)\rho_L(x) + g_4(\rho_R(x)^2 + \rho_L^2(x))] \tag{A.0.16}$$

The interaction can be written in the fermionic language:

$$\begin{aligned}V = \frac{1}{2L}\sum_{k_1,k_2,k_3=-\infty}^{\infty} &[2g_2 c_{R,k_1+k_3}^\dagger c_{R,k_1} c_{L,k_2+k_3}^\dagger c_{L,k_2} \\ &+ g_4(c_{R,k_1+k_3}^\dagger c_{R,k_1} c_{R,k_2-k_3}^\dagger c_{R,k_2} \\ &+ c_{L,k_1+k_3}^\dagger c_{L,k_1} c_{L,k_2-k_3}^\dagger c_{L,k_2}]\end{aligned} \tag{A.0.17}$$

one can easily find the g_2 term corresponds to a two-particle interaction involving different chiralities; and the g_4 term corresponds to an interaction between two particles with the same chirality.

Once the interaction terms have been added, one can now write the total Hamiltonian $H = H_0 + V$. As we will see, it takes a very simple form in the bosonic language:

$$\begin{aligned} H =& \sum_{q>0} q[v_F(b^\dagger_{R,q}b_{R,q} + b^\dagger_{L,q}b_{L,q}) + \frac{g_2}{2\pi}(b^\dagger_{R,q}b^\dagger_{L,q} + b_{R,q}b_{L,q}) \\ &+ \frac{g_4}{2\pi}(b^\dagger R, qb_{R,q} + b^\dagger_{L,q}b_{L,q})] + \frac{\pi v_F}{L}(\hat{N}^2_R + \hat{N}^2_L) \\ &+ \frac{g_2}{L}\hat{N}_R\hat{N}_L + \frac{g_4}{2L}(\hat{N}^2_R + \hat{N}^2_L) \end{aligned} \tag{A.0.18}$$

One can easily see that the effect of g_4 term is to renormalize the Fermi velocity to $v_F + \frac{g_4}{2\pi}$. And the g_2 term can be diagonalized by a Bogoliubov transformation. One can define the following two parameters:

$$\begin{aligned} v =& [(v_F + \frac{g_4}{2\pi} - \frac{g_2}{2\pi})(v_F + \frac{g_4}{2\pi} + \frac{g_2}{2\pi})]^{1/2} \\ g =& [(v_F + \frac{g_4}{2\pi} - \frac{g_2}{2\pi})/(v_F + \frac{g_4}{2\pi} + \frac{g_2}{2\pi})]^{1/2} \end{aligned} \tag{A.0.19}$$

In the conventional case case, one can take $g_2 = g_4 > 0$ (repulsive interaction), v is therefore the plasmon velocity which is larger than Fermi velocity because the repulsive interaction reduces the compressibility of the electron gas. And g is the parameter that we mentioned above, which describes the interaction strength between electrons, $g < 1$ for repulsive interaction.

The Bogoliubov transformation now take the forms:

$$\begin{aligned} \tilde{b}_{R,q} &= \frac{b_{R,q} + \gamma b^\dagger_{L,q}}{\sqrt{1-\gamma^2}} \\ \tilde{b}_{L,q} &= \frac{b_{L,q} + \gamma b^\dagger_{R,q}}{\sqrt{1-\gamma^2}} \\ \gamma &= \frac{1-g}{1+g} \end{aligned} \tag{A.0.20}$$

One can now rewrite the total Hamiltonian in the quadratic expression:

$$\begin{aligned} H =& \sum_{q>0} vq[\tilde{b}^\dagger_{R,q}\tilde{b}_{R,q} + \tilde{b}^\dagger_{L,q}\tilde{b}_{L,q}] \\ &+ \frac{\pi v}{2L}[\frac{1}{g}(\hat{N}_R + \hat{N}_L)^2 + g(\hat{N}_R - \hat{N}_L)^2] \\ &= \frac{v}{2}\int_0^L dx[g(\partial_x\theta)^2 + \frac{1}{g}(\partial_x\phi)^2] \\ &= \frac{v}{2}\int_0^L dx[(\partial_x\tilde{\theta})^2 + (\partial_x\tilde{\phi})^2] \end{aligned} \tag{A.0.21}$$

The old and new bosonic fields are related as:

$$\begin{aligned} \phi_R &= \frac{(1+g)\tilde{\phi}_R - (1-g)\tilde{\phi}_L}{2\sqrt{g}} \\ \phi_L &= \frac{(1+g)\tilde{\phi}_L - (1-g)\tilde{\phi}_R}{2\sqrt{g}} \\ \phi &= \sqrt{g}\tilde{\phi} \; and \; \theta = \frac{1}{\sqrt{g}}\tilde{\theta} \end{aligned} \tag{A.0.22}$$

Appendix B

Cotunneling and one-dimensional localization

Bibliography

[1] S. Datta, *Electronic Transport in Mesoscopic Systems* (Cambridge University Press, Cambridge, 1997).

[2] S. Tomonaga, Prog. Theor. Phys, **5**, 544 (1950)

[3] J. M. Luttinger, J. Math. Phys,**4**, 1154 (1963)

[4] J. A. E. Gibson , Nature. **359**, 369 (1992).

[5] A. Oberlin, *et al.*, Journal of Crystal Growth, **32**, 335, (1976).

[6] S. Iijima , *et al.*, Nature. **354**, 56 (1991).

[7] S. Iijima , *et al.*, Nature. **363**, 603 (1993).

[8] D. S. Bethune , *et al.*, Nature. **363**, 605 (1993).

[9] T. Guo , *et al.*, Chem. Phys. Lett, **243**, 49 (1995).

[10] A. Thess *et al.*, Science **273**, 483 (1996).

[11] M. Bockrath, *et al.*, Science **275**, 1922 (1997)

[12] S. J. Tans,*et al.*, Nature, **386**, 474 (1997).

[13] J. W. G. Wilder, *et al.*, Nature, **391**, 59, (1998).

[14] T. W. Odom, *et al.* Nature **391**, 62 (1998).

[15] M. Bockrath, *et al.*, Nature **397**, 598 (1999).

[16] W. Liang, *et al.*, Nature **411**, 665 (2001).

[17] B. Gao, *et al.*, Phys. Rev. Lett. **92**, 216804 (2004).

[18] B. Gao, *et al.*, Phys. Rev. Lett. **95**, 196802 (2005).

[19] Yuanbo Zhang, *et al.*, Nature. **438**, 201 (2005).

[20] K. S. Novoselov, *et al.*, Nature. **438**, 197 (2005).

[21] G. S. Painter, *et al.*,s, Phys. Rev. B, **1**, 4747 (1970).

[22] R. Saito, G. Dresselhaus, M. S. Dresselhaus, *Physical Properties of Carbon Nanotubes*, Imperial College Press (1998).

[23] R. Saito, *et al.*, Phys. Rev. B, **46**, 1804 (1992).

[24] J. W. Mintmire, *et al.*, Phys. Rev. Lett, **68**, 631 (1992).

[25] C. Joachim, *et al.*, Nature(London), **408**, 541 (2000).

[26] A. Bachtold, *et al.*, Phys. Rev. Lett. **84**, 6082 (2000).

[27] P.J. de Pablo, *et al.*, Phys. Rev. Lett. **88**, 036804 (2002).

[28] M. Freitag, *et al.*, Phys. Rev. Lett. **89**, 216801 (2002).

[29] M.S. Gudiksen,*et al.*, Nature **415**, 617 (2002).

[30] Y. Yaish, *et al.*, Phys. Rev. Lett. **92**, 046401 (2004).

[31] A. Bezryadin, *et al.*, Phys. Rev. Lett. **80**, 4036 (1998).

[32] J. Nygard, *et al.*, Appl. Rhys. A. **69**, 297(1999).

[33] M. Büttiker, Phys. Rev. Lett. **57**, 1761 (1986).

[34] M. Büttiker, IBM J. Res. Develop. **32**, 317 (1988).

[35] M. Büttiker, Phys. Rev. B **32**, R1846 (1985).

[36] M.S. Fuhrer, *et al.*, Science **288**, 494 (2000).

[37] H. R. Shea, *et al.*, Phys. Rev. Lett. **84**,4441(2000).

[38] H. T. Man, *et al.*,, Phys. Rev. Lett. **95**, 026801(2005).

[39] H. Van Houten, *et al.*, in : *Singel Charge Tunneling* , ed by. H. Grabert and M. H. Devoret, Plenum Press, New York(1992)

[40] D. V. Averin, *et al.*, in : *Mesoscopic Phenomena in Solids* , ed by. P. A. Lee and R. A. Webb, Elsevier Amsterdam(1991)

[41] D.H. Cobden, *et al.*, Phys. Rev. Lett. **89**, 046803 (2002)

[42] Y. Oreg, *et al.*, Phys. Rev. Lett. **85**, 365(2000)

[43] S. Sapmaz, *et al.*, Phys. Rev. B. **71**, 153402(2005)

[44] J.H. Hafner, *et al.*, Phys. Chem. B **105**, 743 (2001).

[45] H. Stahl, *et al.*, Phys. Rev. Lett. **85**, 5186 (2000).

[46] B. Bourlon, *et al.*, Phys. Rev. Lett. **93**, 176806 (2004).

[47] V.A. Gopar, *et al.*, Phys. Rev. B **50**, 2502 (1994).

[48] M. Büttiker, Phys. Rev. B **40**, R3409 (1989).

[49] Y. Takagaki, *et al.*, Solid Stat Commun. **68**, 1051 (1988).

[50] R. de Picciotto, *et al.*, Nature **411**, 51 (2001).

[51] A.B. Fowler, *et al.*, Phys. Rev. Lett. **48**, 196 (1982).

[52] L.D. Landau and E.M. Lifshitz, Statistical Physics (Part 2) - Course of Theoretical Physics-Vol. 9, Butterworth-Heinemann, (1998)

[53] Field theories in condensed matter physics,edited by S. Rao (Institute of Physics Publishing, 2002).

[54] H. J. Schulz: in Mesoscopic Quantum Physics, Les Houches, Session LXI, 1994, ed. by E. Akkermans, G. Montambaux, J.-L. Pichard, J. Zinn-Justin (Elsevier Amsterdam 1995)

[55] G. Morandi, P. Sodano, A. Tagliacozzo, V. Tognetti, Field theories for low-dimensional condensed matter systems ,(Springer Series in Solid-State Sciences 131, 2000).

[56] C.L. Kane, *et al.*, Phys. Rev. Lett. **68**, 1220 (1992).

[57] R.Egger *et al.*, Eur.Phys.J.B **3**, 281 (1998)

[58] F. Dolcini, *et al.*, Phys. Rev. Lett. **91**, 266402 (2003).

[59] C.L. Kane, Physica. B. **189**, 250 (1993).

[60] C.L. Kane, *et al.*, Phys. Rev. B. **46**, 15233 (1992).

[61] A.O. Gogolin, A.A. Nersesyan, A.M. Tsvelik, *Bosonization and strongly correlated systems* (Cambridge University Press, 1998).

[62] Matthew P. A. Fisher and Leonid I. Glazman, **Mesoscopic Electron Transport**, eds by L. L. Sohn et al, Kluwer Academic Publishers (1997).

[63] I. Safi, Phys. Rev. B **55**, R7331 (1997).

[64] J. Kong, *et al.*, Phys. Rev. Lett. **87**, 106801 (2001).

[65] E. B. Sonin, cond-mat/0103017,(2001)

[66] K. A. Matveev *et al.*, Phys. Rev. Lett. **70**, 990 (1993)

[67] C. Kane, *et al.*, Phys. Rev. Lett. **79**, 5086 (1997).

[68] M. H. Devoret, *et al.*, Phy. Rev. Letter. **64**, 1824 (1990).

[69] G. Schön and A. D. Zaikin, Phys. Rep. **198**, 237 (1990).

[70] A. N. Cleland, *et al.*, Phys. Rev. B. **45**, 2950 (1992).

[71] I. Safi *et al.*, Phys. Rev. Lett. **93**, 126602 (2004).

[72] R. Egger *et al.*, Phys. Rev. Lett. **79**, 5082 (1997).

[73] Z. Yao, *et al.*, Nature **402**, 273 (1999).

[74] H.W.C. Postma, *et al.*, Phys. Rev. B **62**, 10653 (2000).

[75] H.W.Ch. Postma, T*et al.*, Science **293**, 76 (2001).

[76] A. Bachtold, *et al.*, Phys. Rev. Lett. **87**, 166801 (2001).

[77] R. Tarkiainen, *et al.*, Phys. Rev. B **64**, 195412 (2001).

[78] W. Yi, *et al.*, Phys. Rev. Lett. **91**, 076801 (2003).

[79] R. Egger *et al.*, Phys. Rev. Lett. **87**, 066401 (2001).

[80] E.G. Mishchenko, *et al.*, Phys. Rev. Lett. **87**, 246801 (2001)

[81] A. Komnik *et al.*, Phys. Rev. Lett. **80**, 2881 (1998).

[82] A. Komnik *et al.*, Eur. Phys. J. B **19**, 271 (2001).

[83] J. Kim, *et al.*, J. Phys. Soc. Jpn. **70**, 1464 (2001).

[84] J.W. Janssen, *et al.*, Phys. Rev. B **65**, 115423 (2002).

[85] S. Berber, *et al.*, Phys. Rev. Lett. **84**, 4613 (2000).

[86] Q. Zheng, *et al.*, Eur. Phys. J. B **25**, 233 (2003).

[87] P. Kim, *et al.*, P.L. McEuen, Phys. Rev. Lett. **87**, 215502 (2001).

[88] T. Hertel, *et al.*, Phys. Rev. B **58**, 13870 (1998).

[89] A. Rochefort, *et al.*, Phys. Rev. B **60**, 13824 (1999).

[90] M.B. Nardelli *et al.*, Phys. Rev. B **60**, 16338 (1999).

[91] R. Egger, *et al.*, Phys. Rev. Lett. **84**, 3682 (2000).

[92] Z. Yao, *et al.*, Phys. Rev. Lett. **84**, 2941 (2000).

[93] B. Gao, *et al.*, Cotunneling and one-dimensional localization in individual disordered single-wall carbon nanotubes: Temperature dependence of the intrinsic resistance, to be published on Phys. Rev. B, see appendix B.